KU LEUVEN

FACULTEIT WETENSCHAPPEN

Tuning the percolation of attractive Red Blood Cells

Kwinten TORFS

Promotor: Prof. M.P. Lettinga
KU Leuven, FZ Jülich

Begeleider: *M. Babaki*
KU Leuven, FZ Jülich

Proefschrift ingediend tot het
behalen van de graad van
Master of Science in Fysica

Academiejaar 2020-2021

Preface

When I first started working on red blood cells in July 2020, I could have never expected to get to where I am today. It surprises me how fast everything has passed by from knowing virtually nothing about red blood cells to writing this thesis. This whole year proved to be an adventure in which I have gained important insights, both academic and personal. It shaped me as better scientist, researcher, friend and person. I am thus extremely grateful for everyone that helped me during this work, everyone I met along the way, and all those that supported me now and before.

First and foremost, I would like to thank my supervisor, Pavlik Lettinga, and my mentor, Mehrnaz Babaki, who have guided and taught me so much valuable skills the past year. Both of you have been instrumental in the creation and finalisation of this thesis. Pavlik, I would like to express my great appreciation for the frequent discussions (both online and in real life), patience when I didn't understand things and your ideas and solutions for problems that we encountered. Mehrnaz, I would like to particularly thank you for teaching me all the experimental details of working with red blood cells during my time in the Forschungszentrum Jülich and in Leuven.

Furthermore, I want to show my gratitude for everyone that has helped me in the laboratories at SMART in Leuven. Thank you Erin, Andi and especially Jens and Sebastian. Sebastian, I am very happy that you let me use the desktop to run lengthy calculations and want to thank you for your contribution to the idea of finding percolation networks. Jens, I genuinely appreciate that you were always present to help with issues in the wet-lab, in the confocal lab and with the rheometer.

The next line of thank is for everyone at IBI-4, in Jülich, that I met and helped me throughout the summer internship there. I would like to thank Thorsten Auth for arranging the IHRS Biosoft guest programme. Further I would like to thank Oli and Amir for your discussions and ideas during our weekly 'Blood meetings' with Pavlik and Mehrnaz.

I would also like to express my gratitude to both readers of this thesis for taking the time to review this work.

Although I have seen you less this year than I had hoped, I want to thank my friends/colleagues/fellow students of *Knabenphysik*: Bram, Michelle and Thibo. Apart from improving these past 5 years of study, thanks for providing me with good ideas, useful tips and tricks, the constant reminders and, of course, the frequent singing of *Take away your billion dollars*.

Next, I would have never survived this year without the distractions provided by my RMS-roommates that brought my much joy. Ladies, thanks for all the wonderful evenings after the long workdays, the frequent baking of cookies, the carol-singing, the *De Mol*-viewing, the excessive trips to *'t Galetje* and your overall contribution to my general well-being. A special thanks goes out to Ellen, Elien, Mira and Lotte. Lynn and Megan, thank you for lighting up each day with your optimism, laughter and characters. Adelheid, besides your enthusiasm, kindness and general Chiro-minded spirit, I thoroughly enjoyed our small walks to and from the library which easily got me through the first weeks of writing this thesis. Finally I wish to express my gratitude to my sister Emma. Even though I don't acknowledge it as often as I should, you have always been there for me. Thank you for helping me directly in this work by accompanying me to the library these past weeks and, most importantly, introducing me to Mendeley. Besides I also want to thank you for your indirect help by often cooking or doing the dishes, listen and join me for lunches, walks, trips,... I sincerely hope, you will get the same opportunities as me later on.

Dan richt ik me nog tot m'n familie. Eerst en vooral bedank ik m'n grootouders (Hildegard en Ivo) en meter en nonkel (José en Herman). De leuke gesprekken die we hebben wanneer ik in het weekend eens binnensprong, ervaarde ik steeds als een moment van rust doorheen de drukke weken. Oma, bedankt voor het (al jaren) wekelijks heerlijk koken op vrijdag en je steun gedurende m'n ganse tijd in Leuven.

Tot slot wil ik mijn ouders, Jan en Elke, nog bedanken. Bedankt om mij steeds in al mijn academische keuzes te steunen, mij de kans te geven om deze studies op te nemen, altijd in mij te geloven en er steeds voor mij te zijn. Zonder jullie zou ik nooit uitgekomen zijn waar ik nu ben.

Kwinten Torfs - 9 June 2021

Abstract

English

In this thesis, we study the phase behaviour of red blood cells (RBCs) mixed with two attraction inducing macromolecules: polysaccharide dextran $70kDa$ and rod-like *fd*-virus. We observe transitions between various phases that emerge at varying concentrations of cells and macromolecules. We focus, however on the percolation of such mixtures into a colloidal gel.

Red blood cells play a key role in the shear thinning behaviour of blood through the formation of linearly stacked aggregates, called rouleaux. Rouleaux are formed when biconcave RBCs stick together under an attractive interaction due to the presence of certain macromolecular plasma proteins, like fibrinogen in human blood plasma. The most common macromolecule, used in RBC aggregation experiments, is neutral dextran, that induces short range attraction through a cross mechanism of bridging and depletion. Fd on the other hand, is an ideal long-range depletant. Although RBC aggregation and rouleaux formation are extensively studied, detailed research into percolation of RBC networks is lacking. In comparison to colloidal spheres, shape anisotropy in RBCs is crucial for rouleaux formation and branching of said rouleaux to form three-dimensional network structures.

Using laser scanning confocal microscopy, we investigate the aggregate phases of RBC-macromolecule systems and compare differences for short ranged dextran and long-ranged *fd*. Furthermore, we developed a direct method to identify percolated networks in confocal images, which allowed the construction of the percolation transition line for RBCs.

The results in this thesis show that percolated networks of RBCs can form over a broad range of RBC volume fractions for both dextran and *fd*. Besides percolation, we classify gas, gas-rouleaux co-existence and branched rouleaux phases in the RBC-dextran phase diagram. For RBC-*fd* mixtures, gas and gas-cluster co-existence is described.

We conclude that RBCs form percolated structures which are strikingly different from those composed of colloidal spheres. Furthermore, the coherent description of aggregate types at different concentrations of macromolecules and RBCs is beneficial to the understanding of the rheological behaviour of RBC mixtures and blood.

Nederlands

In deze thesis onderzoeken we colloïdale gelen van rode bloedcellen (RBC) voor twee attractie inducerende macromolecules: het polysacharide dextran $70kDa$ en staafvormig *fd*-virus.

Voorts tonen fasediagrammen van RBC-macromolecuulmengsels de verschillende fases en transities bij wisselende concentraties cellen en macromoleculen.

Rode bloedcellen spelen een cruciale rol in het *shear thinning* gedrag van bloed door de vorming van lineair geordende aggregaten, rouleaux genaamd. Rouleaux vormen wanneer rode bloedcellen samenklitten o.i.v. een attractieve interactie door de aanwezigheid van macromoleculaire plasmaproteïnen, zoals fibrinogeen in bloedplasma. Het vaakst voorkomende macromolecuul, gebruikt in RBC aggregatie experimenten, is neutraal dextran, dat interactie op korte afstand opwekt. Attractie door dextran bestaat uit een mix van depletie en overbrugging van macromolecules tussen cellen. Fd, echter, vertoont ideale depletie op lange afstand. Hoewel RBC aggregatie en rouleaux formatie uitgebreid bestudeerd zijn, ontbreekt gedetailleerd onderzoek naar de percolatie van RBC netwerken. In tegenstelling tot colloïdale sferen, blijkt de vorm-anisotropie van rode bloedcellen cruciaal voor rouleauformatie en vertakking van die rouleaux tot driedimensionale netwerkstructuren.

Door het gebruik van een laser-scanning confocaal microscoop, onderzochten we de aggregatie fases van RBC-macromolecuul systemen en vergelijken we de verschillen tussen de invloed van attractie op korte of lange afstand. Verder ontwikkelden we een directe methode om percolatie van netwerken op te sporen in confocaalbeelden, waardoor we een percolatie-transitie lijn konden opstellen voor rode bloedcellen.

De resultaten van dit werk tonen dat percolatienetwerken opduiken onder invloed van dextran en *fd* concentraties bij een waaier aan RBC volume fracties. Naast percolatie, categoriseren we ook de gas, gas-rouleaux co-existentie en vertakte rouleaux fases in het RBC-dextran fasediagram. Voor RBC-*fd* mengsels beschrijven we nog een gas en gas-cluster co-existentie fase.

Uiteindelijk besluiten we dat de percolatie structuren die bestaan uit rode bloedcellen duidelijk verschillend zijn aan die voor colloïdale sferen. Daarenboven kan de samenhangende beschrijving van soorten aggregaten bij verschillende concentraties RBC en macromoleculen bijdragen aan het verstaan van rheologisch gedrag van RBC mengsels en bloed.

Popular summary

Red blood cells (RBC), the most abundant cells in human blood, stick together due to the presence of certain plasma proteins. The unusual shape of the cells enables them to form structures that resemble stacks of coins, called rouleaux. In contrast with blood clotting, red blood cell aggregation is a reversible process where the rouleaux can again break up into single cells when a force is applied. In this work, we study systems where large numbers of RBCs are strongly attracted to one another. In such systems, we observe that after initial aggregation of rouleaux, larger networks of cells are formed. Besides cells stacking face-to-face, they also start attaching to the sides of the rouleaux, creating anchoring points for new rouleaux. This results in branches of rouleaux growing outwards on the initial rouleau, that can extend out and form other branches. Eventually the whole system consists of an intricate network of these branched rouleaux. At the point where a network of cells spans the entire sample, that network is said to be percolated. We were the first to our knowledge that created such percolated networks of RBCs while controlling the different components in the sample.

We investigate the structure in samples of red blood cells by imaging the systems with fluorescence confocal microscopy. The cells are labelled with a certain dye that is distributed in the cell's membrane. The dye emits light after it is illuminated with a laser, that is then measured by the confocal microscope. This type of microscope allows for samples to be scanned in three dimensions. This enables us to generate 3D images of the RBC networks. From these images, we can examine the different structures of the RBC specimens and determine where percolation occurs.

Percolated networks and rouleaux are highly important to the flow of blood. In the body, the heart vigorously pumps the blood, breaking down rouleaux into single cells that easily flow. This break-up is necessary since rouleaux are too large to fit through the capillaries, whereas single red blood cells can. Percolated networks, behave much more like solids and their structure is less easily destroyed. Besides increased RBC aggregation being an indication of certain diseases, it can also be theorised that percolation networks form if the force to break the up is too low. This could be the case for people with very low heart rate (like sportsmen) or e.g. for patients with reduced blood flow after lengthy hospitalisations.

In conclusion, this works touches the existence of percolated red blood cell networks. Although an interesting phenomenon, plenty of research needs to be performed to fully characterise the percolation transition.

Vulgariserende samenvatting

Rode bloedcellen (RBC), de meest voorkomende cellen in menselijk bloed, plakken aan elkaar door de aanwezigheid van bepaalde plasmaproteïnen. De ongebruikelijke vorm van de cellen laat hen toe structuren te vormen die lijken op geldrollen. Deze structuren zijn gekend als rouleaux. In tegenstelling tot bloedstolling, is RBC-aggregatie een reversibel proces waar de rouleaux kunnen opsplitsen tot enkele RBC wanneer er een kracht op inwerkt. In dit werk bestuderen we systemen waar een groot aantal rode bloedcellen sterk tot elkaar worden aangetrokken. In deze stelsels observeren we dat, na rouleaux-aggregatie, er grotere netwerken van cellen kunnen vormen. Naast de lijnvormige opstapeling, gaan de rode bloedcellen ook aan de zijkanten van rouleaux hechten. Deze cellen vormen dan ankerpunten voor vertakkingen van nieuwe rouleaux op het initieel gevormde aggregaat. Uiteindelijk bestaat het ganse systeem uit een ingewikkeld netwerk van vertakkende RBC-rouleaux. Op het punt dat een celnetwerk de volledige ruimte bekleed noemen we dat netwerk gepercoleerd. Zover we weten, zijn we de eersten die zo'n gepercoleerde netwerken van rode bloedcellen creëerden terwijl we de verschillende componenten van het systeem konden controleren.

We onderzoeken de structuren in mengsels van rode bloedcellen door beelden te maken met confocale fluorescentiemicroscopie. De cellen worden gelabeld met een fluorescente kleurstof, verdeeld over het celmembraan. Wanneer de stof wordt belicht met een laser, zal het zelf licht uitzenden dat dan wordt gemeten in de confocaal microscoop. Dit soort microscoop laat toe om 3D beelden te maken van stalen. Van deze beelden kunnen we verschillende RBC-structuren onderzoeken en bepalen waar percolatie optreedt.

Gepercoleerde netwerken en rouleaux zijn beiden zeer belangrijk voor de bloedstroom. In het lichaam pompt het hart het bloed krachtig rond. Deze kracht zorgt ervoor dat rouleaux opbreken in individuele cellen die makkelijker stromen. Als het hart niet in staat is de structuren op te breken, kan het bloed niet door de kleinste capillairen. Deze bloedvaten zijn zo klein dat rode bloedcellen er juist door geraken, maar rouleaux niet. Gepercoleerde netwerken gedragen zich nog meer vast en hun structuur is dan ook moeilijker te vernietigen. Naast dat rode bloedcelaggregatie een indicator voor bepaalde ziekten is, kan het ook worden gesteld dat gepercoleerde netwerken kunnen vormen wanneer de opbreekkracht te klein is. Dit kan optreden bij mensen met een lage hartslag (bijvoorbeeld sporters) of patiënten met een verlaagde bloeddoorstroming bij langdurige hospitalisatie.

Tot slot besluiten we dat gepercoleerde rode bloedcelnetwerken een interessant fenomeen zijn waar nog veel bijkomend onderzoek moet worden naar verricht om een beter zicht te krijgen op het karakter van deze systemen.

Glossary

B Bending modulus.

C_γ Strain constant.

C_σ Stress constant [m^{-3}].

D Diameter of rods [nm].

E Energy (in eV or J).

F_a Total aggregation force [N].

F_b Bridging force [N].

F_d Depletion force [N].

F_e Electrostatic force [N].

F_m Mechanical bending force of membrane [N].

F_s Shear force [N].

F Helmholtz free energy.

G" Shear loss modulus [Pa].

G' Shear storage modulus [Pa].

G Gravitational acceleration $1G = 9.81\,\mathrm{m/s^2}$.

G Shear modulus [Pa].

I Inertia [$\mathrm{kg \cdot m^2}$].

L Length of rods [nm].

M_w Molecular weight [mg/ mol].

M_{min} Minimum torque [$\mathrm{N \cdot m}$].

NA Numerical aperture.

N_0 Initial number of RBCs.

N_A Avogadro's number $N_A = 6.02 \times 10^{23}\,\mathrm{mol}^{-1}$.

N_k Number of aggregates of length k.

N Number of aggregates.

P Pressure.

R_G Radius of gyration [nm].

R Resolution [nm].

S Entropy.

T Temperature.

U Internal energy.

V_{ex} Excluded volume.

V_{ov} Overlap volume.

V Volume.

W Interaction potential.

Δ_0 Depletion layer thickness without polymer ($c_d = 0\,\mathrm{mg/\,mL}$) [nm].

Δ Depletion layer thickness [nm].

δ Glycocalyx thickness [nm].

$\dot{\gamma}$ Shear strain rate [s^{-1}].

η Viscosity [$Pa \cdot \mathrm{s}$].

γ Shear strain of deformation.

λ Wavelength of (fluorescent) light [nm].

ν Frequency [s^{-1}].

ω Radial frequency [s^{-1}].

$\overline{k}$ Average number of RBCs per aggregate.

ϕ_{RBC} volume fraction of red blood cells.

ϕ_{col} volume fraction of colloids.

ϕ_d volume fraction of depletant.

ϕ_{fd} Volume fraction of fd-virus.

ϕ_p Volume fraction of polymer.

ϕ_r Volume fraction of rods.

ϕ Volume fraction.

ρ Density [g/ mL].

σ_y Yield stress [Pa].

σ Diameter of penetrable sphere [nm].

σ Stress [Pa].

θ Maximal half-angle of the light cone.

c^* Polymer overlap concentration [mg/ mL].

c_d^* Critical depletant concentration [mg/ mL].

c_d Depletant mass concentration [mg/ mL].

c_p Penetration constant of the polymer [mg/ mL].

c Speed of light $c = 3 \times 10^{17}\,\mathrm{nm/\,s}$.

d_f Fractal dimension.

h Separation between depleting colloids.

h Planck constant $h = 4.1 \times 10^{-15}\,\mathrm{eV \cdot\,s}$.

kDa kilo Dalton, atomic mass unit $1Da = 1.66 \times 10^{-21}\,\mathrm{mg}$.

k_B Boltzmann constant $k_B = 8.62 \times 10^{-5}\,\mathrm{eV}/K$.

k Number of RBCs per aggregate.

m probability to find a reacted group.

n_d Number density of depletant in bulk [mL^{-1}].

n Refractive index.

p Penetration depth of polymer into glycocalyx [nm].

q Size ratio of depletant over colloid size.

r_{CM} Centre of mass position.

w_m Mass fraction of aggregates.

Acronyms

fd Filamentous bacteriophage d.

APD Avalanche Photodiode.

AS Amplitude Sweep.

ATP Adenosine Triphosphate.

Dex Dextran.

DMA Dynamic Mechanical Analysis.

DNA Deoxyribonucleic Acid.

EDTA Ethylenediaminetetraacetic acid.

EMCC Erythrocyte Membrane-Cortical Cytoskeleton.

FN Fibrinogen.

FS Frequency Sweep.

Hb Haemoglobin.

HSA Human Serum Albumin.

HSCs Haematopoietic Stem Cells.

Ht Hematocrit [vol%].

HyD Hybrid pixel Detector.

LSCM Laser Scanning Confocal Microscopy.

PBS Phosphate Buffered Saline.

PBS-OP PBS with Optiprep.

PMT Photomultiplier Tube.

PSF Point Spread Function.

RBC Red blood cell.

RBCs Red Blood Cells also *Erythrocytes*.

RGB Red-Green-Blue.

SNR Signal-to-Noise Ratio.

TWS Trainable Weka Segmentation.

USM Unsharp Masking.

WBCs White Blood Cells or *Leukocytes*.

WEKA Waikato Environment for Knowledge Analysis.

List of Figures

2.1 Main cellular components (not to scale) of human blood in vivo. Image taken from Encyclopædia Brittanica [13] 4

2.2 Three distinctive phases of blood after sedimentation/ centrifuging. **(a)** graphical representation **(b)** Eppendorf 1.5ml tube after centrifuging blood with Phosphate Buffered Saline (PBS) at $500G$ for 5 min at room temperature. Due to small amounts of blood, the buffy coat is less visible 5

2.3 Schematic of plasma membrane of Red Blood Cells also *Erythrocytes* (RBCs). Size and concentration of components not to scale 6

2.4 Scanning electron microscope image of **(a)** Discocyte **(b)** Echinocyte **(c)** Stomatocyte **(d)** Spherocyte. Image **a-c** from [26] **d** from [27] 7

2.5 Rouleaux formation of erythrocytes in human blood. Image from S. Rowlands [30] 8

2.6 Bridging by Dextran (Dex) shows equal intercellular distance between RBCs, thus requiring membrane deformation [7, 36] 9

2.7 **(a)** If no macromolecules (e.g. Dextran) are present, there will be no bridging interaction. For macromolecule concentrations below the critical concentration c_d^*, a small percentage of the cell's surface is covered. **(b)** 50% of the Red blood cell (RBC)'s surface is covered in macromolecules at c_d^*, providing maximal bridging attraction. **(c)** Further increase in macromolecule concentration will saturate the surface, effectively creating a repulsive interaction where no macromolecules can bridge between neighbouring RBCs 10

2.8 Schematic drawing of RBC aggregation by depletion. The rods and coiled polymers are the depletant macromolecules that lose configurational entropy near the surface, creating an excluded volume V_{ex} around the cells, i.e. the depletion layer (dashed). The overlapping volume V_{ov} (green) reduces the total excluded volume, creating more space for depletant to migrate to. This gain in free volume increases as the cells move closer, effectively creating a net attractive interaction $W_d(h) = -P \cdot V_{ov}$ where P is the osmotic pressure by the depletant on the cells [31] **(a)** Coiled polymer depletant is a good representation of Dex $70kDa$, used in the experiments. Since the dextran molecule is small, the depletion layer will be smaller as well **(b)** Fd-virus is a hard rod depletant with a long length, creating a broader depletion layer 11

2.9 Depletion interaction potential per area between parallel plates W_d for hard rods (from eq. 2.15). **(a)** W_d in function of volume fraction of polymers ϕ_r for different h/Δ ratios. **(b)** W_d in function of distance between plates h for different polymer volume fractions ϕ_r 13

2.10 Depletion interaction potential per area between parallel plates W_d for ideal polymers (from eq. 2.18). **(a)** W_d in function of volume fraction of polymers ϕ_p for different h/Δ ratios. **(b)** W_d in function of distance between plates h for different polymer volume fractions ϕ_p 14
2.11 Depletion interaction potential per area W_d between RBCs due to the non-ideal polymer Dex 70kDa (from eq. 2.21) **(a)** W_d in function of concentration of depletant c_d for different distances h between RBCs **(b)** W_d in function of distance between cells h for different depletant concentration c_d 15
2.12 Depletion layer thickness Δ over polymer concentration c_d for Dex 70kDa. Calculated using equation 2.23 16
2.13 Schematic of the various macromolecules and RBC to scale. **(a)** From largest to smallest: semi-flexible rod Filamentous bacteriophage d (*fd*)-virus (ochre), rod like Fibrinogen (FN) (pink) and coiled polymer Dex 70kDa (green) **(b)** Segment of RBC plasma membrane with glycocalyx and macromolecules to scale 18
2.14 Three indications of RBC aggregation in function of dextran concentration, from Chien *et al.* [7] demonstrating the bell shape **(A)** Macroscopic Aggregation Index (MAI) **(B)** Erythrocyte Sedimentation Rate (ESR) **(C)** Relative viscosity (η_r) 20
2.15 The depletion interaction between attractive spheres and it's phase diagrams, image from Anderson en Lekkerkerker [64] **(a)** Interaction potential with hard sphere core and depletion attraction tail **(b)** Phase diagram for large polymer depletion shows three phase region (shaded). Percolation line added in red (long range interaction = solid line) **(c)** Phase diagram for short polymer depletion, similar to some systems with proteins it shows two-phase coexistence and metastable liquid-liquid (L + L) region. Percolation line added in red (short range = dashed line) 22
2.16 Particles connected by bonds form clusters. The blue cluster has percolated since it spans the entire matrix 23
2.17 Key concepts in rheology **(a)** Shear force F causes a displacement Δl and flow of the fluid between two parallel plates separated by h **(b)** Shear stress σ dependency on shear rate $\dot{\gamma}$ for important Newtonian and Non-Newtonian fluids 24
2.18 Characterisation and identification techniques for gels and percolated networks **(a)** Gel Dynamic Mechanical Analysis (DMA) frequency sweep on a SOS triblock-copolymer ion gel from He *et al.* [77]. Blue = gel, green = gel point, red = liquid **(b)** Whole blood shows non-zero yield stress σ_y for $Hematocrit[vol\%](Ht) = 41.6\%$ and $T = 37°C$. Image from Apostolidis *et al.* [73] **(c)** Graphical representation of g(r). Image from [78] **(d)** Paths in X (blue), Y (yellow) and Z (red) direction show direct percolation in confocal images 26

3.1 Schematic of parallel plate (PP) geometry, diameter D and gap h, with sample of RBCs. Twin drive system where geometries are rotated in opposite directions. Not to scale 32
3.2 Schematic diagram of the excitation light cone and in-focus excitation light in a Laser Scanning Confocal Microscopy (LSCM) 34
3.3 Obtaining images of focal planes at different depths allow for reconstruction of 3D objects **(a)** Schematic of LSCM scanning direction **(b)** 3D scan of RBC . 35

3.4 **(a)** Confocal image of discocyte RBC and it's reconstructed cross section. Scale bar is 2 µm **(b)** Sequence of RBC confocal images at different Z depths. Confocal scans consist of a 3D stack of images. **(c)** Confocal Z-stacks are used to recreate 3D objects e.g. a mesh reconstruction of a rouleaux of RBCs image (see section 3.4.3) 36

3.5 **(a)** Cross-sections as taken by confocal microscope **(b)** 3D representation of a *.tif* stack **(c)** The original 3D object is visible 37

3.6 **(a)** Original image **(b)** Gaussian blurring $\sigma = 1$ **(c)** Mean filter **(d)** Unsharp masking $\sigma = 1$, $M = 1$ **(e)** Rolling ball background subtraction with $r_{ball} = 20\ pixels$ 39

3.7 Ilastik environment: **(a)** brushstrokes (user input) to label individual cells (blue) and background (yellow) **(b)** output meshes used to generate 3D reconstruction of cells. 3D reconstruction in software program Meshlab [100] 40

3.8 **(a)** original confocal image **(b)** Manual classification of different objects as in step 2 **(c)** Classification by Trainable Weka Segmentation (TWS) as in step 3-4 **(d)** Classified image as in step 6 41

3.9 Principle of start (or end) plane identification. The cubes represent non-zero RBC voxels. **(a)** When it is required that the start planes contain more than 3 non-background voxels, the coloured cubes represent the start planes in X (blue), Y (red), Z (green) direction. **(b)** All voxels that connect to each other in a start (or end) plane, are represented by 1 *search pixel/node* 43

3.10 Different steps to identify search nodes in a 2D image: **(a)** Raw binary image needs filtering to remove noise; **(b)** Median filter removes isolated regions while retaining the binary nature of the image; **(c)**After skeletonisation, nodes with one or zero edges (black) are checked for internal paths; **(d)** Search nodes/pixels (green stars) are the minimal number of nodes that connect all nodes in that 2D plane 44

3.11 Generating a shell (here in 2D, for easier visualisation) of the image reduces the number of nodes and edges dramatically without losing nodes that describe the shape **(a)** Fully connected image **(b)** Connected shell (in 2D) **(c)** Multiple RBC voxels (partly indicated by the lattice) make up this cuboid object. Paths between pixels in the start and end plane in a fully connected image (red) go through the object's volume. Paths in the shell image (blue) follow the cuboid sides as the inside voxels are relabelled as background 46

3.12 Zoomed in percolated network. Different colours (Tab. 3.2) represent the paths in different direction through voxels 47

3.13 Percolation paths in three directions on a sample of red blood cells and Dextran ($\phi_{RBC} = 0.38,\ \ [Dex] = 50\,\mathrm{mg/mL}$) **(a)** Sample of RBCs with percolation paths **(b)** Percolation paths in X-direction **(c)** Percolation paths in Y-direction **(d)** Percolation paths in Z-direction 48

3.14 Flowchart that describes analysis of confocal images in this work 49

4.1 Phase diagram for RBC-Dex mixtures. Four distinct phases exist: Gas phase (G), Gas and Rouleaux phase (G+R), Branched Rouleaux phase (BR) and Percolation phase (P). Phase boundaries indicate the gas-aggregate transition and percolation transition. Error bars on data points are smaller than markers and thus not shown. Roman numerals refer to the corresponding confocal images. Link to original tiff stacks in the appendix A. 51
4.2 Network with mesh size 53
4.3 Gas phase (G) RBC mixtures with $[Dex] = [fd] = 0\,\mathrm{mg/mL}$ at different volume fraction ϕ_{RBC}. Roman numerals refer to data points in Fig. 4.1. Scale bar 10 µm 54
4.4 Packing of RBCs in a hexagonally packed rouleaux: **(a)** RBC plotted with Cassini equation 4.1; **(b)** Stacking of RBCs by stacking them in rouleaux with hexagonal packing 55
4.5 Gas phase (G) RBC-Dex mixtures at different volume fraction ϕ_{RBC} and concentration $[Dex]$. Roman numerals refer to data points in Fig. 4.1. Scale bar 20 µm 55
4.6 Gas-Rouleaux co-existence phase (G+R) RBC-Dex mixtures at different volume fraction ϕ_{RBC} and concentration $[Dex]$. Roman numerals refer to data points in Fig. 4.1. Scale bar 20 µm 57
4.7 Distribution of RBCs per rouleau k for RBC-Dex mixtures. Roman numerals refer to same data points in Fig. 4.1 **(a)** RBC mass fraction $w_m(k)$ in function of number of RBCs per rouleau k. Fitted with the Flory-Schulz distribution (eq. 4.4) **(b)** Average number of RBCs per rouleau $\overline{k}$ in function of ϕ_{RBC} . . 59
4.8 Branched Rouleaux phase (BR) RBC-Dex mixtures at different volume fraction ϕ_{RBC} and concentration $[Dex]$. Roman numerals refer to data points in Fig. 4.1. Scale bar 20 µm 60
4.9 Percolation phase (P) RBC-Dex mixtures at different volume fraction ϕ_{RBC} and concentration $[Dex]$. Roman numerals refer to data points in Fig. 4.1. Scale bar 20 µm 62
4.10 3D visualisation of RBC networks with percolation paths in RBC-Dex samples with $[Dex] = 50\,\mathrm{mg/mL}$. Total number of found paths in (X,Y,Z) direction. Roman numerals refer to data points in Fig. 4.1. Colours as defined in Tab. 3.2 63
4.11 XZ-Cross section of image XXI shows anchoring of rouleaux to the wall 64
4.12 Percolation analysis of sample XXV $\phi_{RBC} = 0.23$ and $[Dex] = 40\,\mathrm{mg/mL}$, image 4.9c 65
4.13 Calculating the radial distribution function: **(a)** raw image. Scale is 8 µm; **(b)** segmented cytosols. Scale is 8 µm; **(c)** $\frac{dN}{dr}$ in function of r for the RBC marked with yellow dot. $dr = 0.5\,\mu\mathrm{m}$; **(d)** $g(r)$ for the RBC marked with yellow dot. $dr = 0.5\,\mu\mathrm{m}$ 67
4.14 Phase diagram for RBC-*fd* mixtures. Three distinct phases are identified: Gas phase (G), Gas and Cluster phase (G+C) and Percolation phase (P). Phase boundaries indicate the gas-cluster transition and percolation transition. Error bars on the data points are smaller than markers and thus not shown. Roman numerals refer to the corresponding confocal images 68
4.15 Gas phase (G) RBC-*fd* mixtures at different volume fraction ϕ_{RBC} and concentration [*fd*]. Roman numerals refer to data points in Fig. 4.14. Scale bar 20 µm 69

4.16 Gas-Cluster co-existence phase (G+C) RBC-*fd* mixtures at different volume fractions ϕ_{RBC} and concentration [*fd*]. Roman numerals refer to data points in Fig. 4.14. Scale bar is 20 µm 70
4.17 Percolation phase (P) RBC-*fd* mixtures at different volume fraction ϕ_{RBC} and concentration [*fd*]. Roman numerals refer to data points in Fig. 4.14. Scale bar 20 µm 71
4.18 DMA on mixtures of RBCs and Dex with PP $D = 15\,\mathrm{mm}$ geometry and gap $h = 0.5\,\mathrm{mm}$. Grey regions indicate experimental boundaries 72

5.1 Normalised fluorescence intensity in function of depth of the channel measured on RBC-Dex mixtures and a sample of homogeneous Promofluor Premium 488 carboxylic acid dye in water (5%). Origin fixed at maxima 76
5.2 Enhanced discocyte-echinocyte transition in samples where RBCs are labelled with too much dye 77

List of Tables

2.1 Components of blood and their sub-components (in %). Based on [14] 5

3.1 Number of pixels that fit the criteria in image 3.10 45
3.2 Values and colours in the final percolation image for different combinations of voxels in the separate path images 47

4.1 Images classified by Waikato Environment for Knowledge Analysis (WEKA) segmentation. Table shows calculated and experimental volume fractions ϕ_{RBC}. The number of paths found by the percolation algorithm are given for X,Y and Z separate. †Percolation algorithm does not search all paths. These are too numerous and weren't found after 2 days. This simplified algorithm only checks whether percolation exist 66
4.2 Images classified by WEKA segmentation. Table shows calculated and experimental volume fractions ϕ_{RBC}. The number of paths found by the percolation algorithm are given for X,Y and Z separate 71

Contents

Preface i

Abstract iii

Popular summary v

Vulgariserende samenvatting v

Glossary ix

Acronyms xiii

List of Figures xv

List of Tables xxi

Contents xxiii

1 Introduction 1
- 1.1 Percolation of Red Blood Cells . . . 1
- 1.2 Outline of this work . . . 1

2 Red blood cell aggregation 3
- 2.1 Blood . . . 3
- 2.2 Red blood cells . . . 6
- 2.3 Aggregation mechanism . . . 9
  - 2.3.1 Bridging interaction . . . 9
  - 2.3.2 Depletion interaction . . . 11
  - 2.3.3 Summary of attractive interactions . . . 17
- 2.4 Aggregation macromolecules . . . 18
  - 2.4.1 FD-virus as long-range rod depletant . . . 19
  - 2.4.2 Dextran as short-range depletant . . . 19
- 2.5 Phase diagram of attractive colloidal spheres . . . 21
- 2.6 Description of percolated networks . . . 22
  - 2.6.1 Characterisation of colloidal gels . . . 23
- 2.7 Open questions . . . 27

3 Materials and methods **29**
3.1 Red blood cells sample preparation . . . 29
3.1.1 Phosphate Buffered Saline (PBS) . . . 29
3.1.2 PBS with Optiprep (PBS-OP) . . . 29
3.1.3 CellMask™ membrane stain . . . 30
3.1.4 RBC preparation . . . 30
3.1.5 Red blood cells dyeing with CellMask™ protocol . . . 31
3.1.6 Sample preparation RBC with macromolecules . . . 31
3.2 Rheology . . . 32
3.2.1 MCR 702 twin-drive Rheometer . . . 32
3.3 Confocal microscopy . . . 33
3.3.1 Background and introduction . . . 33
3.3.2 Laser Scanning Confocal Microscopy . . . 33
3.4 Image analysis . . . 37
3.4.1 Confocal images and raw data . . . 37
3.4.2 Image processing . . . 37
3.4.3 Ilastik individual cell segmentation . . . 39
3.4.4 Trainable Weka segmentation . . . 40
3.5 Data analysis and algorithms . . . 42
3.5.1 Volume fraction control . . . 42
3.5.2 Percolation algorithm . . . 42
3.6 Analysis flowchart . . . 49

4 Results and discussion **51**
4.1 RBC-dextran phase diagram . . . 51
4.1.1 Gas Phase . . . 54
4.1.2 Rouleaux Phase . . . 58
4.1.3 Rouleaux length distribution . . . 58
4.1.4 Branched Rouleaux Phase . . . 61
4.1.5 Percolation Phase . . . 63
4.2 RBC-*fd* phase diagram . . . 68
4.2.1 Gas phase . . . 69
4.2.2 Cluster phase . . . 69
4.2.3 Percolation phase . . . 71
4.3 Rheology of percolated networks . . . 72

5 Miscellaneous **75**
5.1 Depth limited confocal scanning . . . 75
5.2 Dye influenced echinocyte transformation . . . 76

6 Conclusion and outlook **79**

Bibliography **81**

Appendices **89**

A Additional material **91**

Chapter 1

Introduction

1.1 Percolation of Red Blood Cells

Blood is a complex fluid that fulfills the transportation of oxygen and carbon dioxide, nutrients and waste products throughout the body, and plays a critical role in thermoregulation and protection. The main cellular constituents of blood are Red Blood Cells (RBCs) whose unique biconcave shape and aggregating mechanism contribute heavily to the non-Newtonian rheological response of blood [1, 2]. Red blood cells aggregate with the addition of neutral macromolecules, like fibrinogen in whole blood [3, 4]. The interaction of these macromolecules with colloidal particles (like RBCs) is explained by two mechanisms: depletion [5, 6] or bridging [7]. Aggregated RBCs stack linearly to form one-dimensional crystals, rouleaux. Strong attractive interaction forces and a large amount of RBCs, allow for the composition of long rouleaux with other rouleaux branching outwards. Under the right conditions, these branched rouleaux can potentially form network structures that span large distances.

When aggregate structures grow to such sizes that they span the entire three-dimensional space, these structures become percolated and the system undergoes gelation. It is known that both bridging [8] and depletion [9] can be used to create colloidal gels of spherical particles. Whereas, phase diagrams for the different phases of colloidal sphere systems are well established, percolation on model systems of RBCs, with a carefully measured concentration of macromolecules, have not been studied before.

The detection of percolated networks is crucial for the determination of the phase transition into gelation. Four ways to detect percolation in a colloidal gel are: 1) Dynamic Mechanical Analysis 2) presence of a yield stress σ_y 3) the radial distribution function $g(r)$ and 4) direct detection. In this work, we predominately focus on the development of a technique to directly detect percolation of RBC networks in confocal image stacks.

1.2 Outline of this work

In this work we investigate mixtures of RBCs with short-range Dextran [10, 11] and long-range *fd*-virus [12] macromolecules. Aggregates of RBCs are imaged with laser scanning confocal microscopy and their flow behaviour is measured with a rheometer. This thesis marks the first time percolated structures of RBCs are identified directly by visualisation. Fur-

thermore, an overview of different aggregate phases is compiled into phase diagrams of the RBC-macromolecule systems.

The outline of this thesis is as follows:

Chapter 2 introduces the theoretical background on aggregation of red blood cells. First the role of blood in the human body and the properties of RBCs considered, where the second part is devoted to an overview of the aggregation mechanisms, bridging and depletion. The last part deals with percolated networks and the difference in phases for attractive colloidal spheres and RBCs.

Chapter 3 treats the daily sample preparation and experimental techniques in microscopy and rheology. Acquisition of confocal images, processing of said images and the final analysis methods are discussed.

Chapter 4 presents the results and measurements. This chapter begins with the identification of different phases in aggregation. Next, these individual phases are discussed and analysed. Later, rheological and miscellaneous measurements are described.

Chapter 5 offers results that, although not crucial to the topic of the thesis, can be of importance and help to future experimental work on RBC networks and aggregates

Chapter 6 finalises this work by presenting the conclusions and outlook into future experimental work on this topic.

Appendix A provides links to the confocal data and percolated networks used in this thesis, allowing the reader to more easily view the three-dimensional image stacks

Chapter 2

Red blood cell aggregation

2.1 Blood

Blood is the most important bodily fluid in humans and animals, serving multiple critical roles in maintaining life. Without blood, most animals cannot survive. Hereby, blood also has a deep root into culture and language. Blood brothers, blood oaths, *Blood is thicker than water* all dwell on the fact that one's blood provides one's life, implying large value to 'connection' through blood. On the opposite, we fear those creatures that rob others of their blood (and thus life) like bats, ticks and leeches. This general fascination of blood, combined with the medical importance of the substance, naturally lead to an interest among scientists to explore blood from a physical and rheological stance as well.

Blood fulfills three fundamental roles in the human body: *Transportation*, *Regulation* and *Protection*.
Red Blood Cells also *Erythrocytes* (RBCs) (from Greek *Erythros* for 'red' and *-cyte* for 'cell' as modern variation of *kytos* meaning 'hollow') are by far the most numerous type of cell found in blood. These cells' principal purpose is the transportation of oxygen (O_2) and carbon dioxide (CO_2) between the capillaries of the lungs and every other tissue and organ inside the human body. Through the elaborate network of arteries and veins, RBCs can navigate the entire body to deliver these gases and other vital nutrients. The second class of cells inside blood are White Blood Cells or *Leukocytes* (WBCs) (from Greek *Leuko* for 'white'). Leukocytes are part of the immune system that eradicates dangerous, foreign or domestic substances. To combat the various threats a body faces, blood contains different specialised WBCs. *Neutrophils* -most abundant type- primarily deal with bacteria and fungi, *Eosinophils* protect against larger parasites, *Basophils* regulate inflammatory response and *Monocytes* -largest- present pathogens to T cells for future recognition. *Lymphocytes* (T cell, B cells and NK cells) are also abundantly present in blood but can be found in much larger numbers in the lymphatic system. Finally, platelets or *thrombocytes* (from Greek *Thromvos* for clot) are the smallest cells of the blood that will form blood clots after injury. They use a glycoprotein Fibrinogen (FN) to form a platelet plug to repair damage to the vascular wall, contributing to the hemostasis.

Although cells realize the major functions, the main component of blood is plasma. Plasma accounts for 55% of the roughly 5 litres of blood in an average adult human body. The yellowish fluid is composed mainly of water (92%) and proteins. The major blood proteins (see also Tab.2.1) in plasma are the transport proteins *Albumins* (54-60%) followed by globulins

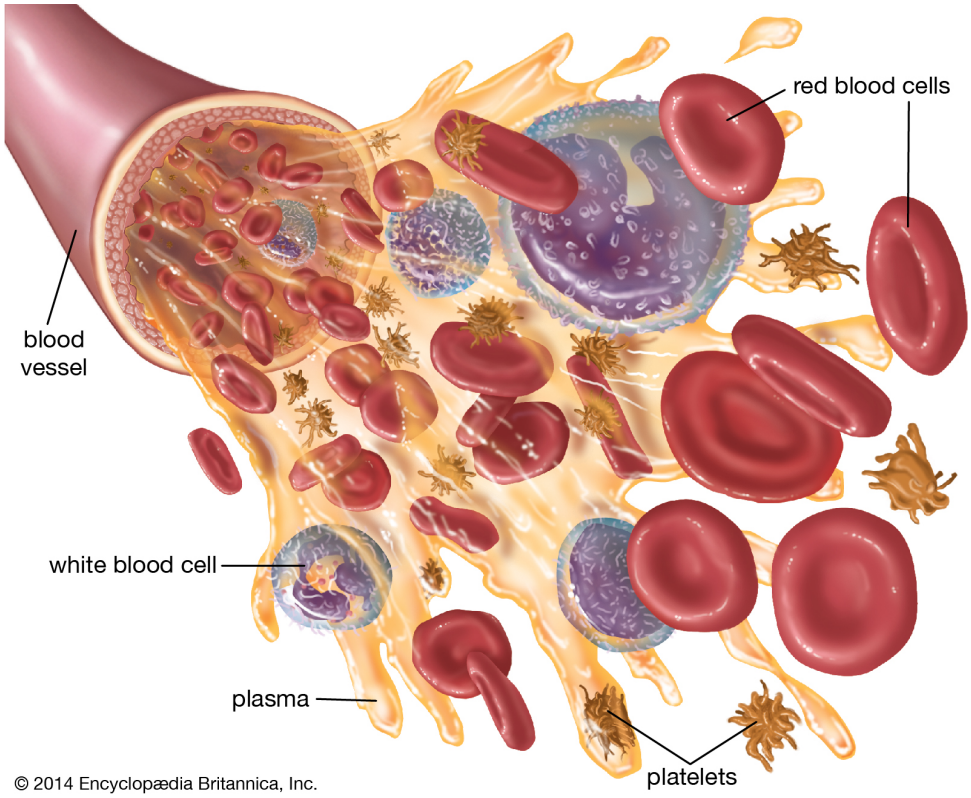

Figure 2.1: Main cellular components (not to scale) of human blood in vivo. Image taken from Encyclopædia Brittanica [13]

(35-38%) and coagulation protein *Fibrinogen* (4-7%). Minor components of the plasma are acquired from specific tissues or organs. These include nutrients like glucose, oxygen and carbon dioxide, amino acids and others (all <1%) that are also partially dissolved in the aqueous solution. Proteins in plasma serve different roles. Some examples are the FN used in clotting, Human Serum Albumin (HSA) being the most abundant and immunoglobulins (antibodies) are used to defend against pathogens.

Ensuing, blood flow is of great importance to the human body's thermoregulation. In warm environments, increased blood flow to the surface will lead to warmer skin and faster heat loss, resulting in cooling of the body. At last, blood flow also regulates pH and water content inside the body. The average pH of blood is regulated to be around $pH = 7.40$.

Compared to the physiological point of view, from a physical standpoint blood can be seen as a fluid exhibiting multiphase flow. The aqueous plasma ($\pm 55\%$) acts as the liquid phase, whereas the different cellular components (i.e. red blood cells, white blood cells and platelets) are regarded as the solid phase ($\pm 45\%$) as can be seen in figure 2.1. The volume percentage of RBCs is more often referred to as Hematocrit [vol%] (Ht) and varies for males between 41% and 50% while for females it lies between 36% and 46%.

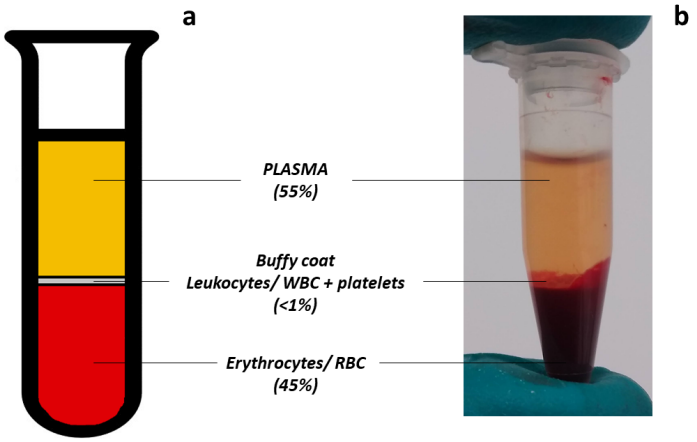

Figure 2.2: Three distinctive phases of blood after sedimentation/ centrifuging. **(a)** graphical representation **(b)** Eppendorf 1.5ml tube after centrifuging blood with PBS at $500G$ for 5 min at room temperature. Due to small amounts of blood, the buffy coat is less visible

When centrifuged or left to sediment, the heavier RBCs sediment at the bottom of the vials with the liquid, yellow plasma phase on top. The WBCs, that are less dense than the RBCs, form a white *buffy coat* in between as seen in figure 2.2. The solid phase cells are predominately RBCs (>98%) with in addition platelets (<1%) and WBCs (<1%).

Blood components (% of blood)	Sub-components (% of component)	Types (% of sub-component)
Plasma 46-63%	Water 92%	
	Proteins 6-7%	Albumin 54-60%
		Globulin 35-38%
		Fibrinogen 4-7%
	Other proteins and solutes <2%	hormones, enzymes, gases,...
Blood cells 37-54%	RBCs or erythrocytes >98%	
	WBCs or leukocytes <1%	Neutrophils, eosinophils, lymphocytes, ...
	platelets or thrombocytes <1%	

Table 2.1: Components of blood and their sub-components (in %). Based on [14]

2.2 Red blood cells

Red blood cells' shape and aggregating behaviour is profoundly significant for the phase behaviour and flow of whole blood.

Erythrocytes are produced in a process called *erythropoiesis* (from Greek *poiesis* 'to make') which is part of the overarching process of blood cell production: *Haematopoeisis* (from Greek *Aíma* for 'blood'). In contrast to children where erythropoiesis occurs in the bone marrow of most bones, for adult humans, erythropoiesis occurs only in the bone marrow of the vertebrae, ribs and some other bones. Inside this bone marrow, erythrocytes are differentiated from Haematopoietic Stem Cells (HSCs), the common ancestor of all mature blood cells. Besides RBCs, WBCs, lymphocytes and thrombocytes are also derived from the HSCs. After one day in the blood stream, immature RBCs are completely matured. During a red blood cell's life, their main task is O_2 delivery to cells through capillaries and CO_2 transport from those cells to the lungs. After circulating the bloodstream for about 100-120 days, RBCs are recycled by macrophages of the spleen and liver in a process called *eryptosis* (apoptosis is programmed cell death).

Mature red blood cells lose certain cellular components during erythropoiesis. The lack of a cell nucleus and other organelles permits them more room for packing Haemoglobin (Hb), increasing their capacity to carry O_2 and CO_2. Genome size and RBC size are directly correlated [15], so the absence of a nucleus allows mammals to have smaller RBCs than possible with nuclei. Along with the deficiency of genetic material in a nucleus, RBCs can not repair themselves, and thus have relatively short life cycles. Without mitochondria, the usual aerobic pathway of generating energy (Krebs Cycle) in cells is inhibited [16]. RBCs take the anaerobic Embden-Meyerhof pathway of producing Adenosine Triphosphate (ATP), thereby not converting the oxygen they carry.

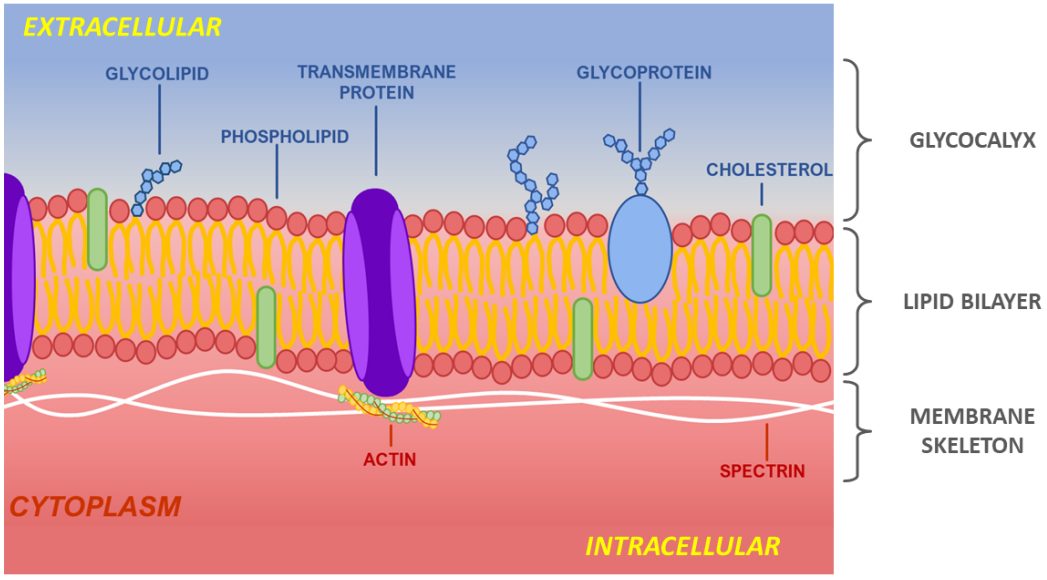

Figure 2.3: Schematic of plasma membrane of RBCs. Size and concentration of components not to scale

The two main components of RBCs are the flexible plasma membrane and the Hb-rich cytoplasm. A third of the RBC's volume is Haemoglobin (Hb), the iron-containing protein responsible for the cells' red colour which also provides binding sites for carrying O_2 and CO_2.

The cell membrane, on the other hand, consists of three distinctive layers: the glycocalyx, lipid-bilayer and membrane skeleton (see Fig. 2.3). The outermost layer, the glycocalyx, is a brush-like coat of glycoproteins and glycolipids. The length of this brush varies between $\delta = 5 - 10\,\mathrm{nm}$ [17]. Sialylated glycoproteins, part of the glycocalyx, are also responsible for the net negative surface charge that creates a repulsive ζ-potential between cells[18].
The second layer, lipid bilayer, comprises the actual lipid border between the intra- and extracellular environment. In addition to phospholipids and cholesterol, it also houses transmembrane proteins that allow the transport of substances in and out of the cell. The final, inner layer is the membrane skeleton. This Erythrocyte Membrane-Cortical Cytoskeleton (EMCC) is a 2D-network attached to the inside of the plasma membrane. It is a mesh of short actin filaments ($\sim$ 37 nm) connected by spectrin tetramers in a repetitive triangle pattern. The EMCC contributes to the distinctive biconcave shape of the RBCs and it's mechanical properties[19–21]. Other factors, i.a. pH, salt concentration, temperature, etc. also influence the deformability of the membrane and thus the shape of the cell. The deformability of RBCs is essential to squeeze the cells through narrow capillaries.

Shape is the most relevant property to the physical work on RBCs. Normal, healthy human erythrocytes are biconcave, disk like particles with a dimple in the centre, referred to as discocytes (see Fig. 2.4a). They have a diameter of 6.2-8.2 µm, with a thickness of 2-2.5 µm at the periphery and 0.8-1 µm in the centre. The distinctive biconcave shape maximises RBCs' surface area to volume fraction, where the average volume of a single RBC is 90 fL with a surface area of 140 $\mu\mathrm{m}^2$ [22, 23]. The cross-sectional shape of RBCs is approximated , using Cassini ovals [24]. RBC shape can be deformed under various conditions. The energy needed to deform a membrane from it's original curvature to another curvature, is represented in the bending modulus B of the membrane. In recent experiments, the bending modulus for RBCs is measured to be on the order of $B \sim 50 k_B T$ [25].

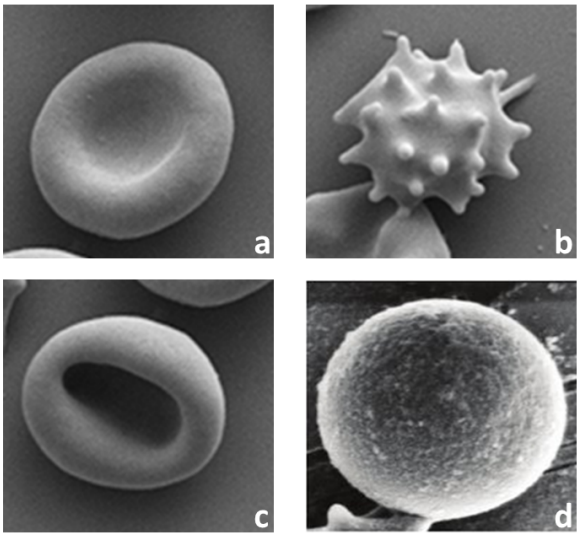

Figure 2.4: Scanning electron microscope image of **(a)** Discocyte **(b)** Echinocyte **(c)** Stomatocyte **(d)** Spherocyte. Image **a-c** from [26] **d** from [27]

The shape of RBCs depends strongly on the pH and tonicity. Since blood is pH-neutral, RBCs show a biconcave shape in solutions of $pH \sim 7.40$. Tonicity, on the other hand, indicates the amount of solutes present in certain solutions and thus effectively osmotic pressure. The presence of osmotic pressure can lead to water flowing between the intra- and extracellular environment through the semi-permeable cell membrane. A suspending medium with a higher number of solutes than the RBC's cytosol, is said to be hypertonic and water will flow out of the cell. The cell, thereby, will shrink to a shape that is called *echinocyte* (from Greek *echinos* for 'hedgehog'), see Figure 2.4b. In a hypotonic medium, on the contrary, a smaller number of solutes in the medium, compared to the cytosol, results in the swelling of RBCs. The flexible plasma membrane allows for the increasing of their volume to stomatocytes (Fig. 2.4c) or even spherocyte shape (Fig. 2.4d), up to 150 fL. An even further increase in volume can also lead to rupture of the cell membrane and cell death.

In blood, red blood cells take part in *RBC aggregation* and *coagulation*. It is important to distinguish these two processes. Where RBC aggregation is induced by charge-neutral macromolecules and is *reversible*, coagulation is not. In coagulation, or clotting, blood is transformed from a liquid to a gel like structure and the constituents are irreversibly clumped together. The mechanism behind coagulation depends on the maturation of fibrinogen into fibrin. Coagulated blood forms blood cloths that are composed of a spectrin network with coagulated platelets and RBCs, which is extremely useful in sealing wounds but also dangerous in blood cloth formation inside the circulatory system. Whereas RBCs in a blood cloth can not be separated again , RBC aggregation, on the other hand, is a *reversible* process, involving weaker interactions, that can be undone by shear deformation. In blood, plasma proteins, like FN, are also responsible for this aggregation in which RBCs attract each other under influence of depletion or bridging interaction. Aggregated RBCs stick to each other and tend to form rouleaux (see Fig. 2.5), i.e. stacks of RBCs, on the condition that the cells show discoid shape. Rouleaux formation and the subsequent break up of rouleaux is crucial to the understanding of blood flow [28]. Without break up, rouleaux can not pass capillaries with diameters smaller than a RBC's. Rouleaux break up further explains the shear thinning behaviour of whole blood, as will be further discussed in section 2.6.1. Rouleaux formation can also be an indicator for certain types of disease, e.g. plasma cell myeloma[29].

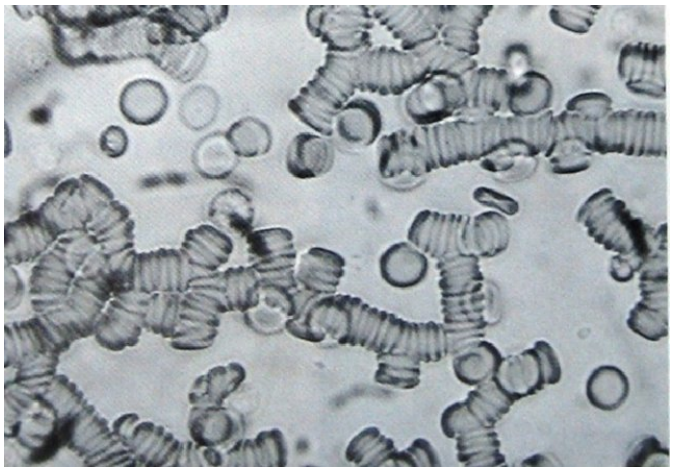

Figure 2.5: Rouleaux formation of erythrocytes in human blood. Image from S. Rowlands [30]

2.3 Aggregation mechanism

Aggregation of red blood cells happens in human blood under influence of plasma proteins. As early as the 1920s, Fahråeus [3] reported the aggregation of RBCs under influence of Fibrinogen (FN). Later, Merill [4] would further expand on the fibrinogen induced aggregation. It is important to distinguish the two processes of reversible *red blood cell aggregation* from irreversible *coagulation*.

Over the past 60 years, two mechanisms for RBC aggregation were put forward. Historically, the earliest theories focused mainly on aggregation by FN or Dextran (Dex). Chien and Merill [4, 7] worked on the bridging model for RBC aggregation.
The second mechanism, depletion, was only suggested for RBC aggregation later on. In the next section we focus on the different mechanisms behind RBC aggregation [6, 7, 31]

2.3.1 Bridging interaction

The bridging model is used to describe the attraction between red blood cells under influence of charge-neutral polymers. The first mention of this theory by Merril *et al.* [4] stressed the importance of fibrinogen in RBC-aggregation. Further work by Chien and Jan [7, 10, 32, 33] and Brooks [34, 35] shifted towards induced aggregation by charge-neutral Dextran. Bridging assumes the adsorption of macromolecules to the surface membrane of the cells [10] with the possibility of connecting neighbouring cells by the same macromolecule. When cells move closer together, they form more bridges which in turn will reduce the total free energy of the system and increase the interaction strength (Fig. 2.6).

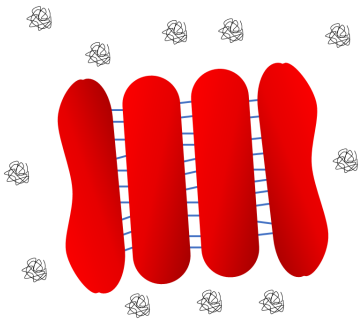

Figure 2.6: Bridging by Dex shows equal intercellular distance between RBCs, thus requiring membrane deformation [7, 36]

The negatively charged surface of RBCs opposes aggregation with a repulsive electrostatic force (F_e) between cells [32]. For colloids, this repulsive force decreases linearly with distance to the surface. In bridging aggregation, this repulsive force is overcome by a surface-bridging force (F_b) from adsorption of macromolecules to the cell surface. F_b is assumed to be dependent on the number of bridges formed, and thus the concentration of macromolecules. During rouleaux formation, two other forces will counter aggregation: mechanical bending forces in the membrane (F_m) and shear forces during flow (F_s) [34, 37]. Bringing together these terms

$$F_a = F_b - F_e - F_s - F_m \tag{2.1}$$

represents the total aggregation force F_a as proposed by Chien [7]. The surface-binding force F_b is proportional to

$$F_b \sim f_b n A \tag{2.2}$$

f_b the adsorption force per bond, n the number of bridging macromolecules per cell surface area and A the total surface area. The intercellular distances between RBCs were found

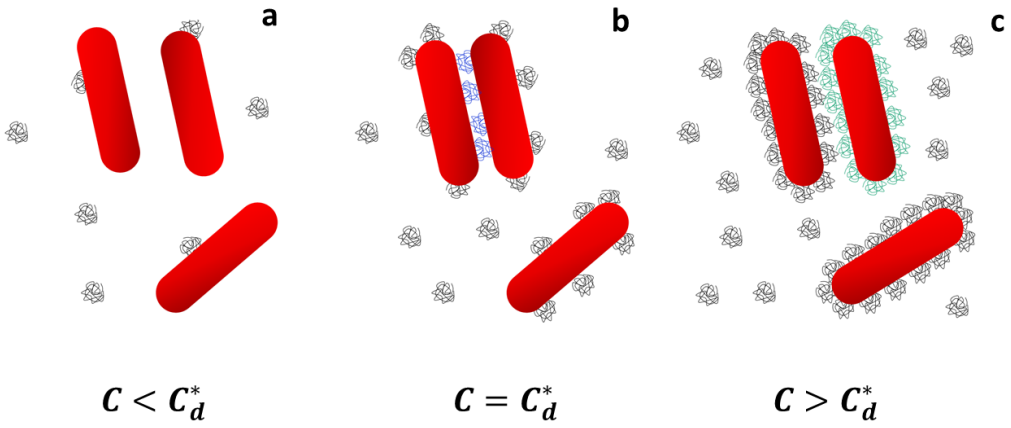

Figure 2.7: **(a)** If no macromolecules (e.g. Dextran) are present, there will be no bridging interaction. For macromolecule concentrations below the critical concentration c_d^*, a small percentage of the cell's surface is covered. **(b)** 50% of the RBC's surface is covered in macromolecules at c_d^*, providing maximal bridging attraction. **(c)** Further increase in macromolecule concentration will saturate the surface, effectively creating a repulsive interaction where no macromolecules can bridge between neighbouring RBCs

to be shorter than the corresponding Dex contour length [7]. Thus, macromolecules in the intercellular space tend to be coiled up. Furthermore, there exists a minimal molecular size for macromolecules to induce aggregation, explaining why e.g. Dex 10 and 40kDa reduce aggregation instead of inducing it like Dex 70kDa [38]. In more recent work on clay particles by Swenson *et al.* [39] and on RBCs by Barshtein *et al.* [40], it was found that the bridging macromolecules would be partly stretched when holding the colloids together. They also point to a critical macromolecular concentration for maximal bridging attraction. As seen in figure 2.7, an overabundance of macromolecule adsorption creates a repulsive layer, reducing the possibility of aggregation. The aggregation strength thus follows a bell shaped dependence on macromolecule concentration, as seen for Dex in figure 2.14. Nowadays, a different model for the surface-binding force is proposed, a spring model [36]. They assume the force per bond

$$f_b = k(l - l_0) \tag{2.3}$$

where k is the spring constant an l and l_0 respectively the stretched and unstretched length of the macromolecule. Furthermore, the total aggregation force per unit length becomes

$$f_a = k(l - l_0)\ n_b \frac{x}{l} \tag{2.4}$$

with x the distance between cells and n_b the density of bonds that holds to the reaction equation

$$\frac{\partial n_b}{\partial t} \propto \tau_{br} \left(n - \frac{n_b}{2} \right)^2 \tag{2.5}$$

where n is the density of the cross-linking molecules on each cell and τ_{br} the lifetime of a bridge

$$\tau_{br} = \tau_{br,0} \exp\left(\frac{k(l-l_0)^2}{k_B T}\right) \tag{2.6}$$

with $\tau_{br,0}$ the lifetime at equilibrium.

2.3.2 Depletion interaction

Depletion interaction was first proposed by Asakura and Oosawa in the 1950s [5] for attraction between two parallel plates due to spherical solute molecules. It later would find usefulness in colloidal physics where it was studied extensively by Vrij [41] and Vincent *et al.* [42–45]. Vincent's works expanded the original idea for hard sphere colloids into models for soft spheres. Apart from a mention of Dextran exclusion volume by Chien [46], the possibility of depletion-induced RBC aggregation had not been extensively studied until the works of Evans, Bäumler, Meiselman, Neu and others [6, 47–49].

Depletion is a model to describe attraction of large colloidal particles through the addition of non-adsorbing solute particles, depletants. Depletion force is of pure entropic nature. The smaller macromolecule depletants lose configurational entropy near the surface of the colloids compared to the bulk solution. Subsequently, maximising entropy, a layer with fewer depletant molecules than the bulk will form: the depletion layer. This region around the colloids is referred to as the excluded volume V_{ex}. As the excluded volumes of two neighbouring colloids start to overlap, the available volume for depletants increases. Effectively, overlap volume V_{ov} is responsible for an osmotic pressure difference: the driving force behind the attractive depletion interaction.

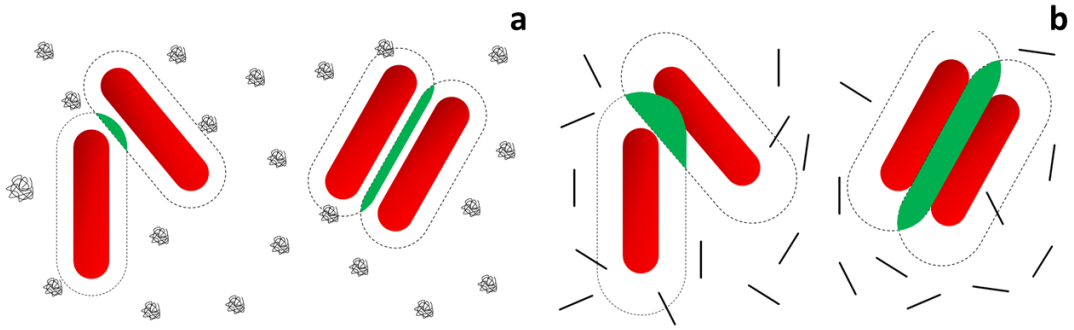

Figure 2.8: Schematic drawing of RBC aggregation by depletion. The rods and coiled polymers are the depletant macromolecules that lose configurational entropy near the surface, creating an excluded volume V_{ex} around the cells, i.e. the depletion layer (dashed). The overlapping volume V_{ov} (green) reduces the total excluded volume, creating more space for depletant to migrate to. This gain in free volume increases as the cells move closer, effectively creating a net attractive interaction $W_d(h) = -P \cdot V_{ov}$ where P is the osmotic pressure by the depletant on the cells [31] **(a)** Coiled polymer depletant is a good representation of Dex $70kDa$, used in the experiments. Since the dextran molecule is small, the depletion layer will be smaller as well **(b)** Fd-virus is a hard rod depletant with a long length, creating a broader depletion layer

As depletion layers overlap, a lower osmotic pressure will be experienced between the colloids than outside, leading to the same attractive interaction. Maximising contact area between the colloids, maximises the total depletion force.

From a thermodynamic point of view, attraction through depletion arises from a change in the Helmholtz free energy F

$$W = \Delta F = \Delta U - T\Delta S = -T\Delta S \tag{2.7}$$

where W denotes the interaction potential, T temperature, S entropy and $\Delta U = 0$ internal energy. With the help of the fundamental equation in thermodynamics $dU = TdS - PdV$ and the volume difference due to excluded volume, the interaction potential can be described as

$$W(h) = -P\Delta V = -P\big(V_{ex}(h \to \infty) - V_{ex}(h)\big) \tag{2.8}$$

where h is the separation between the colloids and P the difference in osmotic pressure between the bulk and overlap region. Osmotic pressure is given by Van 't Hoff equation

$$P = n_d k_B T \tag{2.9}$$

with n_d the number density of depletant macromolecules and k_B the Boltzmann constant. This number density is found from the molecular weight M_w [mg/ mol] and mass concentration c_d [mg/ mL] of depletant

$$n_d = \frac{N_A}{M_w} c_d \tag{2.10}$$

where N_A is Avogadro's number.
The depletion force F_d is found from the derivative of the potential with respect to the distance between colloids [31].

$$F_d = -\frac{\partial W_d}{\partial h} \tag{2.11}$$

As with bridging, the total aggregation force F_a in RBCs will be the sum of the attractive depletion force F_d and the repulsive forces F_e, F_s, F_m

$$F_a = F_d - F_e - F_s - F_m \tag{2.12}$$

were, in case of stationary samples, we assume $F_s = 0$. Also, the electrostatic repulsion and mechanical bending forces will not be of interest in this work, thus we take $F_e = 0$, $F_m = 0$. In this work, we focus on the influence of RBC volume fraction ϕ_{RBC} and polymer/depletant volume fraction (concentration of depletant) ϕ_d (c_d) on the phase behaviour of the mixture. Therefore, the depletion interaction potential will be determined for the case of rod-like depletant (Fd-virus) and coiled polymer depletant (Dextran).

Depletion between parallel plates due to ideal rods

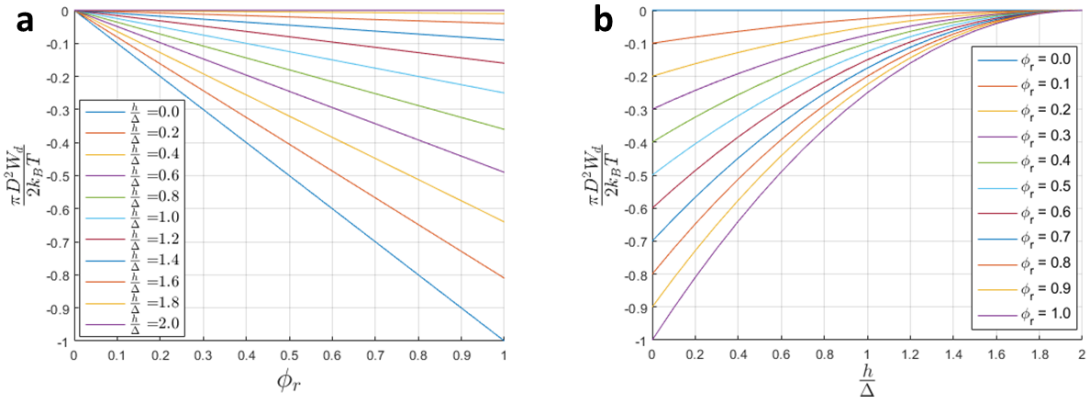

Figure 2.9: Depletion interaction potential per area between parallel plates W_d for hard rods (from eq. 2.15). **(a)** W_d in function of volume fraction of polymers ϕ_r for different h/Δ ratios. **(b)** W_d in function of distance between plates h for different polymer volume fractions ϕ_r

.

The depletion interaction potential per unit area W_d of two parallel plates induced by ideal rods [50] is

$$W_d(h) = \begin{cases} -\frac{1}{2} n_d k_B T \frac{(L-h)^2}{L} & 0 \leq h \leq L \\ 0 & h > L \end{cases} \tag{2.13}$$

where h is the distance between the plates and L is the length of the thin rods. Rewriting this in function of the volume fraction of rods

$$\phi_r = \frac{\pi}{4} L D^2 n_d \tag{2.14}$$

we find

$$W_d(h, \phi_r) = \begin{cases} -\frac{2}{\pi} \frac{k_B T}{D^2} \phi_r \left(1 - \frac{h}{2\Delta}\right)^2 & 0 \leq h \leq 2\Delta \\ 0 & h > 2\Delta \end{cases} \tag{2.15}$$

The depletion layer thickness Δ is $L/2$ for ideal rods.

Fd-virus resembles a thin ideal rod-like depletant molecule, and is used in our experiments at volume fractions of $\phi_{fd} = 0 - 0.011$. In section 2.4.1, the characteristics of *fd* are discussed. Figure 2.9 shows the linear dependence of the depletion interaction potential W_d on volume fraction of hard rods ϕ_r and that same potential in function of distance h between parallel plates/cells.

Depletion between parallel plates due to ideal polymers

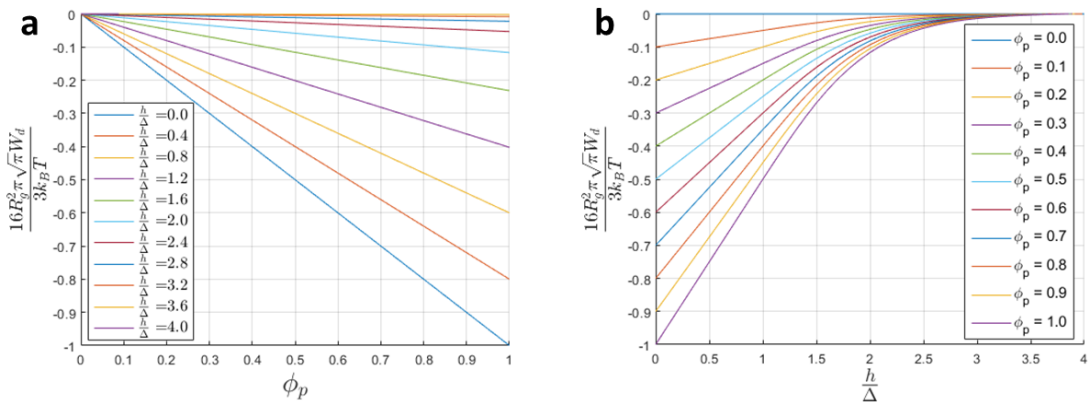

Figure 2.10: Depletion interaction potential per area between parallel plates W_d for ideal polymers (from eq. 2.18). **(a)** W_d in function of volume fraction of polymers ϕ_p for different h/Δ ratios. **(b)** W_d in function of distance between plates h for different polymer volume fractions ϕ_p

.

The depletion interaction potential per unit area W_d of two parallel plates induced by ideal polymers [50] is

$$W_d(h) = \begin{cases} -n_d k_B T \left[\frac{4R_G}{\sqrt{\pi}} - h - \frac{8h}{\pi^2} e^{-\frac{\pi^2 {R_G}^2}{h^2}} \right] & 0 \leq h \leq \frac{8R_G}{\sqrt{\pi}} \\ 0 & h > \frac{8R_G}{\sqrt{\pi}} \end{cases} \tag{2.16}$$

with R_G the radius of gyration. The depletion layer thickness Δ and volume fraction ϕ_p for ideal polymers are given by [50]

$$\Delta = \frac{2R_G}{\sqrt{\pi}} \qquad \phi_p = \frac{4}{3}\pi {R_G}^3 n_d \tag{2.17}$$

Combining equations 2.16 and 2.17 we find

$$W_d(h, \phi_p) = \begin{cases} -\frac{3k_BT}{16\pi\sqrt{\pi}{R_G}^2}\phi_p \left[1 - \frac{h}{2\Delta} + \frac{4h}{\pi\Delta} e^{-\frac{\pi^3\Delta^2}{4h^2}} \right] & 0 \leq h \leq 4\Delta \\ 0 & h > 4\Delta \end{cases} \tag{2.18}$$

The interaction for ideal polymers can also be described by treating the depletant as penetrable hard spheres with diameter σ

$$\sigma = \frac{4R_G}{\sqrt{\pi}} \tag{2.19}$$

as was done by Eisenriegler [51]. The relationship between the radius of gyration R_G [nm] and the molecular mass M_w [mg/ mol] is described as [52]

$$R_G(\,\mathrm{nm}) = 3.385 \times 10^{-3} \cdot {M_w}^{0.43}(\,\mathrm{mg/\,mol}) \tag{2.20}$$

where the factor 0.43 is due to the coiled nature of the polymer. Figure 2.10 shows the linear dependence of the depletion interaction potential W_d on volume fraction of ideal polymers ϕ_p and that same potential in function of distance h between parallel plates/cells.

Depletion of soft particles due to non-ideal polymers

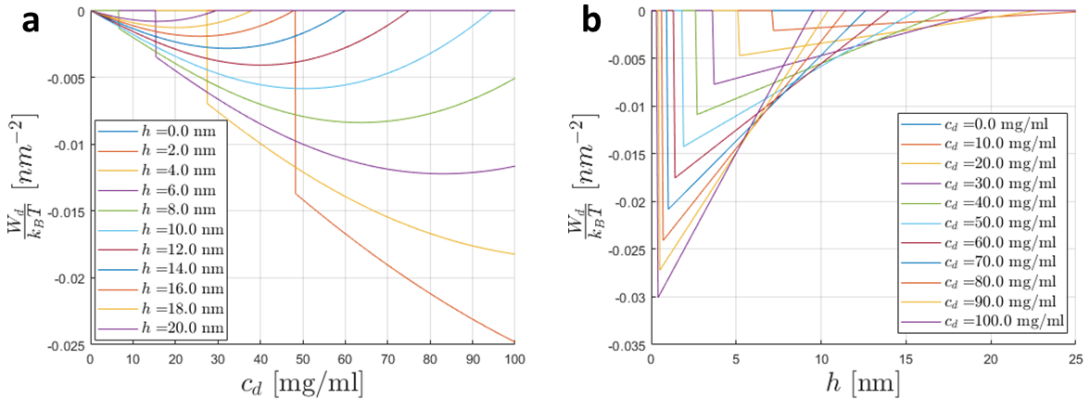

Figure 2.11: Depletion interaction potential per area W_d between RBCs due to the non-ideal polymer Dex $70kDa$ (from eq. 2.21) **(a)** W_d in function of concentration of depletant c_d for different distances h between RBCs **(b)** W_d in function of distance between cells h for different depletant concentration c_d

Assuming that the Dextran-RBC interaction behaves like the parallel plates interaction due to ideal polymers, would neglect some key characteristics of the interaction. Dextran is not an ideal polymer, but it's coiled shape can enter a certain depth into the RBC's glycocalyx. As mentioned before, it was Vincent *et al.* [42–45] that further developed a theory to explain depletion interactions between soft particles and free polymer. Hereafter, we follow the approach of Neu and Meiselman [6] for depletion interaction between RBCs due to free (coiled) polymer.

The interaction potential per unit area W_d for RBCs, that have a 'soft' or 'hairy' surface (coated in glycocalyx macromolecules), is

$$W_d(h) = \begin{cases} -2P\left(\Delta - \frac{h}{2} + \delta - p\right) & 0 \leq \frac{h}{2} - \delta + p \leq \Delta \\ 0 & else \end{cases} \tag{2.21}$$

where Δ is the depletion layer, P the osmotic pressure, δ the glycocalyx thickness and p the penetration depth of the polymer into the glycocalyx. Neu and Meiselman [6] then elaborate each of these terms.

The osmotic pressure P for the non-ideal polymer was calculated using the virial expansion up to second order:

$$P = N_A k_B T \left(\frac{c_d}{M_w} + A_2 {c_d}^2\right) \tag{2.22}$$

where (apart from the usual variables) $A_2 = 0.404 \times 10^{-9}\,\frac{\text{mL mol}}{\text{mg}^2}$ is the second virial exponent for Dex $70kDa$ [53].

Further, the approach of Vincent [45],based upon calculation of the equilibrium between the elastic free energy and the osmotic force experienced by polymer chains at a non-absorbing

surface, was used to find the depletion layer thickness Δ

$$\Delta = \frac{1}{2}\sqrt{\left(\frac{P}{D}\right)^2 + 4\Delta_0^2} - \frac{1}{2}\frac{P}{D} \qquad D = \frac{2k_BT}{\Delta_0^2}\left(\frac{c_d N_A}{M_w}\right)^{2/3} \tag{2.23}$$

with $\Delta_0 = 1.4R_G$ the depletion layer thickness in absence of depletant polymer and D a constant.

The penetration depth p of the polymer into the glycocalyx depends on the interaction between the polymer and the glycocalyx, molecular size and concentration of the polymer. The exact interaction between polymer and glycocalyx is still unknown but an exponential is used to describe the behaviour

$$p = \delta\left(1 - e^{-\frac{c_d}{c_p}}\right) \tag{2.24}$$

where c_p is the penetration constant. Although the glycocalyx can compress under osmotic pressure, δ is assumed to be constant here. Since p increases with c_d and $W_d = 0$ for $h < 2(\delta - p)$, we observe a cut-off in figure 2.11.b. Combining eqs. (2.21) and (2.24) explains the cut-off in figure 2.11.a where $W_d = 0$ for $c_d < c_p \ln \frac{2\delta}{h}$.

Figures 2.11 and 2.23 are constructed for Dextran (Dex) $70kDa$. In experiments, the polymer is used at volume fractions of $\phi_p = 0 - 1.84$. In section 2.4.2, the properties of Dextran are presented. Furthermore we assume a glycocalyx thickness of $\delta = 5\,\mathrm{nm}$ and penetration constant of $c_p = 30\,\mathrm{mg/\,mL}$.

In the depletion interaction between soft particles (RBCs) and non-ideal polymers, the depletion layer thickness decreases with added concentration of polymer c_d, as seen in figure 2.12.

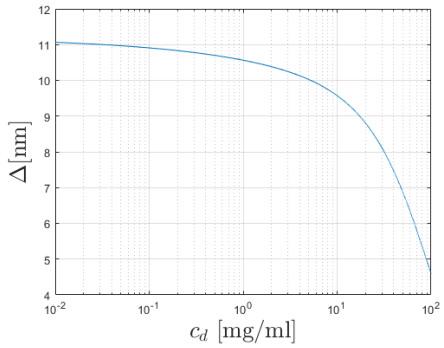

Figure 2.12: Depletion layer thickness Δ over polymer concentration c_d for Dex $70kDa$. Calculated using equation 2.23

This model for depletion interaction between RBCs is particularly useful for it's prediction of bell-shaped interaction. As seen in figure 2.11.a, the depletion interaction potential does not just increase linearly with the concentration of depletant, but rather has a critical value c_d^* where the aggregation is strongest. At higher c_d, the interaction decreases again. The resulting, bell-shaped, behaviour has been observed in multiple studies into RBC aggregation [7, 33]. Dextran induces such bell-shaped behaviour, seen in figure 2.14. Further, the glycocalyx thickness δ and penetration depth p both influence the aggregation by shifting the

critical concentration c_d^* towards lower concentrations. The restabilisation of the system could also be related to the network of polymers that is formed at concentrations above the overlap concentration c^*

$$c^* = \frac{3M_w}{4\pi N_A {R_G}^3} \tag{2.25}$$

that coincides with c_d^* for dextran, as described by Korculanin [14].

2.3.3 Summary of attractive interactions

The two models, used for describing the attraction between red blood cells due to neutral macromolecules, are the Bridging and Depletion model.
The bridging model supposes that the macromolecules attach to the RBCs' surface and thus form connecting 'bridges' between cells. The strength of the interaction depends on the number of bridges and the strength per bridge. The size of macromolecules influences the strength of the bridging interaction. Furthermore, bridging requires bending of the red blood cell's membrane
On the other hand, the depletion model does not necessarily assume the adsorption of macromolecules to the cell's surface. The depletants experience steric hindrance near the surface of the colloidal particles i.e. RBCs, that will lead to the formation of a depletion layer. Overlapping depletion layers will lead to a net attraction between the colloids, since there is a non-uniform osmotic pressure between the bulk of depletant and the overlap volume. The size of the depletion depends strongly on the type of macromolecule used, as well as it's size.
Although both models can be used to explain the bell-shaped aggregation strength for Dex, the observation that intercellular distance depended not on c_d but on the molecular size of dextran led Chien [7] to believe that bridging caused RBC-Dex aggregation.

The exact aggregation mechanism for RBCs is heavily debated and, of course, dependent on the depletant macromolecules. In recent work by Korculanin [14], the disaggregation forces between two aggregated red blood cells were measured using optical tweezers. The disaggregation forces could then be related to the aggregation forces by cause of bridging or depletion. They performed this experiment for *fd* virus and Dextran (Dex) 70kDa. Lee *et al.* [54] did the same for the plasma protein fibrinogen.

Dex 70kDa appears not to be a pure depletant. The macromolecule shows a mixture of both depletion and bridging attraction.

Fd, on the other hand, is a pure depleting macromolecule with a linear concentration-aggregation strength dependence. The depletion model due to hard rods is in good agreement with the fd-macromolecule, confirming that hard rods are excellent depletion agents, as already recognised by Asakura and Oosawa [5].

In this work, we focus on the phase behaviour of RBC aggregation in function of both volume fractions of RBCs ϕ_{RBC} and the volume fraction (or concentration) of macromolecular polymers ϕ_p. We hypothesise that the nature and range of the interaction plays a key role in the aggregate phases that form.

2.4 Aggregation macromolecules

The main macromolecule of physiological importance is Fibrinogen (FN). Aggregation of RBCs in the body significantly depends on the amount of FN present as shown by Fahråeus and Merill [3, 4]. It is a glycoprotein that can be found in blood plasma after production by hepatocyte cells in the liver. Further, fibrinogen has a molecular mass of $340kDa$, rod-like shape with concentrations of 1.5-4 mg/ mL in a healthy human blood. The molecule consists of three nodules (Fig. 2.13) connected by a thin thread, diameter $D = 0.8 - 1.5\,\mathrm{nm}$. The nodules have a diameter of $5 - 7\,\mathrm{nm}$ and the length of the dried molecule was measured to be $L = (47.5 \pm 2.5)\,\mathrm{nm}$ [55].

Although fibrinogen is the obvious physiologically relevant aggregation agent, other aggregation agents are often used to study RBC aggregation. The first reason why, is the complex nature of FN. Depletion and bridging interactions have been described mathematically for hard rods, hard spheres, coiled polymers,... Fibrinogen, however, display a more intricate shape through the presence of the three nodules. A second, more important reason, is to clearly separate aggregation from coagulation. FN is also the main plasma protein responsible for coagulation, so studying aggregation with FN could potentially be influenced by coagulating behaviour.
Therefore, different macromolecules are used to replicate the aggregation between red blood cells (see Figure 2.13). It is essential to recognise that the sizes of the macromolecules (and thus the interaction range) is on a totally different scale than the colloids i.e. the red blood cells. In this work, we use Dextran (Dex) $70kDa$ and Filamentous bacteriophage d (*fd*) virus.

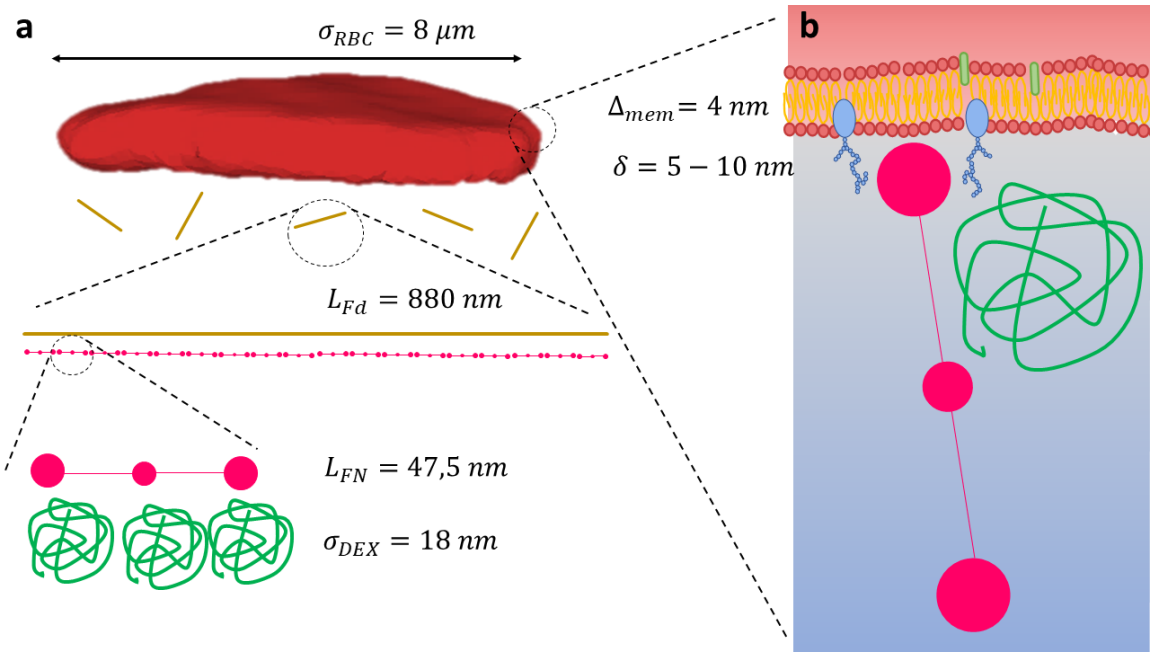

Figure 2.13: Schematic of the various macromolecules and RBC to scale. **(a)** From largest to smallest: semi-flexible rod *fd*-virus (ochre), rod like FN (pink) and coiled polymer Dex $70kDa$ (green) **(b)** Segment of RBC plasma membrane with glycocalyx and macromolecules to scale

2.4.1 FD-virus as long-range rod depletant

Filamentous bacteriophage d (*fd*) is a rod shaped virus with length $L = 880\,\mathrm{nm}$ and diameter $D = 6.6\,\mathrm{nm}$. The virus, originally isolated from raw sewage [56], is grown from an E. Coli (XL1-Blue) host. *Fd* as a depletion agent will induce long-range depletion [12, 57, 58] interaction through it's long length (see fig. 2.13). *Fd* is part of the family of filamentous bacteriophages, viruses that infect bacteria. The core of the virus consists of single stranded Deoxyribonucleic Acid (DNA) with a coat made of viral proteins. It is also negatively charged, like the RBCs. Due to this relative simplicity, *fd* lends itself as a perfect model system to study both biological and physical phenomena. Furthermore, the depletion interaction for rods is many times larger than for spherical depletant at the same volume fraction [59]. As seen in figure 2.8, the excluded volume V_{ex} increases when depletants are larger. Also from equation 2.13 it's seen that the interaction strength increases linearly with length L of the rod. Since the depletion layer thickness is $\Delta = L/2 = 440\,\mathrm{nm}$, *fd* is a long-range depletant. Additionally, *fd* is a very effective depletant because the rod like macromolecule has a very small volume. Small volume fractions of *fd* can thus already induce strong aggregation.

In recent work by Korculanin *et al.* [14], *fd* was used for the first time to induce RBC aggregation. They showed a quantitative analysis of the different possible aggregation forces by studying the cellular interaction kinetics in an holographic optical tweezers experiment. *Fd* was shown to induce RBC aggregation via pure depletion, since *fd* is not adhering to the cells. Additionally, the strength of the attraction increases linearly with concentration. Therefore, *fd* is an important tool to study RBC aggregation due to pure depletion of rods.

The molecular weight of *fd* measures $M_w = 1.64 \times 10^{10}\,\mathrm{mg/\,mol}$ [56, 60, 61] and the persistence length is 2.2 µm, making it a semi-flexible rod. In this work, the macromolecule is suspended in Phosphate Buffered Saline (PBS) at concentrations $c_d = 0 - 10\,\mathrm{mg/\,mL}$

2.4.2 Dextran as short-range depletant

Dextran (Dex) is a complex polysaccharide of varying molecular weight ($10 - 10^3 kDa$) and thus length. The type of dextran used in RBC related research has a main chain of consecutive α(1,6)-linked glucosyl with side chains [11]. Free dextran molecules exist in a coiled polymer shape. Dextran is a commercially important polysaccharide with applications mainly in the medical field as synthetic plasma substitutes. For this role, Dextran $70kDa$ is an important medication in the health system. Further, research by Chien *et al.* [7, 10] proved that Dex can also induce RBC aggregation. It is shown that the aggregation strength and intercellular distance in aggregates increases with molecular weight of the dextran used. In contrast the intercellular distance does not depend on the concentration of dextran. An important difference between Dex and *fd* is the bell-shaped RBC aggregation dependence on macromolecule concentration (Fig. 2.14 and section 2.3.2). There exists a critical concentration of dextran above which the aggregation strength will restabilise. Both bridging [7, 10] and depletion [6] mechanisms are used to explain this bell-shaped behaviour. For depletion: above this concentration, dextran cannot be simply treated as individual coiled spherical particles, but the molecules start to entangle. The attraction will interact on the length scale of the entangled polymer mesh, rather than the radius of gyration R_G.
The bridging model also explains the bell shaped aggregation behaviour. Chien *et al.* [10]

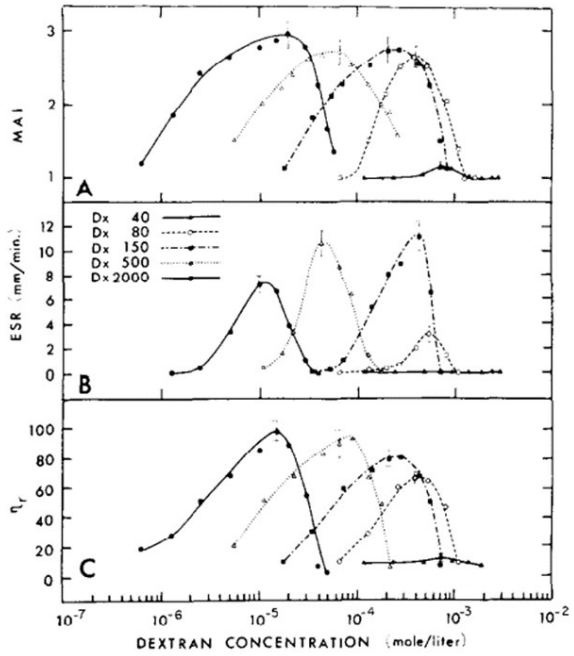

Figure 2.14: Three indications of RBC aggregation in function of dextran concentration, from Chien *et al.* [7] demonstrating the bell shape **(A)** Macroscopic Aggregation Index (MAI) **(B)** Erythrocyte Sedimentation Rate (ESR) **(C)** Relative viscosity (η_r)

showed that dextran molecules can attach to RBCs' surface and thus bridge. An overabundance of dextran then leads to a saturation of the RBC membrane, creating a steric repulsive polymer layer. At high concentrations of dextran, the bridging interaction would thus also decrease in strength.

In recent work by Korculanin *et al.* [14], Dex is shown to be neither an ideal depletant nor an ideal bridging macromolecule.

In this work, we use Dex $70kDa$ in Phosphate Buffered Saline (PBS) at concentrations $c_d = 0 - 100\,\mathrm{mg/\,mL}$. It has an overlap/critical concentration of $c^* = c_d^* = 54\,\mathrm{mg/\,mL}$. The radius of gyration $R_G = 8\,\mathrm{nm}$ ($\sigma = 18\,\mathrm{nm}$) ensures the short range of the interaction.

2.5 Phase diagram of attractive colloidal spheres

Colloidal interactions can be attractive or repulsive, long or short ranged, and the corresponding phase diagram depends on the aspects of this interaction. In this work, we study red blood cells (colloidal particles) with Dex or *fd* (polymer macromolecules),inducing short and long range interactions, respectively. As stated in section 2.3.2 and 2.3.2, the electrostatic repulsion is assumed to be negligible, thus we treat the interaction of the RBCs as hard particles with only an attractive potential part. Hence, only phase diagrams of attractive colloidal particles will be reviewed hereafter.
Colloidal spheres are simple model systems that show the elemental concepts in attractive particle phase diagrams. In case polymers are used as depletion agents, a phase diagram (Fig. 2.15) represents the various phases of material that exist at different volume fractions of polymer ϕ_p and colloids ϕ_{col}. The strength of the depletion (and bridging) interaction between colloids depends on ϕ_p. In absence of polymers, the interaction between colloids is just the hard core repulsion. At low ϕ_{col}, colloid suspensions are in the dilute regime where no aggregates exist and the colloids behave like a gas. the fluid phase (F). At intermediate ϕ_{col}, the system can phase separate in a gas phase with a low concentration and a phase with a liquid phase with high concentration, just as in gas-liquid phase separation. The only difference between the two phases is just concentration. Both phases coexist (G+L). At very high ϕ_{col}, crowding of the spheres results in crystallisation : the crystal phase (C). Both phases can coexist in part of the phase diagram (F + C)[62].

Fig. 2.15 shows that the exact phase diagram depends mainly on the inter-particle interaction and the size ratio of depletant over colloid size

$$q = \frac{R_G}{R_{coll}} \tag{2.26}$$

with R_{coll} the radius of the colloid. q is considered low for $q < 0.3$. Considering interaction between red blood cells, the size ratios are very low for Dex ($q_{DEX} \approx 0.002$) and low for *fd* ($q_{FD} \approx 0.11$).

For small q, non-equilibrium and metastable states dominate large parts of the phase diagram. Of particular interest is the region at higher ϕ_p where gelation can take place [62–64]. Percolation, related to gelation, appears to the right of the percolation line (red) in figure 2.15. For longe range depletants, the percolation line shifts to lower ϕ_{col}. The final phase diagram and different phases are strongly dependant on the nature and strength of the interaction and the kind of colloids. Different phases exist for different systems e.g. Gibbsite platelets [65], lysosomes [66],etc.

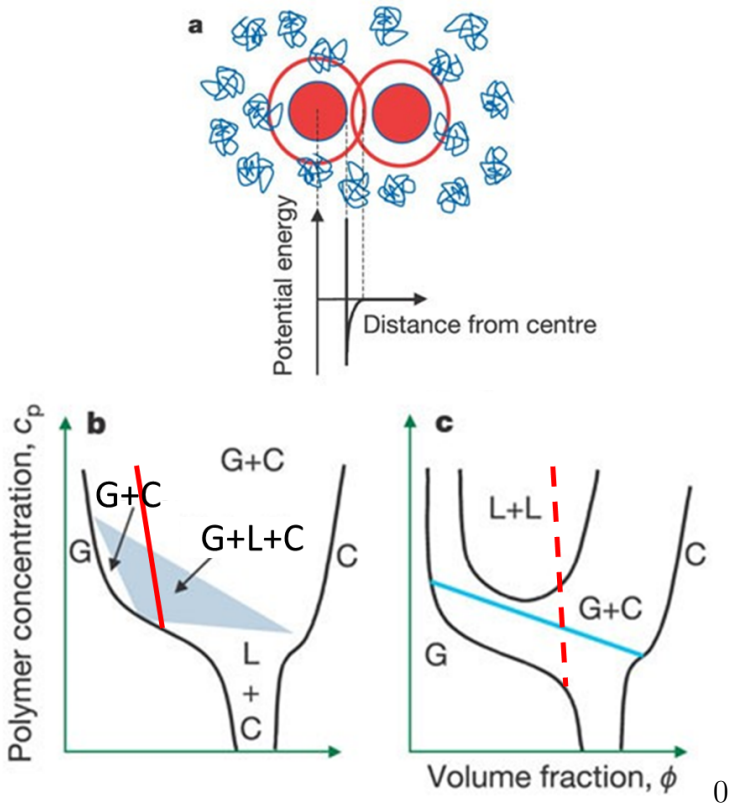

Figure 2.15: The depletion interaction between attractive spheres and it's phase diagrams, image from Anderson en Lekkerkerker [64] **(a)** Interaction potential with hard sphere core and depletion attraction tail **(b)** Phase diagram for large polymer depletion shows three phase region (shaded). Percolation line added in red (long range interaction = solid line) **(c)** Phase diagram for short polymer depletion, similar to some systems with proteins it shows two-phase coexistence and metastable liquid-liquid (L + L) region. Percolation line added in red (short range = dashed line)

2.6 Description of percolated networks

Aggregation between colloids can lead, under the right circumstances, to the formation of a colloidal gel. Gels are semi-solids with two or more components. Although gels consists of mainly liquid, they behave like a solid due to the presence of a network of colloidal particles. Initially, colloids flocculate into small aggregates that will then cluster together to form the larger gel networks [8, 9, 67]. The precursor to the completely gelled phase, is a percolated network. Percolation was introduced into theoretical physics by Flory [68] with regard to gel formation. The classical description of percolation is since used to describe phase transitions and other critical phenomena. Furthermore, from analysing the physical nature through percolation theory, interesting parameters are found to describe colloidal networks. Apart from physics, nowadays, percolation is an important field of study in mathematics and computer sciences alike [69].

In the classical model of percolation, a container is filled with particles that can form bonds (as in Fig. 2.16). After time, these particles will cluster together to form flocks and later larger superstructures. When there exists at least one such superstructure that spans the

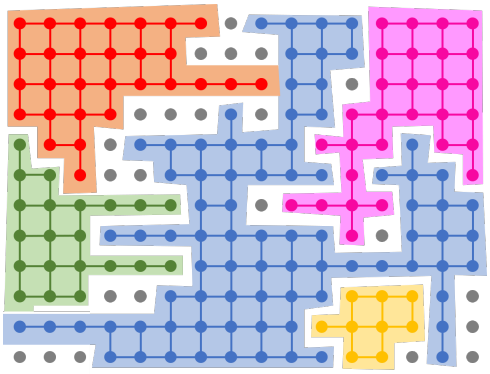

Figure 2.16: Particles connected by bonds form clusters. The blue cluster has percolated since it spans the entire matrix

entire container, percolation sets in. This space-spanning network is referred to as the *percolation network*. The interaction strength and the particles involved both influence the shape and behaviour of such percolated networks. Nowadays, depletion and bridging gels of spherical colloids are being developed and studied [8, 9, 70].

The formation of bridging gels is shown to closely follow the percolation line and results from purely kinetic phenomena [8], whereas depletion gels can form a percolated network that coarsens over time while not necessarily taking a kinetic pathway [9] determined by both kinetic and thermodynamic factors. Gels do not necessarely form when adding depletant, as was observed for example for mixtures of Gibbsite platelets and polymers which reach an arrested glass state as shown by Kleshchanok *et al.* [65].

RBCs are large colloidal particles that can aggregate due to depletion or bridging at the hand of neutral macromolecules and thus should form colloidal gels under the right conditions. These conditions are high enough volume fraction of cells ϕ_{RBC}, in order to have enough cells to span the entire considered space, and sufficient aggregation strength to maintain the aggregated network.

2.6.1 Characterisation of colloidal gels

There are several ways to identify gelation. We will discuss four techniques below: 2 rheological and 2 more physical.

Rheology of percolated networks

Rheology (literally *study of flow* in Greek) is the science that involves the investigation and characterisation of flowing matter. Besides the study of liquids and gasses, rheology mainly focuses on the flow of complex fluids and deformation of soft solids like gels. A material's rheological properties are paramount for it's applications in food technology, medicine, engineering and others.

In shear flow, a plate is shifted relative to another parallel plate (Fig. 2.17.a), causing a displacement. The fluid will react (and resist) this movement. This resistance to the displace-

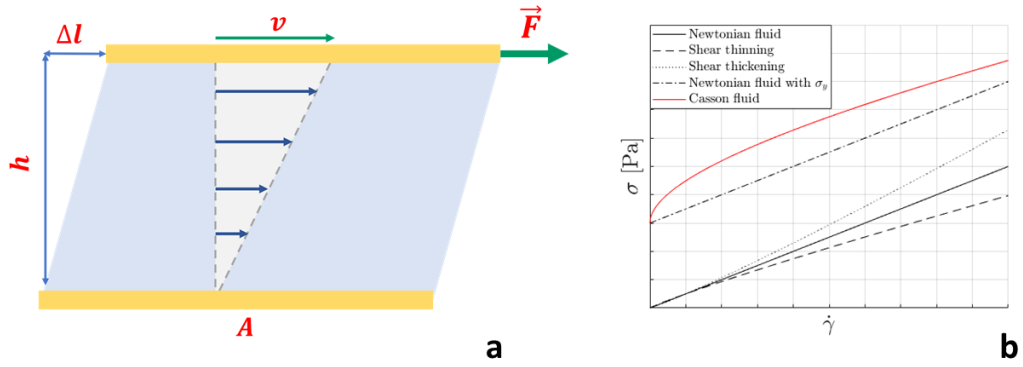

Figure 2.17: Key concepts in rheology **(a)** Shear force F causes a displacement Δl and flow of the fluid between two parallel plates separated by h **(b)** Shear stress σ dependency on shear rate $\dot{\gamma}$ for important Newtonian and Non-Newtonian fluids

ment is called viscosity η. Shear stress is given by

$$\sigma = \frac{F}{A} \tag{2.27}$$

where F is the shearing force and A is the area of the plates, as seen in Fig. 2.17.a. Shear strain is defined as the fraction of the displacement Δl compared to the separation of the plates h

$$\gamma = \frac{\Delta l}{h} \qquad \dot{\gamma} = \frac{v}{h} \tag{2.28}$$

where $\dot{\gamma}$ is the shear strain rate and v the velocity of the plate.

Viscous *Newtonian fluids* (solid black line Fig. 2.17.b) exhibit ideal flow where the shear stress is linearly proportional to the shear rate through the viscosity

$$\sigma = \eta \cdot \dot{\gamma} \tag{2.29}$$

The elastic behaviour of material, however, is treated as a *Hookean solid* where

$$\sigma = G \cdot \gamma \tag{2.30}$$

with G the shear modulus. Apart from these two ideal cases, real life materials (soft matter, real fluids,...) can be both viscous and elastic. Viscoelastic behaviour depends strongly on the time scales at which the shear is applied.
The first gel-characterisation approach, ***Dynamic Mechanical Analysis (DMA)***, reveals this behaviour. Here an oscillatory strain $\gamma = \gamma_0 \sin \omega t$ is applied to a material and the stress response is measured

$$\sigma(t) = \gamma_0 \left[G' \sin \omega t + G" \cos \omega t \right] \tag{2.31}$$

where G' is the shear storage modulus and $G"$ the shear loss modulus. Generally, a material is more elastic where $G' > G"$ and more viscous when $G' < G"$. In a frequency sweep, the moduli are measured at a fixed γ_0 for a wide range of frequencies ω. This characterises the behaviour of the material on different timescales. Gels exhibit the same behaviour at short and long timescales, and are thus in an arrested state. Both G' and $G"$ are independent of ω with $G' > G"$ signalling the elastic nature and strength of the gel (Fig. 2.18.a). The transition

from an aggregate suspension/liquid ($G' < G"$) to a gel can then be observed when G' crosses $G"$.

A second feature of gels and percolated networks is the presence of a ***yield stress*** σ_y, which allows such a material to show solid like behaviour at extremely small stresses and initiate flow above a certain threshold stress. Colloidal gels in steady state appear as a network of clusters that gets fragmented into smaller flocks when applying a stress $\sigma > \sigma_y$, and then starts flowing [71]. Yield stress fluids act as solids ($\eta \to \infty$) below the yield stress and flow beyond σ_y

$$\sigma = \begin{cases} \infty & \sigma \leq \sigma_y \\ \eta(\dot{\gamma}) & \sigma > \sigma_y \end{cases} \tag{2.32}$$

Fluids that exhibit Newtonian behaviour after σ_y are modelled with the *Bingham model*, first coined by Bingham [72].

$$\sigma = \sigma_y + \eta\dot{\gamma} \tag{2.33}$$

Shear flow can also influence the structure of the material. These non-Newtonian fluids can exhibit shear thickening or shear thinning behaviour (see Fig. 2.17.b). In this case, the fluid's viscosity is not independent of the shear rate $\eta(\dot{\gamma})$ and thus the stress response to shear rate will be more subtle. These fluids can be described with a *power-law model*

$$\sigma = \eta(\dot{\gamma}) \cdot \dot{\gamma} = k\dot{\gamma}^n \tag{2.34}$$

where k and n are constants. $n < 1$ is shear thinning while $n > 1$ is shear thickening. Further, shear thickening or shear thinning can also occur in yielding materials with the appropriate models to describe the flow. Whole blood is such a non-Newtonian fluid that displays a yield stress (Fig. 2.18.b) and shear thinning behaviour [1, 2, 73]. Before such a system can start to flow, the network needs to be broken into smaller aggregates, which explains σ_y. These aggregates will then be dismantled into individual RBCs at higher deformation rates $\dot{\gamma}$. Single RBCs more easily flow, thus demonstrating shear thinning.
At these very high shear rates, blood starts to behave Newtonian, while at low shear rates it was shown by Merrill *et al.* [1, 4] that blood behaviour is best described by the *Casson model* [1, 4, 74].

$$\sqrt{\sigma} = \sqrt{\sigma_y} + \sqrt{\eta\dot{\gamma}} \tag{2.35}$$

The science that explores rheological properties of blood and it's constituents is called haemorheology.

Physical percolation characterisation

Apart from rheology, the position of the individual colloids in a colloidal gel also reveal valuable information about the materials' composition and microstructure.
The ***radial distribution function*** $g(r)$ contains information on the structure of a sample. It is defined as

$$g(r) = \frac{1}{4\pi r^2 N}\frac{dN}{dr} \tag{2.36}$$

where r is the distance to the central particle, N the total amount of particles in the sample and dN the amount of particles in the shell $r + dr$. Particles in the gas phase are distributed isotropically , thus not showing peaks in $g(r)$ at characteristic length scales. More

ordered/structured phases (crystal, gel,...) show distinctive peaks. It is to be expected that RBCs in rouleaux, effectively one-dimensional crystals, show strong oscillations in $g(r)$ as the cells are spaced evenly from each other. $g(r)$ is often measured indirectly in diffraction experiments. However, since RBCs are large colloids that are optically visible, $g(r)$ can also directly be constructed from positions r_{CM} of cells in confocal images.
In colloidal gels, measuring $g(r)$ is particularly useful, given that it is directly linked to the fractal dimension d_f, a dimensionless parameter that expresses how densely a cluster is packed [75]. Therefor it is a useful way to compare percolated networks' structure.

This **direct detection of percolation** is the core of this work. As stated before, a percolated network is established as soon as the individual components of the network span the entirety of a predefined space. For systems of large colloids i.e. red blood cells, confocal imaging can visualise the network of aggregates in 3D. Graph analysis of these networks confirms the presence of percolation [70] or can be linked to the rheological behaviour of the network [76]. In figure 2.18.d a confocal image of RBCs ($\phi_{RBC} = 0.23 \quad [Dex] = 40\,\mathrm{mg/mL}$) was examined for percolation. If a paths exists between all sides of the images then the RBC network is said to span the entire image, and thus is percolated.

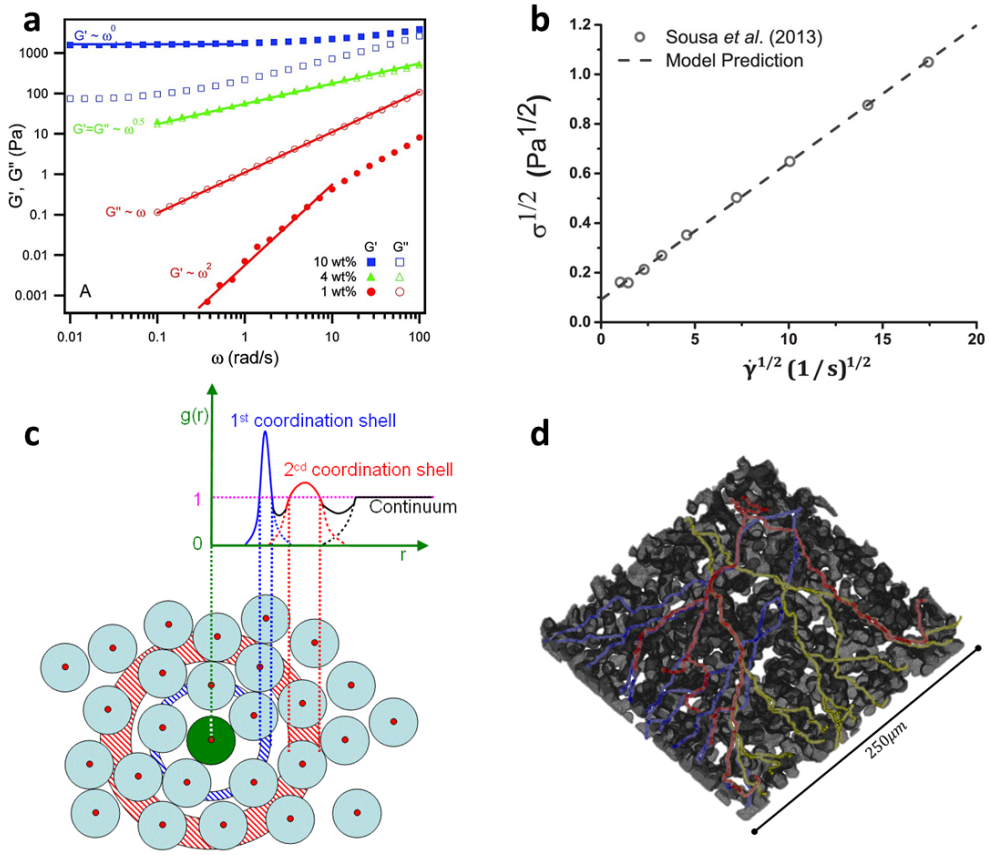

Figure 2.18: Characterisation and identification techniques for gels and percolated networks **(a)** Gel DMA frequency sweep on a SOS triblock-copolymer ion gel from He *et al.* [77]. Blue = gel, green = gel point, red = liquid **(b)** Whole blood shows non-zero yield stress σ_y for $Ht = 41.6\%$ and $T = 37°C$. Image from Apostolidis *et al.* [73] **(c)** Graphical representation of g(r). Image from [78] **(d)** Paths in X (blue), Y (yellow) and Z (red) direction show direct percolation in confocal images

2.7 Open questions

Although red blood cell aggregation [3, 6, 7, 14, 33, 46, 54, 79] and the yield stress in whole blood [1, 2, 73] have been extensively studied, a detailed study into colloidal gels [8, 9, 70] composed of RBCs is not yet attempted to our knowledge.

This is surprising as the flow and rheological behaviour of blood are strongly related to percolation, as was introduced above. Percolation of RBCs is not only of practical interest, but also of fundamental interest. The major differences with spherical colloids is of course their shape which results in the tendency to form rouleaux when aggregating. This shape anisotropy will therefore likely result in percolating structures that are markedly different from percolating spheres. The question here is when and how the rouleaux will branch to form a percolated network. However, there are practical issues that need to be dealt with when studying percolation of RBCs. First, the question is how aggregation is induced. Indeed, in whole blood there are many factors that play a role, so the challenge is to simplify the system to well controlled aggregation. Second, RBCs are more dense than the physiological buffer, so they will sediment, which can be solved by tuning the density of the buffer. Third, the structure needs to be imaged in 3D, and, finally, the imaged structure needs to be processed.

In this thesis, we attempt to establish colloidal RBC gels, prove the presence of percolation and investigate the difference in structures that are formed by introducing bridging or depletion agents. We present a direct way of detecting percolated structures from confocal images. Additionally we aim to present a phase diagram of RBC aggregation by addition of both Dextran and *fd*-virus. In this way, we wish to contribute to a better understanding of RBC aggregation at high ϕ_{RBC} and pave the way for future characterisation of colloidal RBC gels.

Chapter 3

Materials and methods

3.1 Red blood cells sample preparation

3.1.1 Phosphate Buffered Saline (PBS)

Red blood cells are to a high degree susceptible to changes in pH and tonicity of their environment. Tonicity is a measure indicating the osmotic pressure gradient between the surrounding medium and the interior of the RBCs. If the medium in a RBC solution is *hypertonic* or *hypotonic*, water will flow through the cell membrane, causing shrinking or swelling respectively. The ideal buffer for RBCs therefor has an equal amount of solutes as the cells: isonoticity. NaCl osmolarity in blood is known to be 290mOsm/l, additionally the blood is pH neutral with $pH = 7.40$.

In this work we use Sigma-Aldrich PBS-pellets (ref. P4417) to prepare an homogeneous PBS(1x) solution. The pellets are each dissolved in 200 ml of deionized Milli-Q water. The buffer contains 10mM phosphate, 2.7mM KCl and 137mM NaCl. The final solution has an osmolarity of 295-300 mOsm/l, as measured by freezing point technique. At temperature of $25°$, it has a pH of 7.40. PBS conditions resemble that of RBCs in human blood and is moreover often used as a buffer in biological research. Before sample preparation, the pH of the PBS-solution was verified with a pH meter and adjusted by adding some drops of NaOH or HCl.

3.1.2 PBS with Optiprep (PBS-OP)

Red blood cells in PBS tend to sediment quickly due to a mismatch in their densities, $\rho_{RBC} = 1.11\,\mathrm{g/\,mL}$ compared to $\rho_{PBS} = 1.01\,\mathrm{g/\,mL}$. For two solutions, the equations

$$\phi_1 + \phi_2 = 1 \qquad \rho_1 \cdot \phi_1 + \rho_2 \cdot \phi_2 = \rho_{RBC} \tag{3.1}$$

need to be satisfied to accomplish RBC density matching. ϕ_1 and ϕ_2 are the volume fractions required of both solutions. Elaborating this yields

$$\phi_1 = \frac{\rho_2 - \rho_{RBC}}{\rho_2 - \rho_1} \qquad \phi_2 = \frac{\rho_{RBC} - \rho_1}{\rho_2 - \rho_1} \tag{3.2}$$

Optiprep™(Sigma-Aldrich, ref. D1556) is a density gradient medium used regularly in biological research. It is a non-ionic, isosmotic, iodixanol-based medium non-toxic to cells. The solution,

60% iodixanol in water, has a density of $\rho_{OP} = 1.32\,\mathrm{g/mL}$, which makes it suiting for use in combination with PBS. In this work, we combine PBS with an already diluted PBS with Optiprep (PBS-OP) solution ($\rho_{PBS-OP} = 1.26\,\mathrm{g/mL}$). To density match RBCs (Eq. (3.2)), a solution of 60% PBS and 40% PBS-OP is prepared. The exact proportions depend on the density of RBCs, which can change subtly. Therefore, it is recommended to check the exact ratios for density matching every experimentation day by preparing a density matched solution and suspending some RBCs in it. After centrifuging, the RBCs should not sediment or float to the top if the medium is properly density matched.

3.1.3 CellMask™ membrane stain

CellMask™ plasma membrane stain (ThermoFischer Scientific) is a fluorescent dye used for imaging the plasma membrane, the cell's boundary, in fluorescence microscopy. The membrane stains are amphipathic molecules consisting of a lipophilic moiety for membrane loading and a negatively charged hydrophilic dye to anchor into the plasma membrane [80].

In this work, CellMask™ Deep Red plasma membrane stain (ref. C10046) was used to stain the RBCs' membrane. The deep red dye has fluorescence excitation and emission maxima at respectively 649 nm and 666 nm. This long wavelength dye is situated far into the red part (625-700 nm) of the visible spectrum. The choice for long wavelength dye comes from the importance of scans deep into the sample. This requires penetration of the sample up to 100 µm ideally. Longer wavelength light is known to better penetrate biological tissue and improve intensity because of reduced Rayleigh scatter ($I \sim 1/\lambda^4$).

3.1.4 RBC preparation

In this thesis, experiments are always performed with fresh human blood. The morning of an experiment, fresh human blood is collected by puncturing the fingertip with a sterile blood lancet and capturing it in an Ethylenediaminetetraacetic acid (EDTA) anticoagulation tube. The tubes used are ®MiniCollect EDTA coated (ref. 450474). Before puncturing, the finger is rinsed with ethanol to sterilise it. Typically, the daily amount of blood drawn ranges between 200-800 mg. These small amounts allow to draw small amounts of blood from the fingers' capillaries. After collection, the blood is diluted with 500 µL of isotonic solution of PBS (NaCl: 137 mM,KCl: 2.7 mM; pH = 7.4) and mixed to realise an homogeneous solution. PBS is a regularly used non-toxic buffer to wash cells [81] with a pH and osmolarity similar to that of the human body.The PBS-blood mixture is transferred to 1.5 mL ®Eppendorf vials for further RBC washing.

Washing red blood cells separates the RBCs from the plasma and buffy coat of WBCs.The main goal of this washing step, is to remove most of the natural proteins found in blood that, not only can influence experiments, over time they also contribute to echinocyte formation[82].

The employed procedure was based on [83].

1. Centrifuge whole blood with 500 µL PBS for 5 min at 500×G and room temperature
2. Remove the supernatant (PBS and plasma) and replace it with an equal amount of PBS. Vortex mix to homogenise the mixture
3. Centrifuge erythrocytes and PBS for 5 min at 500×G
4. Repeat step 2 and 3 so that the RBCs are washed three times overall and the supernatant is clear (See Fig. 2.2)
5. Remove the final supernatant and use the RBCs within 2-4 hours
6. Place RBCs in the right buffer to label them with fluorescent dye

3.1.5 Red blood cells dyeing with CellMask™ protocol

Confocal imaging requires stained RBCs. The cells' plasma membrane is labelled with CellMask™ dye.

1. Use 1.5 mL Eppendorf tubes
2. Bring washed erythrocytes in PBS to 10%Ht
3. While vortex mixing at low speed, add CellMask™ 1000X concentrated solution to create 1X working solution
   - Example. 200 µL PBS + 20 µL RBCs + 0.2 µL dye $\Longrightarrow$ 20 µL labelled RBCs
   - Labelled RBCs are always made in multiples of 20 µL
4. Vortex mix vigorously to homogenise the sample and distribute the dye evenly throughout the sample
5. Centrifuge the mixture for 10-15 min at 500×G and room temperature
6. Remove the supernatant (PBS and surplus dye) and cover the Eppendorf tube in aluminium foil to prevent photobleaching in full measure

3.1.6 Sample preparation RBC with macromolecules

The final samples for imaging with the confocal microscope consisted of fluorescently labelled RBCs with macromolecules (Dex or *fd*), density matched with PBS and PBS-OP and are prepared as follows:

1. Use 1.5 mL Eppendorf tubes
2. Determine the volume of macromolecules needed from $C_d \cdot V_T = C_{BULK} \cdot V_{macromolecules}$ where C is concentration (mg/ mL) and V is volume (mL).
3. Carefully pipette the right amounts of PBS, PBS-OP and Dex/*fd* to obtain a total solution volume $V_T = V_{PBS} + V_{PBS-OP} + V_{macromolecules}$
4. Add red blood cells so that $\phi_{RBC} = \frac{V_{RBC}}{V_T + V_{RBC}}$ and vortex mix the entire specimen

3.2 Rheology

3.2.1 MCR 702 twin-drive Rheometer

We use the MCR 702 twin-drive rotational rheometer by Anton Paar [84]. The device uses two twin "electronically commutated synchronous" (EC) motors to generate rotational shear between two co-axially mounted geometries. These geometries can be plate-plate (PP), cone-plate (CP) or a Couette cup, depending on the specimen specifics. Suspensions of RBCs have low viscosity (much like water) at small volume fraction of cells. With the twin-drive, accurate measurements were achieved by rotating the geometries in opposite directions with the twin motors (Fig. 3.1). Since our experiments involve only small amounts of red blood cells, we use small parallel plate geometries. These geometries require the smallest amount of sample to provide correct measurements.

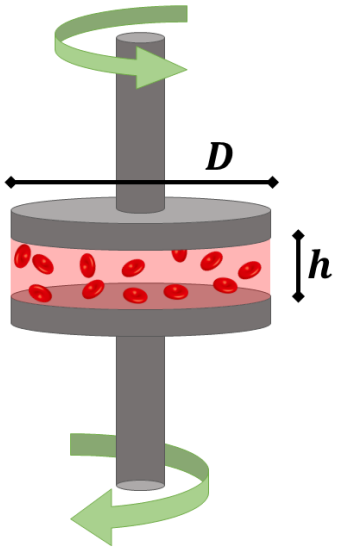

Figure 3.1: Schematic of parallel plate (PP) geometry, diameter D and gap h, with sample of RBCs. Twin drive system where geometries are rotated in opposite directions. Not to scale

3.3 Confocal microscopy

In this section, we go into the principles and breakthroughs that led to the development of confocal microscopy. Laser Scanning Confocal Microscopy (LSCM) is repeatedly used further on in this work and it was the most important tool for raw data collection. This section provides a description of the (dis)advantages of LSCM, resolution and different components of a confocal microscope.

3.3.1 Background and introduction

Fluorescence microscopy is a widely used imaging technique in biology, medical science and soft matter physics[85–87]. At present , fluorescence is a well understood principle that is used in multiple types of microscopes. Fluorescent molecules are excited by a source of excitation light to an higher energy level. These molecules can then relax back to a lower energy state by emission of a fluorescence photon with an energy $E = h \cdot \nu = \frac{hc}{\lambda}$. Scientists had been long aware of the phenomena of *fluorescence* and *phosphorescence* because of plant extracts that emitted different colours of light than the excitation source [88].The first real use of fluorescence in microscopic techniques only appeared at the beginning of the twentieth century. At first, measurements were focused on detecting the auto-fluorescent signal of different specimens. Only later, the discovery of specific fluorescent molecules, *fluorophores*, enabled scientists to label specific parts of a specimen.
In his 1942 work, Albert Coons presented one of the first important biological breakthroughs in fluorescent labelling[88, 89]. Through chemically labelling antibodies, he was able to investigate the presence and orientation of antigenic material in mammalian tissue. Coons' work on labelled antibodies [89, 90] proved a milestone in the popularisation of fluorescence microscopy, the rapid development of new fluorophore techniques and usages.

However, working with standard wide-field fluorescent microscopes limits the user in terms of resolution, Signal-to-Noise Ratio (SNR) and possibility to image 3D structures.

3.3.2 Laser Scanning Confocal Microscopy

The invention of the first confocal microscope by Marvin Minsky in 1955 [87, 91, 92] achieves improvement on all three limitations stated above. The main difference of a confocal- compared to other microscopes- is the presence of two pinholes. These serve to selectively illuminate the sample and block unwanted emission rays. The samples are illuminated one point at a time (point scanning). Minsky's transmission confocal consisted of a fixed illumination position with a stage that was moved in order to scan the sample. More recent development of different scanning mechanisms allows a reduction in scanning time for the microscope. The most frequently employed form of confocal is the Laser Scanning Confocal Microscope [92]. Here the excitation light from a laser is scanned across the sample, instead of moving the sample itself.

Modern day LSCMs are considerably modified compared to the original confocal by Minsky. The addition of a dichromatic mirror (Fig. 3.2) enables epi-illumination of the sample. Since the sample now does not need to be placed between the lenses, it is especially easier to handle biological samples. A dichromatic mirror is designed to reflect short wavelength light and let longer wavelength photons pass. As the excitation light is of shorter wavelength, choosing the

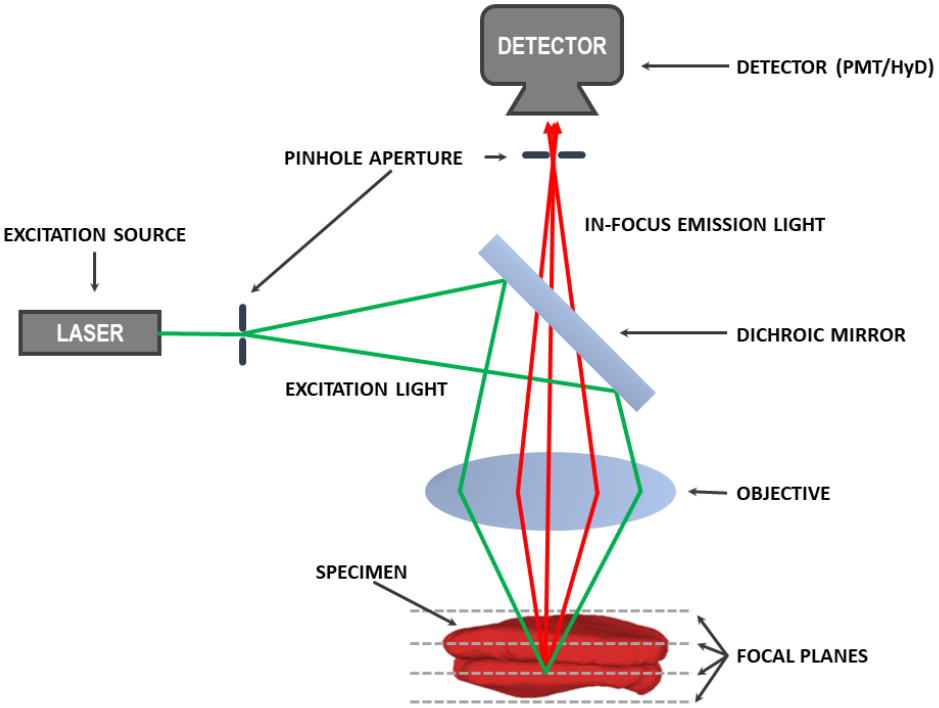

Figure 3.2: Schematic diagram of the excitation light cone and in-focus excitation light in a LSCM

right dichroic allows longer wavelength emission to pass while blocking the excitation light. Lasers are most often used in confocal microscopes, since they allow excitation at one specific wavelength for one specific fluorophore. Sometimes, however, multiple laser channels can be combined to visualise multiple fluorophores at once. This does also require a detector for each type of fluorophore. Light-Emitting-Diodes (LEDs) are also becoming an interesting alternative to the lasers, since they produce less heat, are very intense and often cheaper.

Laser light is focused on a first pinhole that creates a point light source (see green lines Fig. 3.2). After being reflected by the dichroic mirror, the excitation light is focused onto the sample by the lenses inside the objective. Fluorophores inside the beam-path are excited and will isotropically emit the longer wavelength fluorescent light (red lines Fig. 3.2). By introducing a second pinhole, only light from the focal spot will reach a detector. The blocking of this out-of-focus light ensures the detection of a single focal point in the sample, enabling the confocal principle. The detector is typically a Photomultiplier Tube (PMT) or Hybrid pixel Detector (HyD). HyD detectors combine the vacuum tube of a PMT with the high gain in a semiconductor Avalanche Photodiode (APD) and were developed by Leica for use in their confocal microscopes [93].

In order to image a complete 2D image, the focal spot is moved across the sample in a line pattern. Minsky achieved this by moving the stage, however, in a LSCM two scanning mirrors (x and y direction) allow line scanning. Line scanning has the benefit of not physically moving the specimen, which can result in distortion and resolution loss. Finally, a 3D stack of images is collected by moving the objective in Z-direction and capture a 2D image at every Z-position (Fig. 3.3.a). As advantageous as 3D scanning is, a disadvantage is the long acquisition times needed to scan a whole specimen (Fig. 3.3.b) point by point [94].

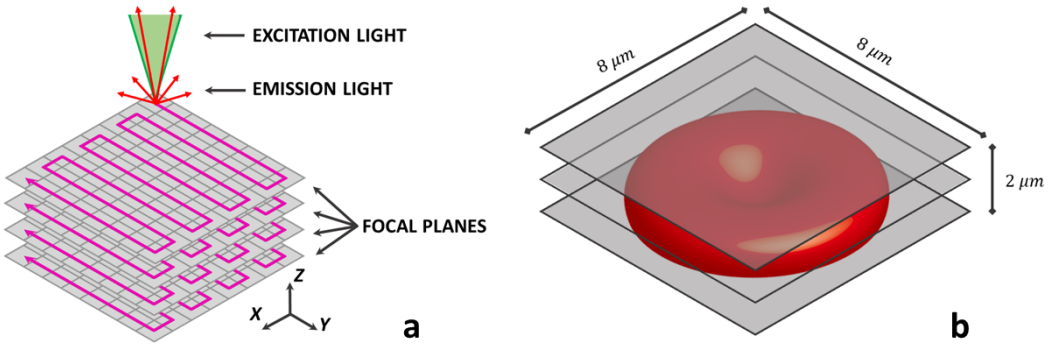

Figure 3.3: Obtaining images of focal planes at different depths allow for reconstruction of 3D objects **(a)** Schematic of LSCM scanning direction **(b)** 3D scan of RBC

Resolution is determined by the objecctive's numerical aperture NA, a dimensionless number. NA of a microscope objective depends on both the refractive index of the medium n and maximal half-angle θ of the cone of emission light that can enter the objective.

$$NA = n \cdot \sin\theta \tag{3.3}$$

Some commonly found types of objectives are dry objectives ($n_{air} = 1.00$), oil immersion objectives ($n = 1.51$) or water objectives ($n = 1.33$).
The numerical aperture is directly linked to the resolving power and resolution of the microscope system. Whereas resolving power is the capacity of an instrument to distinguish two points which are close together, the resolution R is the minimal distance between two individual point sources. De facto it's the smallest distance at which two separate light sources will appear as two separate points in an image. For a microscope where the objective and condenser lens are one, lateral resolution (in *xy*-plane) is defined as

$$R_{XY} = \frac{0.61 \cdot \lambda}{NA} \tag{3.4}$$

where λ is the wavelength of the emitted light. A confocal has the added benefit of a narrower Point Spread Function (PSF) than a typical widefield fluorescence microscope, due to the presence of the pinholes. This further increases lateral resolution with a factor $\sqrt{2}$

$$R_{confocal,XY} = \frac{0.43 \cdot \lambda}{NA} \tag{3.5}$$

Finally the axial resolution (along Z-direction), defined as

$$R_Z = \frac{n \cdot \lambda}{NA^2}, \tag{3.6}$$

is also improved in a confocal microscope [95]. This results in

$$R_{confocal,Z} = \frac{n \cdot \lambda}{(n+1)NA^2} \tag{3.7}$$

In conclusion, confocal microscopy improves resolution and manages to construct 3D images by means of point-scanning the preferred specimen. The relevant specimen ought to be

auto-fluorescent or fluorescently labelled in order to visualise.
To gather three-dimensional data, the LSCM captures images at different focal planes. In between, the objective is moved stepwise in Z-direction as can be seen in Figure 3.4b. Here an erythrocyte is confocally visualised at different depths. The fluorescence is achieved by labelling the cell's membrane. Some examples of the usage of 3D confocal stacks are cross sections (Fig. 3.4a) or reconstructed meshed objects (Fig. 3.4c).

The final samples are density matched with PBS and PBS-OP and loaded into ®Ibidi μ-slide VI 0.1 (cat.No 80666) channels (Fig. 5.1a) for imaging. Most confocal images in this work are produced by a Leica TCS SP8 laser scanning confocal with a 63x glycerol objective (water-glycerol mixture $n = 1.46$ and $NA = 1.3$)[96]. The membrane dye has an emission maximum at $666\,\mathrm{nm}$, thus resulting in a lateral and axial resolution of respectively $R_{XY} = 220\,\mathrm{nm}$ and $R_Z = 234\,\mathrm{nm}$. Some images were acquired using the VT-Hawk confocal by VisiTech international (Sunderland, UK) combined with an Olympus (Shinjuku, Tokyo, Japan) IX71 microscope. This microscope has a objectives of different magnification (20X,60X,100X,...), all with oil $n = 1.51$ and $NA = 0.85$ (for the 20X). The resulting lateral and axial resolutions are $R_{XY} = 478\,\mathrm{nm}$ and $R_Z = 555\,\mathrm{nm}$.

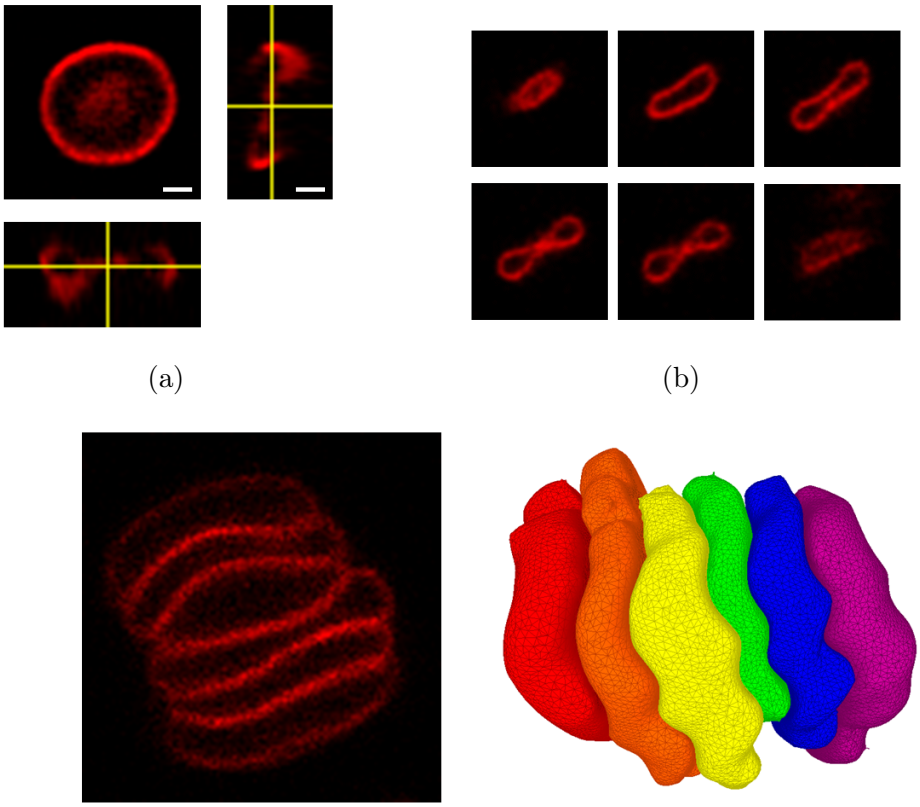

(a) (b)

(c)

Figure 3.4: **(a)** Confocal image of discocyte RBC and it's reconstructed cross section. Scale bar is $2\,\mu\mathrm{m}$ **(b)** Sequence of RBC confocal images at different Z depths. Confocal scans consist of a 3D stack of images. **(c)** Confocal Z-stacks are used to recreate 3D objects e.g. a mesh reconstruction of a rouleaux of RBCs image (see section 3.4.3)

3.4 Image analysis

In the following section, we elaborate on the different steps taken in image treatment. We explain what filters were applied to raw confocal images and the different software used to analyse images. For most of this work, we use the open source image processing software ImageJ with the FIJI platform [97]. Additionally, the carving toolbox in the software program ilastik [98] was also employed. Both programs are well established tools in biological image analysis, lending itself perfectly to red blood cell samples. The flowchart (Fig. 3.14) in section 3.6 indicates where the different image analysis techniques were used in this work.

3.4.1 Confocal images and raw data

The raw images, obtained in confocal microscopy, are 3D *.tif* stacks of 2D cross sections of the sample (as seen in figure 3.3 and 3.4.b). However, it is more straightforward to imagine the images as a rectangular prism divided into separate voxels (data points in 3D grid) with a specific width w, length l and height h. The voxel value corresponds to the intensity of light measured by the detector at that position. Position of each voxel is determined by it's 3D coordinate (x,y,z)

$$x = n \cdot w \qquad y = m \cdot l \qquad z = p \cdot h$$

where n, m, p are the voxel identifiers. The width and height of the voxel correspond to the pixel (data point in 2D grid) size of the image, which depended on the confocal settings, mainly the step size of the scan.The height h corresponds to the inter-planar distance (Z-spacing) chosen i.e. the physical height difference between two subsequent Z-scans. In Figure 3.5 such a *.tif* stack is shown. l and w are the same and on the order of tens to a few hundred nm, while h is $334\,\mathrm{nm}$ or slightly less. The 2D image size was 512 X 512 or 1024 X 1024 (pixels X pixels), while the 3D image size depends on the Z-spacing and the total scanned depth.

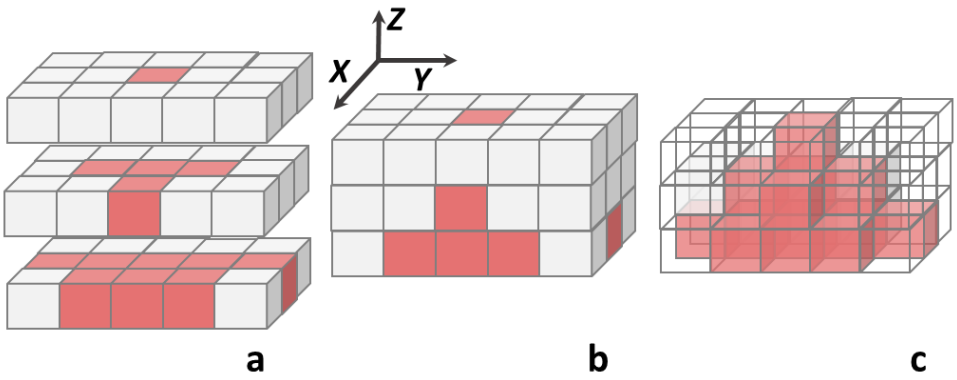

Figure 3.5: **(a)** Cross-sections as taken by confocal microscope **(b)** 3D representation of a *.tif* stack **(c)** The original 3D object is visible

3.4.2 Image processing

Having established the fundamental properties of the confocal images, images will need to be treated in order to improve their quality. Different filters are applied and can be used to smooth the raw images, remove noise, remove the background, etc. Most of the filters rely on

a convolution with a specific kernel matrix. Depending on what we want to do with an image, different filters or a combination of them will be applied. *Note that although we present here the 2D filters, 3D filters are similar and are often used on the 3D stacks.*

Gaussian blur

Gaussian blurring (Fig. 3.6.b) is a convolution with a 2 or 3 dimensional Gaussian kernel. The Gaussian distribution in 2D follows

$$G(x,y) = \frac{1}{2\pi\sigma^2} e^{-\frac{x^2+y^2}{2\sigma^2}} \tag{3.8}$$

where (x, y) are the positions of the kernel and σ is the standard deviation of the distribution, also referred to as the radius of the filter. A Gaussian filter is used to smooth an image, reducing detail and noise.

$$\mathbf{G} = \begin{bmatrix} 0.059 & 0.097 & 0.059 \\ 0.097 & 0.159 & 0.097 \\ 0.059 & 0.097 & 0.059 \end{bmatrix}$$

A Gaussian (3×3) kernel with $\sigma = 1$ is calculated in matrix **G** where $(x = 0, y = 0)$ corresponds to the centre of the matrix.

Unsharp masking

Unsharp Masking (USM) (Fig. 3.6.d) is a sharpening filter that aims to convert a blurred image into a mask of the original sharp equivalent. In effect, it enhances edges all the while subtracting a blurred copy of the image. Mathematically this can be seen as subtracting a Gaussian version of an image from the original image

$$USM(x,y) = \delta(x,y) - M \cdot G(x,y) \tag{3.9}$$

where M is the mask weight. Increased mask weighted, enhances edges. Furthermore USM also depends on the Gaussian standard deviation σ.

$$\mathbf{USM} = \begin{bmatrix} -0.059 & -0.097 & -0.059 \\ -0.097 & 0.841 & -0.097 \\ -0.059 & -0.097 & -0.059 \end{bmatrix}$$

A USM (3×3) kernel with $\sigma = 1$ and $M = 1$ is calculated in matrix **USM**.

Mean and median filter

Another, often used filter to smooth images, is the mean filter (Fig. 3.6.c). The implementation is extremely simple as it replaces a pixel's value by the average of itself and it's neighbours.

$$\mathbf{M} = \frac{1}{9} \cdot \begin{bmatrix} 1 & 1 & 1 \\ 1 & 1 & 1 \\ 1 & 1 & 1 \end{bmatrix} = \begin{bmatrix} 0.111 & 0.111 & 0.111 \\ 0.111 & 0.111 & 0.111 \\ 0.111 & 0.111 & 0.111 \end{bmatrix}$$

A mean (3×3) kernel is calculated in matrix **M**. The median filter results in very similar smoothing behaviour but it replaces the pixel value by the median of itself and it's neighbours.

Subtract Background

Background subtraction (Fig. 3.6.e) in FIJI is achieved with the rolling ball algorithm. This was first developed by Sternberg [99] and imagines (in 2D) that a rolling ball rolls along the intensity landscape of an image. Very bright spots are then intense high peaks where the ball will not roll to. The ball will roll along the smoothly varying landscape (background), depending on the radius of the ball. The region where the ball can migrate to, the background, will be removed from the original image. The final image then has increased contrast between the new background and the bright intensity peaks. The radius of the ball must be chosen to be larger than the radius of the smallest peak that you consider foreground. Background subtraction can also be adapted to 3D images.

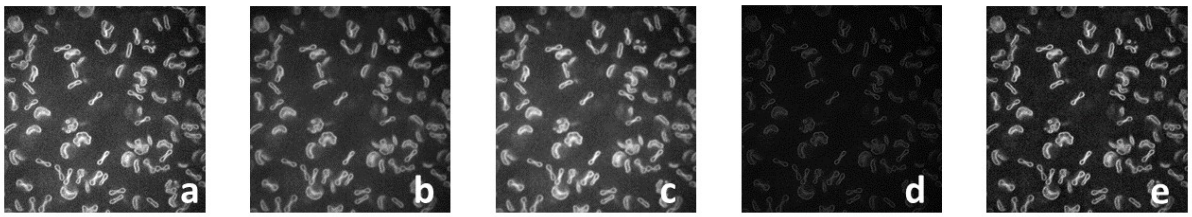

Figure 3.6: **(a)** Original image **(b)** Gaussian blurring $\sigma = 1$ **(c)** Mean filter **(d)** Unsharp masking $\sigma = 1$, $M = 1$ **(e)** Rolling ball background subtraction with $r_{ball} = 20\ pixels$

3.4.3 Ilastik individual cell segmentation

Accurate detection of individual RBCs is necessary for the determination of the centres of mass r_{CM} of these cells and the construction of a three-dimensional mesh of said cells. Nowadays, efficient bio-image examination is guaranteed by the rise of machine-learning-based image analysis programs. One such software program, ilastik, provides experimentalists with an environment for semi-automatic segmentation of objects based on their boundary information [98].

In this *carving-workflow*, users indicate manually the different objects they want to segment with brush strokes on 2D image slices of the three-dimensional image stack (Fig. 3.7.a). In brief, the program starts by finding approximate object boundaries by running an edge detector over all pixels of the image volume, which is later segmented into supervoxels by a watershed algorithm. The user-defined brush strokes provide the seeds for this watershedding algorithm. A more elaborate description of the ilastik *carving* workflow is not presented, since it wasn't used that often in the bulk of our research.

In this work, ilastik segmentation is predominately used for the identification of individual red blood cells. The user is required to, one cell at a time, classify that RBC as a cell with a brushstroke, while labelling all other RBCs and background as background. The software then segments this cell and stores it's 3D shape as a meshed object. To this extent, we can segment larger aggregates (like rouleaux) into it's individual constituents, as seen in figure 3.4.c. After identifying all individual cells, the meshes can be extracted and used to render the 3D structures (Fig. 3.7.b). This meshed objects can then be used to calculate the volume of the objects, r_{CM}, bending energies of the membrane, etc. By trial and error, it was found that segmentation in ilastik was more correct when the input confocal images were first

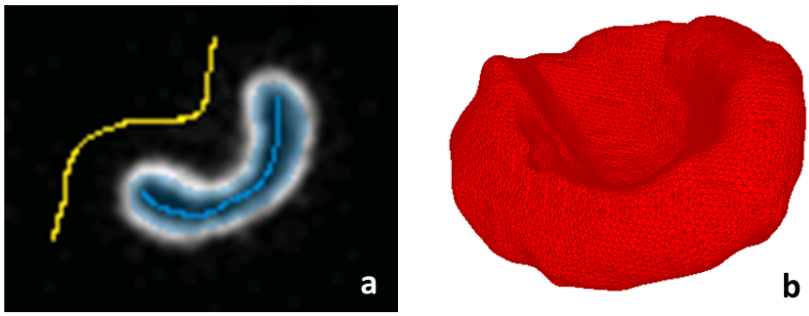

Figure 3.7: Ilastik environment: **(a)** brushstrokes (user input) to label individual cells (blue) and background (yellow) **(b)** output meshes used to generate 3D reconstruction of cells. 3D reconstruction in software program Meshlab [100]

pre-processed. This pre-processing involves a background subtraction in combination with a smoothing filter (Gaussian or median), possibly supplemented with unsharp masking.
Disadvantageous to this method, is the necessity of high quality, strongly magnified images of the RBCs and the laborious process of having to label each individual cell that needs to be segmented. Therefore, ilastik will be mainly used when accurate information about a small amount of cells is desired. In the next section, however, we present Trainable Weka Segmentation that can more easily identify same class objects by itself, without requiring manual input for each of those objects, but is not able to create accurate meshed objects.

3.4.4 Trainable Weka segmentation

Crucial to our analysis was the ability to create binary images of red blood cells and RBC networks. This requires the RBC membrane and cytosol to be differentiated as the same objects in comparison to the sample background. In order to do so, the FIJI plugin *Trainable Weka Segmentation (TWS)* is utilised [101]. This plugin employs machine learning to achieve image segmentation, where different structures are labelled.

TWS operates with the help of the open source machine learning software Waikato Environment for Knowledge Analysis (WEKA). As all machine learning programs, TWS uses user input to improve it's segmentation ability. The user is asked to identify different classes of object in the image, after which TWS aims to label all objects of a same class identically. The user can then adjust the classifier in order to train the software further. In comparison to ilastik, TWS does not demand user input for each individual object.
In this project following steps (also Fig. 3.8) are taken when using TWS

1. Upload filtered (gaussian and mean) RBC confocal *.tif* stack to TWS 3D
2. Define two classes of pixels via drawing lines over pixels of different classes by hand
   - Red blood cell class: voxels of RBC membrane and RBC cytosol
   - Background class
3. Start Trainable Weka Segmentation

- TWS creates a feature stack for calculations (only the first time)
- Identifying user input
- Pixel classification on the basis of user input

4. Return of a classified image
5. Possibility to further train the machine by repeating steps 2-4
6. Export classified image as a binary *.tif* stack with two values RBC (pixel value = 1) and Background (pixel value = 0) or vice versa

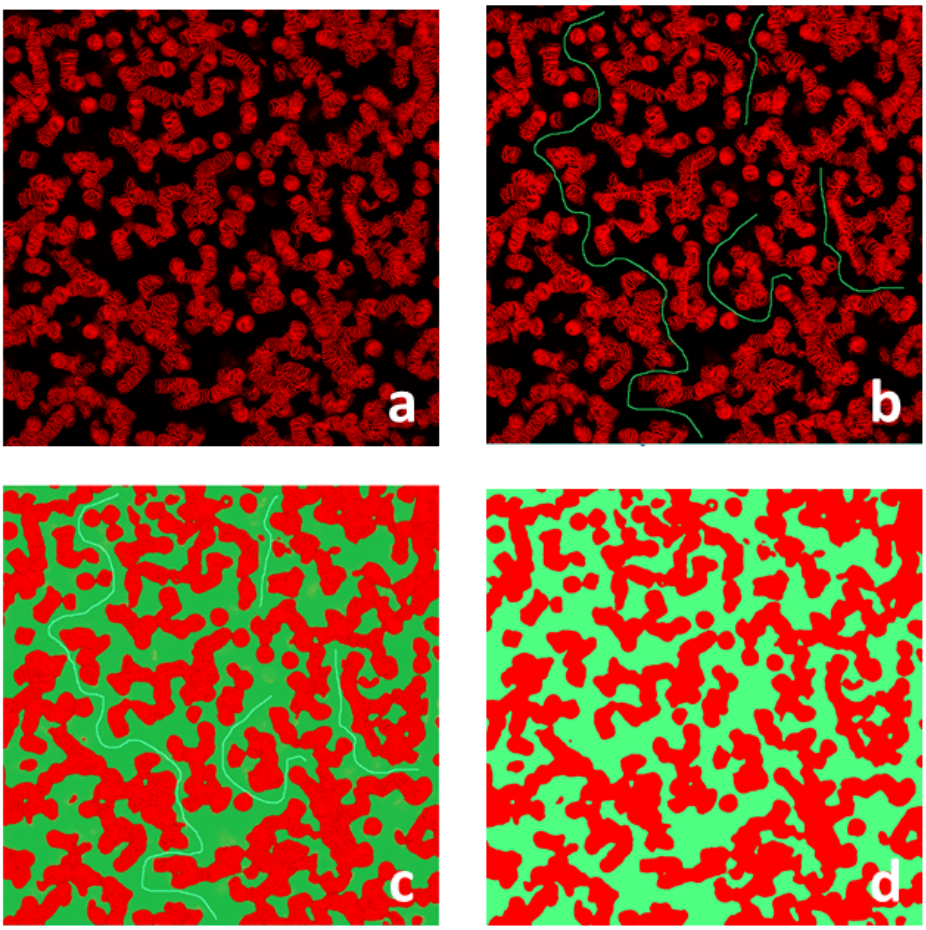

Figure 3.8: **(a)** original confocal image **(b)** Manual classification of different objects as in step 2 **(c)** Classification by TWS as in step 3-4 **(d)** Classified image as in step 6

Since WEKA is a pixel classifier, the time dependence of the software relies heavily upon the number of voxels per image. The most intensive part of the classifier is the creation of a feature stack for calculations (first time step 3). The actual machine learning and user input (steps 2-4) happens fairly quick.

Image analysis with TWS was done on a $32GB$ RAM desktop to images with dimensions of (512×512) pixels in XY and a depth of (100-300) voxels in Z.

3.5 Data analysis and algorithms

In this section, the output images of TWS segmentation are further analysed to gain physical insight into the aggregation of red blood cells.

3.5.1 Volume fraction control

Given that flaws in the preparation of the sample can easily occur, such as inaccurate measuring, sedimentation of cells, bad data acquisition, etc., we check our confocal images for the right ϕ_{RBC} before analysing them further. This is trivial when provided with classified *.tif* stacks with RBC (pixel value = 1) and background (pixel value = 0) from the Trainable Weka Segmentation. The calculated volume fraction of RBCs is the number of RBC voxels N_{vox} in comparison by the total number of voxels

$$\phi_{RBC,calc} = \frac{N_{vox,RBC}}{N_{vox,Tot}} \tag{3.10}$$

where we consider the experimental ϕ_{RBC} correct when it is within 0.05 of the calculated volume fraction. As seen in figure 3.14, volume fraction control is a crucial step before initiating a percolation path search. When the calculated ϕ_{RBC} is too divergent, segmentation with TWS can be repeated. If still offbeat, the corresponding image is not used for the percolation algorithm.

3.5.2 Percolation algorithm

Confocal image stacks, allow to visually and direct identify percolation networks in certain specimens. Percolation requires the arrangement of a 3D network that spans the entire space. In case of a confocal image stack, the RBC network should span the entirety of the image stack in all three directions X,Y and Z. Here, we explain how this requirement was examined and discuss why certain choices of analysis were taken.
The basic idea is to identify the useful RBC voxels in an image, transform them into a three dimensional graph and apply a path searching algorithm to find paths between the different faces of the image. This results in 6 steps to complete percolation analysis:

1. Image pre-processing
2. Start and end plane identification
3. Search node determination
4. Shell creation
5. Graph analysis and path search
6. Path construction and image creation

Image pre-processing

Percolation analysis requires binary image stacks that consist of background voxels and network voxels where RBCs are. As seen in the flowchart (Fig. 3.14), these images are then pre-processed by applying a median filter (Fig. 3.10.b). The median filter will smooth the image while the voxel values remain 0 or 1 (section 3.4.2). Image pre-processing happens on the entire 3D image stack.

Start and end plane identification

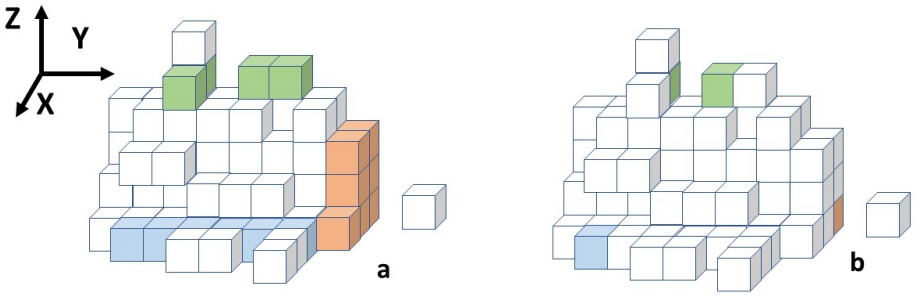

Figure 3.9: Principle of start (or end) plane identification. The cubes represent non-zero RBC voxels. **(a)** When it is required that the start planes contain more than 3 non-background voxels, the coloured cubes represent the start planes in X (blue), Y (red), Z (green) direction. **(b)** All voxels that connect to each other in a start (or end) plane, are represented by 1 *search pixel/node*

The 3D binary image stack consists of 2D planes, where the challenge is to find a point in the starting plane which is connected via a path to a point in the end plane. Since the boundaries of the images (mainly in Z-direction) often contain very little RBC voxels, those planes are not necessarily used as start (or end) plane. Here, a method is described to find the planes, that are used to search paths between, for the Z-direction. Identical operations are applied for the other principal directions as well.

The amount of non-background pixels in each plane of the 3D stack is counted, starting at the initial boundary planes of the image. If the initial plane contains less non-background pixels than a certain threshold (e.g. 1 percent of the pixels per image) then this plane is disregarded and the subsequent plane is considered (Fig. 3.9). The first plane that fulfils the requirement is considered as the *start plane*. For the *end plane*, a similar approach is followed, starting in the opposite direction.

Search node determination

Paths can be studied between all RBC voxels of the start and end planes. However, this is time consuming and computationally excessive as most voxels in both these planes connect to each other and are therefore by force belonging to one path. It becomes critical to reduce the number of pixels in the 2D start (and end) planes to a minimum. This minimal number of pixels are referred to as *search pixels*. Later on, their three-dimensional coordinates are used in

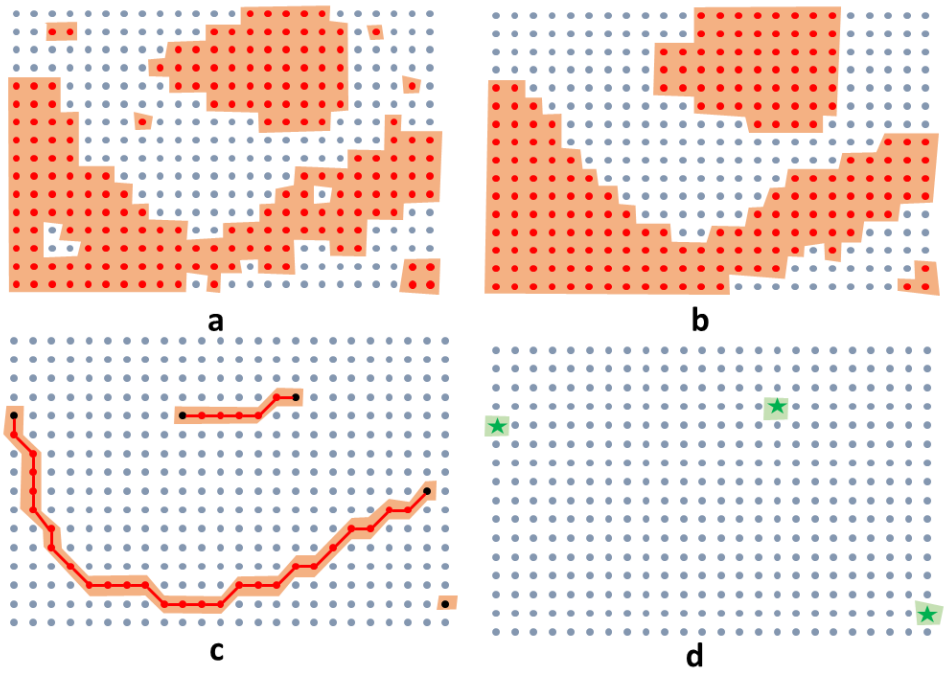

Figure 3.10: Different steps to identify search nodes in a 2D image: **(a)** Raw binary image needs filtering to remove noise; **(b)** Median filter removes isolated regions while retaining the binary nature of the image; **(c)**After skeletonisation, nodes with one or zero edges (black) are checked for internal paths; **(d)** Search nodes/pixels (green stars) are the minimal number of nodes that connect all nodes in that 2D plane

the path searching graph, and they are indicated as *search nodes*. Each search pixel represents all the pixels in one plane which are connected to that pixel in the same 2D plane. Note that search pixels can still connect to each other in the three-dimensional network, but that is not checked. Next we describe how search pixels are determined in a two-dimensional image.

Median filtering was required (as described in section 3.5.2) since it guarantees the removal of isolated pixels (Fig. 3.10.b) that would have been identified as search pixels but are not part of the network, but rather artefacts of TWS. Next, a topological skeleton of the selected plane is composed, which emphasises the geometrical and topological properties of the RBC network shape. Skelitonisation (Fig. 3.10.c) returns a reduced amount of pixels that retain the connectivity of the shape. Thereafter, these skeletonised pixels are appended to a two-dimensional graph. Skeletonisation is a build-in python (skimage package) command. The skeletonised pixels are represented by *nodes* (as is jargon) in a graph. Nodes are connected by *edges*. In our examples, two RBC nodes (red dots) are connected by an edge (red line) when their corresponding pixels are neighbours horizontally, vertically or diagonally (Fig. 3.10.c). The graph structure allows easy network and path analysis.

The *degree* of a node is defined as the number of edges that connect to that node, i.e. how many neighbours a pixel has. Nodes with a degree of zero are immediately classified as *search nodes* (Fig. 3.10.c bottom right), as they do not connect to any other pixels in that plane. Nodes with degree one are potential search nodes but are still connected to other nodes, and thus to other potential search nodes of degree 1, as seen in figure 3.10.c. The

potential search nodes are reduced by checking for paths between themselves in the 2D graph. In a graph structure this is a standard command in python (Networkx package). When two potential search nodes turn out connected, the node corresponding to the pixel furthest from the origin of the image is disregarded. This is important to keep in mind since percolation paths therefore tend to be situated mainly at the origin of an image. In reality, this is because the search nodes (which still connect to many other pixels in a plane) are located primarily at the origin (Fig. 3.13). The final nodes that do not connect to any other nodes, are the final *search nodes* (Figs. 3.10.d and 3.9.b) and their corresponding (x,y,z) coordinates are stored for path searching in 3D. Table 3.1, indicates the amount of pixels in figure 3.10 that fit the criteria along the reduction process.

	Median filter	Skeletonisation	degree ≤ 1	Search nodes
Pixels	193	36	5	3

Table 3.1: Number of pixels that fit the criteria in image 3.10

Shell creation

Graph construction allows for the examination of percolation paths through Dijkstra's shortest paths algorithm. Since we are dealing with large images ($512\times512\times150$ voxels), the complexity and thus speed of the algorithm have to be taken into account.
The most time consuming steps are the construction of the graph and Dijkstra's shortest paths algorithm. For graph construction, each voxel has to be added to a graph and checked for neighbours (to include edges). This step thus has a time complexity proportional to V, the number of RBC voxels (or nodes in the graph).
For the Dijkstra's shortest path algorithm, the worst case scenario for a path search between two nodes is proportional to $E + V \log V$ [102], where E is the number of edges in the graph. Considering all this, it becomes essential to reduce the total number of nodes (and attaching edges) in the graph.

Before graph construction, we therefore reduce the original binary image to a shell of it's initial shape (Fig. 3.11). In the three-dimensional stack, all voxels that are part of the volume of the RBCs, rather than the surface, will be re-labelled as background. In this work, we choose to find paths along the surface rather than through RBC centres. However, it is perfectly possible to do the opposite and the same results should show. The choice was based on the ease of implementation.
Implementation for *shell creation* is achieved through convolving the classified binary image stack with a 3D *Shell kernel* $\mathbf{S}$ that counts the amount of nearest neighbour (not diagonal) RBC voxels.

$$\mathbf{S} = \left[\begin{bmatrix} 0 & 0 & 0 \\ 0 & 1 & 0 \\ 0 & 0 & 0 \end{bmatrix}, \begin{bmatrix} 0 & 1 & 0 \\ 1 & 0 & 1 \\ 0 & 1 & 0 \end{bmatrix}, \begin{bmatrix} 0 & 0 & 0 \\ 0 & 1 & 0 \\ 0 & 0 & 0 \end{bmatrix} \right] \tag{3.11}$$

The image that results from this convolution has values between 0 and 6, that correspond to the number of neighbours each voxel has in 3D. Value 0 means that that voxel has no nearest neighbours and thus should not be part of a smooth RBC surface. On the other hand, value 6 means that that voxel is surrounded by other RBC voxels. A path that would go through

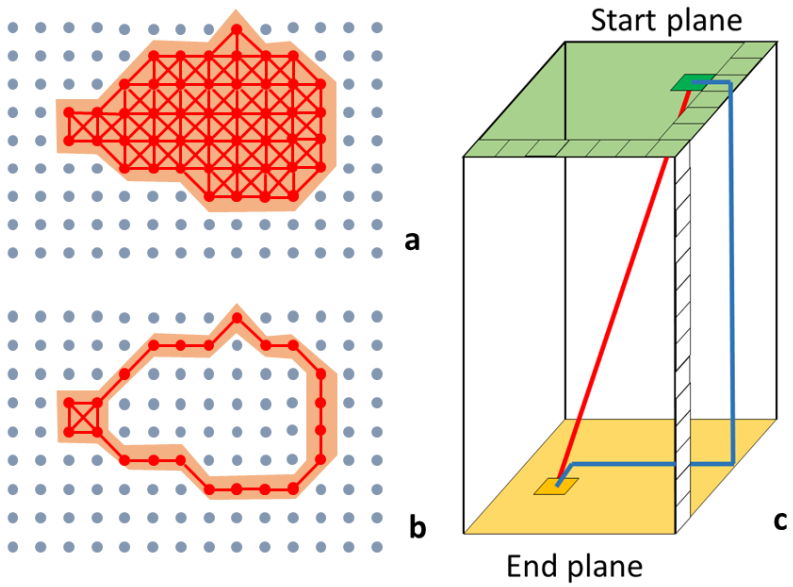

Figure 3.11: Generating a shell (here in 2D, for easier visualisation) of the image reduces the number of nodes and edges dramatically without losing nodes that describe the shape **(a)** Fully connected image **(b)** Connected shell (in 2D) **(c)** Multiple RBC voxels (partly indicated by the lattice) make up this cuboid object. Paths between pixels in the start and end plane in a fully connected image (red) go through the object's volume. Paths in the shell image (blue) follow the cuboid sides as the inside voxels are relabelled as background

this voxel, can also go through those neighbours, rending the according voxel unnecessary (similarity 2D in Fig. 3.11).

After shell construction on the entire 3D binary image, the start and end planes (in X,Y,Z) are inserted entirely back into the shell-image, since the search nodes are not necessarily located on the surface of the RBCs. They are definitely part of the start and end planes, hence they are also present in the shell-image after insertion of the start and end planes.

Graph analysis and path search

As mentioned in section 3.5.2, path searching is extremely uncomplicated in graph structures. Thus in order to detect percolation in the 3D network, we will search for paths in a 3D graph. The nodes in this graph correspond to the RBC voxels in the binary image and are labelled with their matching coordinates (x, y, z). Nodes are connected by edges when their corresponding voxels are neighbouring RBC voxels in the image stack.

After the establishment of the graph, paths are detected between the search nodes of the start and end plane in Z-direction (similarly for the X- and Y-direction). The path search between two nodes uses *Dijkstra's shortest path* algorithm [102]. The nodes that are found the be part of the shortest path between two *search nodes*, are then selected (Fig. 3.11.c). The matching voxels will then be assigned new voxel-values in a copy of the original binary image stack. Voxels of paths in Z-direction get value 2 while voxels of paths in X and Y get,

respectively, values 4 and 6. The reason why is discussed in the following section.

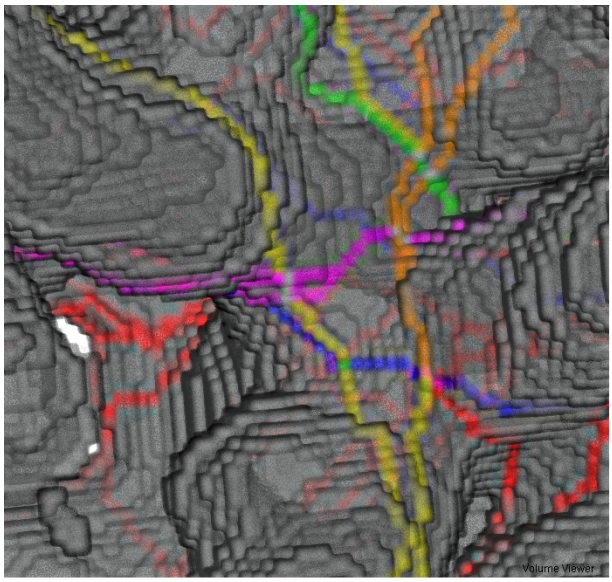

Figure 3.12: Zoomed in percolated network. Different colours (Tab. 3.2) represent the paths in different direction through voxels

Path construction and image creation

As mentioned in *Graph analysis and path search*, we identify the paths in the three principal directions separately. Each time, a copy of the original image is constructed where the paths are labelled with values 0 for background, 1 for RBCs and 2 for Z-paths (4/6 for Y/X). Eventually, the final stack is the sum of these three individual path stacks. The value of each voxel is then converted into a specific colour to construct the final Red-Green-Blue (RGB) image (Tab. 3.2).

X-Paths	Y-Paths	Z-Paths	sum	colour
background	background	background	0	black
RBC	RBC	RBC	3	grey
		Z	4	red
	Y	RBC	6	yellow
		Z	7	orange
X	RBC	RBC	8	blue
		Z	9	pink
	Y	RBC	11	green
		Z	12	white

Table 3.2: Values and colours in the final percolation image for different combinations of voxels in the separate path images

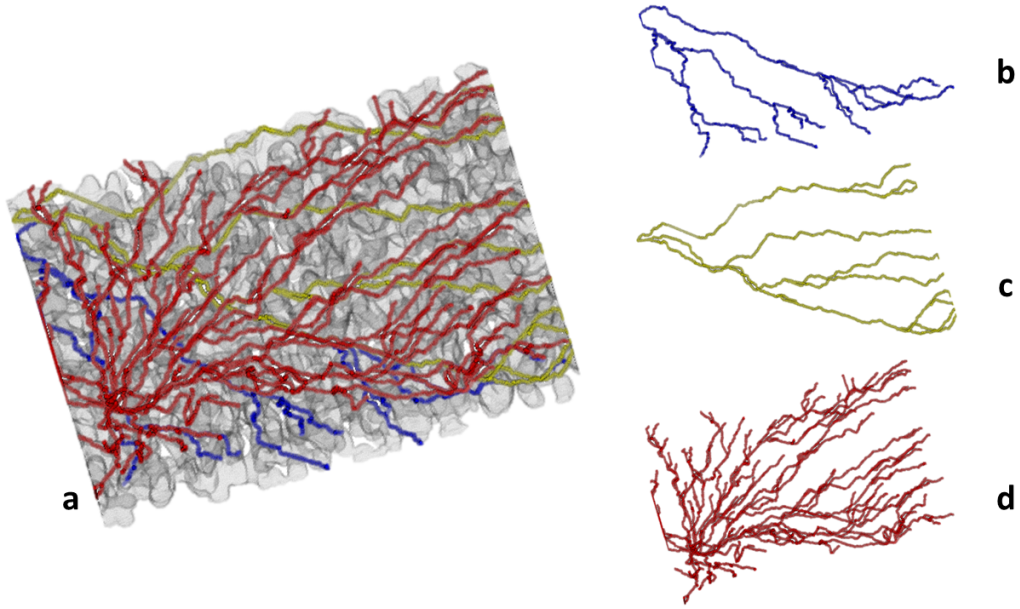

Figure 3.13: Percolation paths in three directions on a sample of red blood cells and Dextran ($\phi_{RBC} = 0.38$, $[Dex] = 50\,\mathrm{mg/\,mL}$) **(a)** Sample of RBCs with percolation paths **(b)** Percolation paths in X-direction **(c)** Percolation paths in Y-direction **(d)** Percolation paths in Z-direction

The percolation algorithm returns these brightly coloured images as seen in figure 3.12. However, we also developed a method to save the paths in X,Y or Z direction and the RBC-shells separately as is seen in figure 3.13. Percolation occurs when paths are found between the opposing sides in X, Y and Z direction. Moreover, the algorithm returns a separate text file where it indicates how many paths exist in X, Y and Z.

3.6 Analysis flowchart

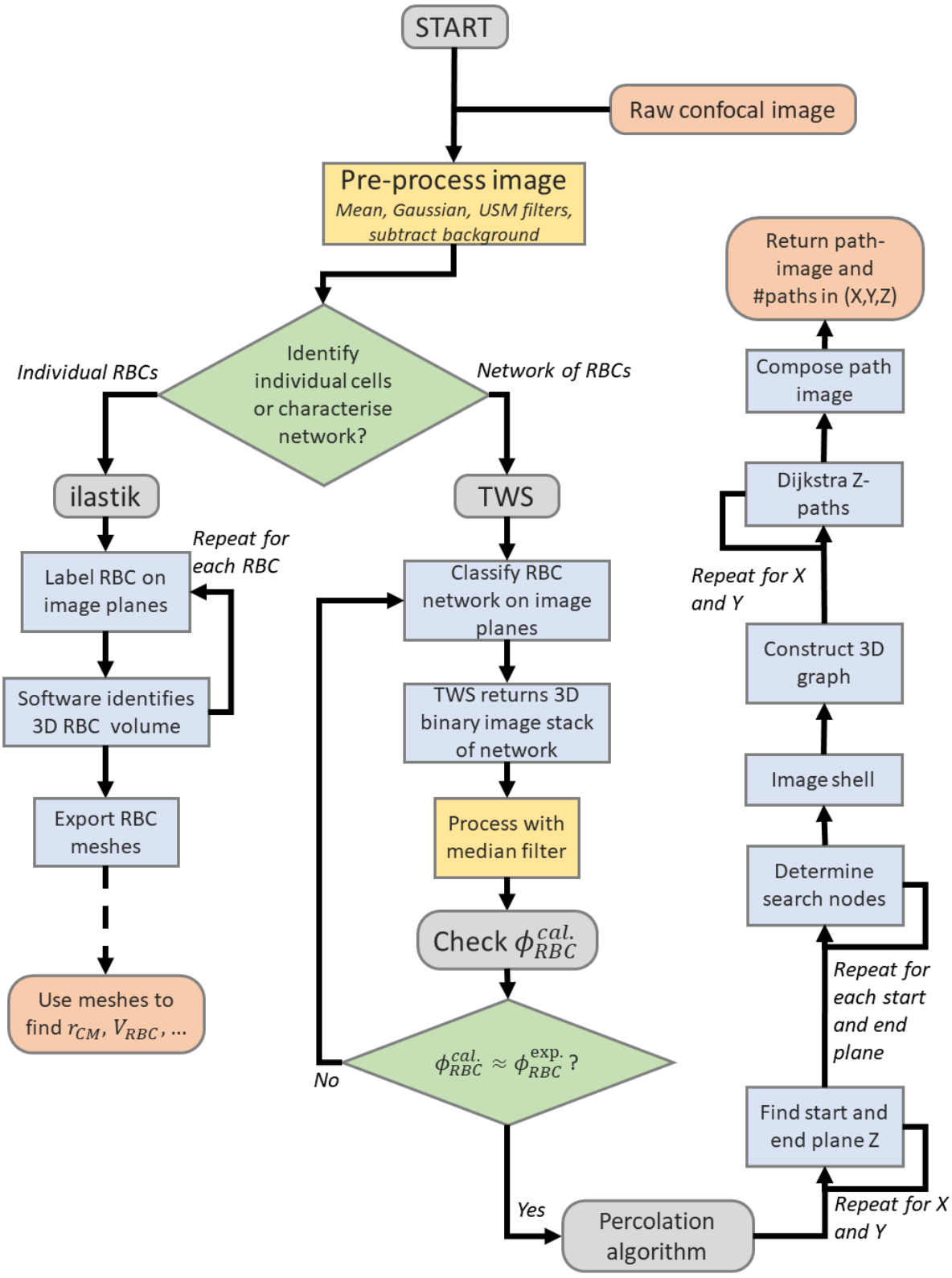

Figure 3.14: Flowchart that describes analysis of confocal images in this work

Chapter 4

Results and discussion

4.1 RBC-dextran phase diagram

A phase diagram gives an overview of the different phases found in mixtures of RBC-Dex systems. In figure 4.1, the RBC volume fractions ϕ_{RBC} and concentration of Dextran [Dex] are set by the sample preparation. Errorbars were calculated for these points, but they are smaller than the markers and are thus not presented.

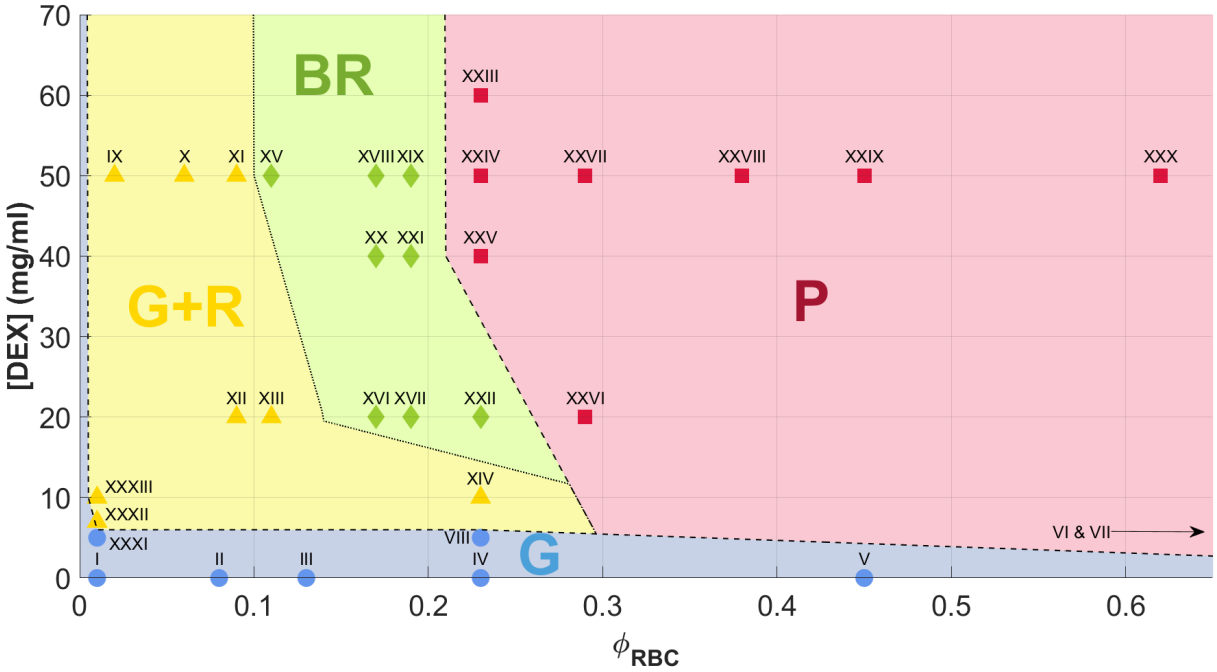

Figure 4.1: Phase diagram for RBC-Dex mixtures. Four distinct phases exist: Gas phase (G), Gas and Rouleaux phase (G+R), Branched Rouleaux phase (BR) and Percolation phase (P). Phase boundaries indicate the gas-aggregate transition and percolation transition. Error bars on data points are smaller than markers and thus not shown. Roman numerals refer to the corresponding confocal images. Link to original tiff stacks in the appendix A.

For RBC-Dex mixtures, we define four different phases: the Gas phase (G), the Gas-Rouleaux phase (G+R), the Branched Rouleaux (BR) phase and Percolated networks (P). The different

phases are separated by the respective phase transition lines.

The gas phase relates to all configurations where no aggregation between particles occurs. All cells are singlets and are homogeneously distributed throughout the sample. Samples enter the rouleaux phase when doublets or larger linear aggregates start to appear. These linear rouleaux are one-dimensional crystals, thus the gas-rouleaux phase is effectively a gas-crystal co-existence, as seen for colloidal spheres in section 2.5. The gas-rouleaux transition line separates the gas phase from the gas-rouleaux co-existence.
We also distinguish the branched rouleaux phase where the rouleaux have grown to such lengths that instead of growing linearly outward, other cells or rouleaux can attach to the side like branches on a tree, although this is not a completely different thermodynamic phase. Branched rouleaux, generally appear as precursor to the completely branched percolation networks. Since the transition from rouleaux to branched rouleaux isn't a pure thermodynamic phase transition it is shown different to the dashed phase transitions.

The final considered phase, is that of the percolated networks. The samples in the percolated phase were all analysed with the percolation algorithm (section 3.5.2) to detect direct percolation. In these samples, there exists at least one path in the X, Y and Z direction of the sample, such that there is a network of RBCs that spans the entire image. Because of this direct detection, the percolation line presents the most accurate phase transition in our phase diagram. Samples in the gas, rouleaux or branched rouleaux phase do not fulfil the requirements of a percolated network.
A more complete discussion of the individual phases is presented in sections 4.1.1 (G), 4.1.2 (R+G), 4.1.4 (BR) and 4.1.5 (P).

Image limitations

We need to consider the limitations of the confocal images and percolation algorithm in light of the implications this gives to the results. Whereas the quality of the images depends on the pixel size, then more pixels are required to create an image with substantial dimensions. We chose to use confocal planes of 512×512 pixels with pixel size 0.481 µm, instead of 1024×1024 with half the pixel size. Going from 512 to 1024 would quadruple the acquisition time of the confocal image from 3 to 10 minutes per stack. Furthermore, the long acquisition times for detailed confocal imaging at large scales is problematic when RBC experiments should preferably be conducted within a 2-4 hour window after drawing blood (section 3.1.4). Similar time increase will occur for the segmentation of the image with TWS (section 3.4.4) and for the final percolation algorithm. Once again, the immensity of these stacks requires a lot of fast computational power.

We could also obtain better detail with small pixel sizes and just limit the dimensions of the scan.To detect percolation, however, we need to investigate the network over large dimensions, preferably a few times the mesh size (Fig. 4.2). Mesh size is the average distance within one 'mesh' of a network. In our RBC networks, mesh size is on the length scale of medium sized rouleaux. As further discussed in section 4.1.3, a typical rouleaux length scale is the average rouleaux length, acquired from the Flory-Schulz distribution. If we assume mesh size to be related to this length scale, we estimate (Eq. 4.5) for percolated samples of $[Dex] = 20\,\mathrm{mg/\,mL}$ ($\phi_{RBC} > 0.26$), a mesh size larger than 7.3 RBCs, roughly $7 - 8\,\mu\mathrm{m}$.

Preferably, we should investigate on images of dimensions larger than a few, e.g. 5 times, the mesh size. The scans should thus have dimensions of at least 35-40 µm, preferably more. In the XY-plane, there is no issue, since we measure planes of $250\,\mu\mathrm{m} \times 250\,\mu\mathrm{m}$. In Z-direction, we are limited to around 30-40 µm (as discussed further in section 5.1).

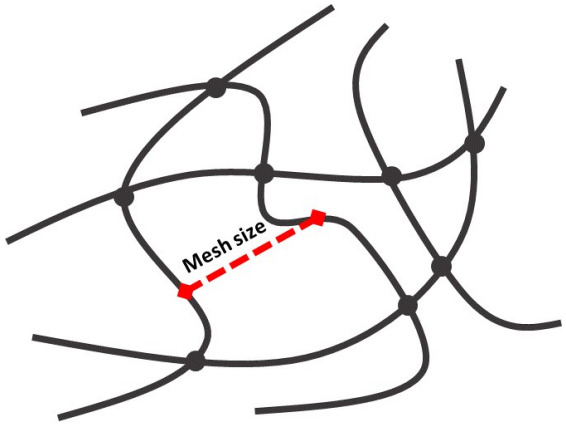

Figure 4.2: Network with mesh size

An implication of this depth limited scanning, is the possibility of a horizontal shift to higher ϕ_{RBC} for the percolation line. We expect this horizontal shift, since we do not scan as deep as multiple mesh sizes into the sample. Moreover, when we are able to scan deeper into the sample, it might reveal that the percolated RBC network only situated close to the bottom and does not span the entire microscope channel (Fig. 5.1a). This will be more probable at the percolated networks close to the transition line. However, we did calculate the volume fractions of RBCs to check whether they coincided with the experimental value. Careful inspection reveals that the RBCs, present in the scanned volume, were dispersed at the same ϕ_{RBC} as the entire sample. Therefore, we can also expect identical ϕ_{RBC} deeper into the sample. Since the aggregation is the same there as at the bottom of the sample, we do expect the same aggregating/percolating behaviour. It would be difficult to claim this if the calculated ϕ_{RBC} at the bottom was considerably higher, which could indicate sedimentation of RBCs. In future work, this can be visually confirmed by scanning deeper into the samples, perhaps with a 2-photon microscope, as discussed in section 5.1.

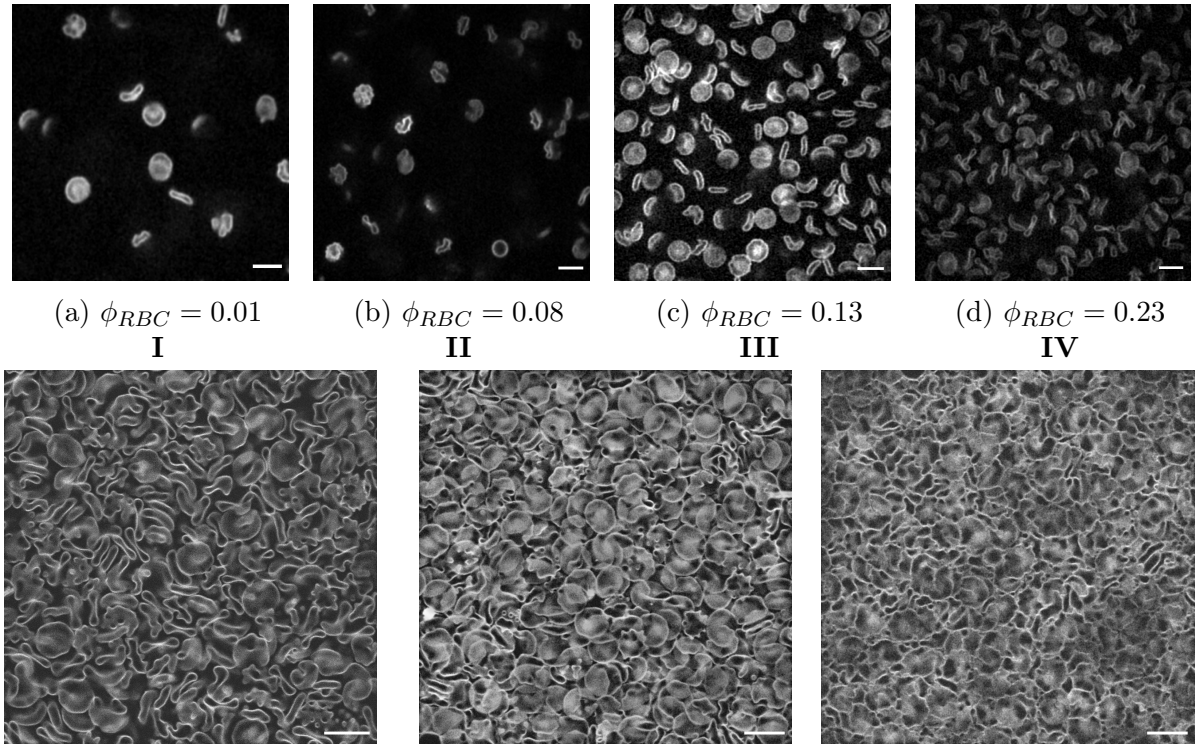

(a) $\phi_{RBC} = 0.01$ **I** (b) $\phi_{RBC} = 0.08$ **II** (c) $\phi_{RBC} = 0.13$ **III** (d) $\phi_{RBC} = 0.23$ **IV**

(e) $\phi_{RBC} = 0.38$ **V** (f) $\phi_{RBC} = 0.75$ **VI** (g) $\phi_{RBC} = 1.00$ **VII**

Figure 4.3: Gas phase (G) RBC mixtures with $[Dex] = [fd] = 0\,\mathrm{mg/\,mL}$ at different volume fraction ϕ_{RBC}. Roman numerals refer to data points in Fig. 4.1. Scale bar 10 µm

4.1.1 Gas Phase

As expected, cells without aggregation (Fig. 4.3), i.e. without Dextran, are all in the gas phase. Further, there turns out to be a threshold concentration of Dex (Fig. 4.5), under which the probability to aggregate is too small to effectively form aggregates. Below $[Dex] = 5\,\mathrm{mg/\,mL}$, aggregated RBCs are not observed in figure 4.5. In both figure 4.3 and 4.5, horizontal slices are shown, that come from confocal image stacks of RBCs at different ϕ_{RBC} and [Dex]. Samples I-IV were imaged with the VT-Hawk confocal all other samples with the Leica (section 3.3).

From figure 4.5 we conclude that for samples of $[Dex] = 0\,\mathrm{mg/\,mL}$, with increasing ϕ_{RBC}, RBCs become more tightly packed together. For high ϕ_{RBC}, this will only be possible due to the deformation of the cells. As discussed in section 2.2, the flexible plasma membrane, allows for these deformations. Up to $\phi_{RBC} = 0.38$ (Fig. 4.3e), the natural discoid shape of RBCs remains clearly visible. For $\phi_{RBC} = 1.00$, it becomes nearly impossible to distinguish discocytes. It has to be said that the shape deformation here is not due to changes in osmotic pressure, as with echinocyte formation. Rather, the cell has to deform because of a lack of available space. Experimentally, the threshold for this deformation has an upper limit of $\phi_{RBC} = 0.75$.

We can also attempt to find this threshold mathematically. If we assume that the RBCs do not deform, retaining their biconcave shape, a maximal packing of RBCs is achieved by stacking RBCs in rouleaux and packing those rouleaux in a hexagonal pattern (Fig. 4.4.b).

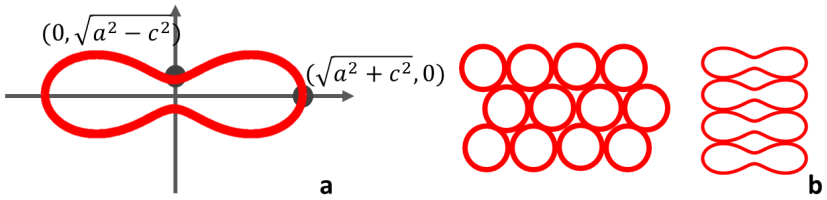

Figure 4.4: Packing of RBCs in a hexagonally packed rouleaux: **(a)** RBC plotted with Cassini equation 4.1; **(b)** Stacking of RBCs by stacking them in rouleaux with hexagonal packing

As is trivial (or easily calculated), hexagonal packing of rouleaux (or cylinders) can achieve a packing density of $\phi_{hex} = 0.9069$. Multiplying this with the packing density of RBCs in a rouleau results in the critical ϕ_{RBC}. RBCs' shape can be described by the Cassini ovals [24] through the equation

$$(x^2 + y^2)^2 - 2c^2(x^2 - y^2) = a^4 - c^4 \tag{4.1}$$

where a and c are constants. Assuming the diameter of a RBC to be $D = 7.5\,\mu\text{m} = 2\sqrt{a^2 + c^2}$ and the thickness in the middle $t = 1\,\mu\text{m} = 2\sqrt{a^2 - c^2}$, the constants a and c are found to be $2.68\,\mu\text{m}$ and $2.63\,\mu\text{m}$ respectively. For the packing density of RBCs in a rouleau we consider the fraction of the RBCs' cross-sectional area to the area of a rectangular box around the cell. In this way, the packing density of RBCs in rouleaux is calculated to be $\phi_{rouleaux} = 0.7554$. The total packing density, or volume fraction, for non-deformable, hexagonally packed RBCs then equals $\phi_{RBC} = \phi_{rouleaux} \cdot \phi_{hex} = 0.69$. That RBCs can be packed without deformation up to $\phi_{RBC} = 0.69$ is also seen experimentally in figure 4.5, although that this is not accurate since we have no samples between $\phi_{RBC} = 0.38$ and $\phi_{RBC} = 0.75$.

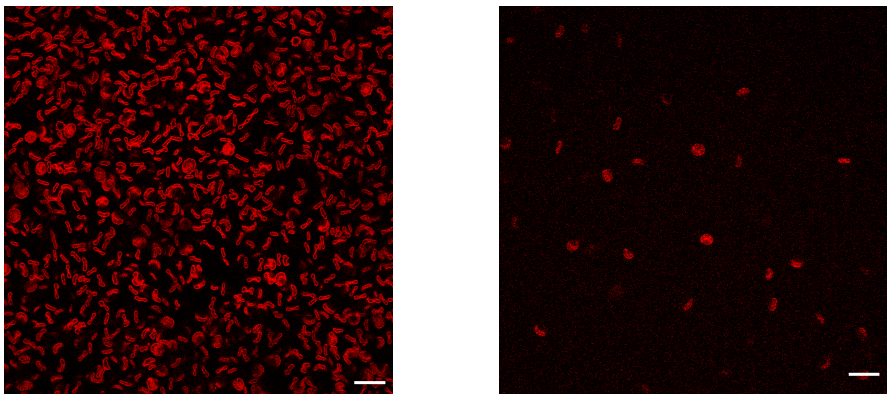

(a) $\phi_{RBC} = 0.23$
$[Dex] = 5\,\text{mg/mL}$
VIII

(b) $\phi_{RBC} = 0.01$
$[Dex] = 5\,\text{mg/mL}$
XXXI

Figure 4.5: Gas phase (G) RBC-Dex mixtures at different volume fraction ϕ_{RBC} and concentration $[Dex]$. Roman numerals refer to data points in Fig. 4.1. Scale bar 20 µm

Apart from samples I-VII, sample VIII and XXXI (Fig. 4.5) are also in the gas phase. Here the aggregation attraction induced by $[Dex] = 5\,\text{mg/mL}$ is not enough to initiate aggregation between RBCs. It confirms that a constant threshold appears at $[Dex] = 5\,\text{mg/mL}$,

independent of the amount of RBCs below which the attraction between RBCs is too small to cause aggregation. For higher ϕ_{RBC}, it is understandable that the gas-rouleaux transition will occur at lower $[Dex]$ since the probability of collisions, with potential aggregation, is higher. More data-points in this part of the phase diagram (low $[Dex]$, high ϕ_{RBC}) should be checked to confirm this hypothesis.

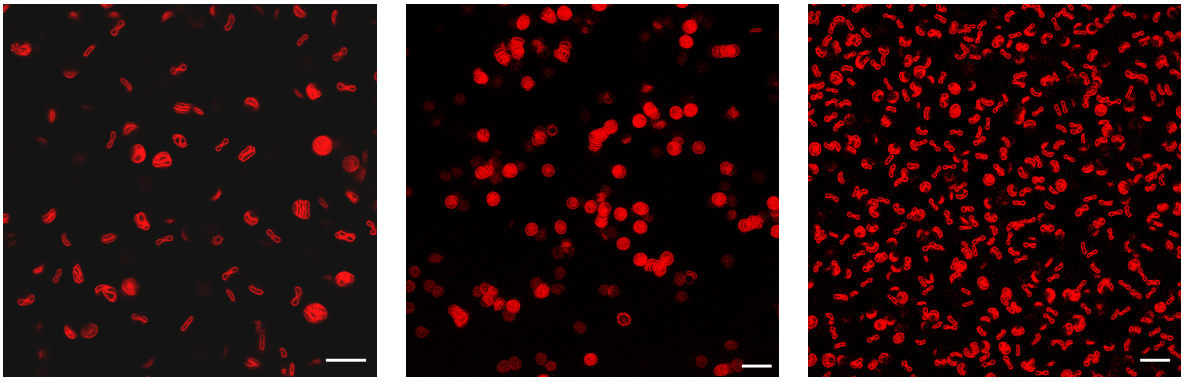

(a) $\phi_{RBC} = 0.02$
$[Dex] = 50\,\mathrm{mg/\,mL}$
IX

(b) $\phi_{RBC} = 0.06$
$[Dex] = 50\,\mathrm{mg/\,mL}$
X

(c) $\phi_{RBC} = 0.09$
$[Dex] = 50\,\mathrm{mg/\,mL}$
XI

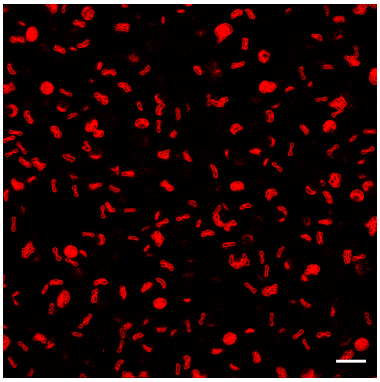

(d) $\phi_{RBC} = 0.09$
$[Dex] = 20\,\mathrm{mg/\,mL}$
XII

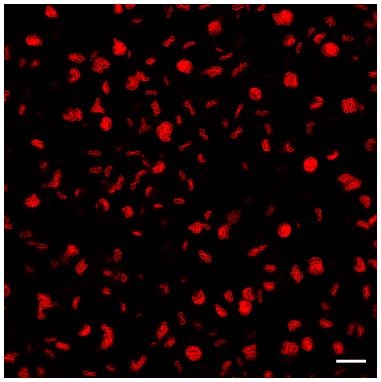

(e) $\phi_{RBC} = 0.11$
$[Dex] = 20\,\mathrm{mg/\,mL}$
XIII

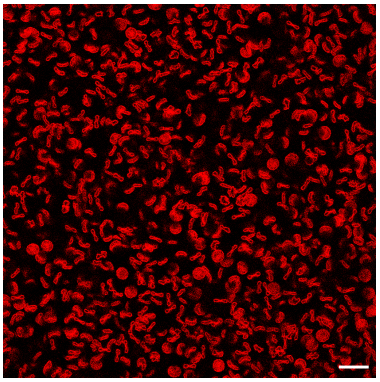

(f) $\phi_{RBC} = 0.23$
$[Dex] = 10\,\mathrm{mg/\,mL}$
XIV

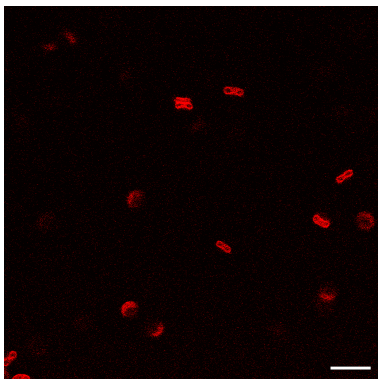

(g) $\phi_{RBC} = 0.01$
$[Dex] = 7\,\mathrm{mg/\,mL}$
XXXII

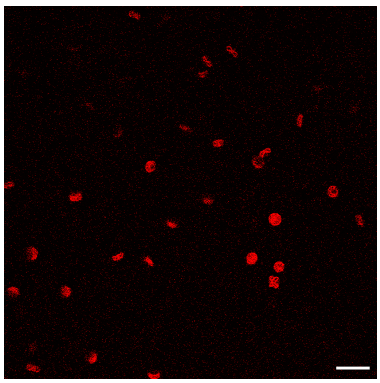

(h) $\phi_{RBC} = 0.01$
$[Dex] = 10\,\mathrm{mg/\,mL}$
XXXIII

Figure 4.6: Gas-Rouleaux co-existence phase (G+R) RBC-Dex mixtures at different volume fraction ϕ_{RBC} and concentration $[Dex]$. Roman numerals refer to data points in Fig. 4.1. Scale bar 20 µm

4.1.2 Rouleaux Phase

When the attraction, brought about by [Dex], surpasses the gas-rouleaux transition line, we enter the rouleaux phase. If a single rouleau is observed, that sample is in the rouleaux phase, indicated in yellow in figure 4.1. The rouleaux phase consists of all aggregates with two or more red blood cells that are linearly packed. Whereas samples directly above the transition lines still predominately consist of singlets, increasingly larger rouleaux appear and their average length increases the further we move away from the transition line. This is further discussed in section 4.1.3. Since most cells in this part of the phase diagram are still singlets, the phase is a coexistence between gas and rouleaux, hence the gas-rouleaux phase co-existence. This is also shown in figure 4.7, where the average number of RBCs per rouleaux for samples XII and XIII is around 2 to 3.

4.1.3 Rouleaux length distribution

Rouleaux size depends on the availability of RBCs (ϕ_{RBC}) and the strength of the interaction, thus c_d. Here we investigate the rouleaux formation as a step towards percolation network creation. When using Dextran as a depletant, rouleaux formation is very clear. With Dex, RBCs are almost exclusively found to aggregate linearly into rouleaux, whereas with *fd* (see section 4.2.2) clumps of RBCs rather appear.

Each RBC has two faces where another RBC can attach. Rouleaux formation then depends on the probability m that two RBCs have aggregated. We'll call that a reacted group. Single RBCs on the other hand, have no reacted groups thus the probability of finding singlets is $1 - m$. This approach is similar to the one Flory [103] used to describe the molecular size distribution in linear condensation polymers.
The probability of finding a rouleau of k RBCs equals

$$P_k = m^{k-1}(1 - m) \tag{4.2}$$

Let now N_0 be the initial number of 'free' RBCs, then the total number of rouleaux N of any size is given as $N = N_0(1 - m)$. We can then define the number of rouleaux of k units

$$N_k = NP_k = N_0(1 - m)^2 m^{k-1} \tag{4.3}$$

Finally, the weight fraction for rouleaux of k RBCs corresponds to $w_m(k) = k\frac{N_k}{N_0}$ which produces the *Flory-Schulz distribution* [103]

$$w_m(k) = (1 - m)^2 k m^{k-1} \qquad \overline{k} = \frac{1 + m}{1 - m} \tag{4.4}$$

where $\overline{k}$ is the average number of RBCs per rouleau, thus related to the average length of said rouleau.

In figure 4.7.a the weight fraction w_m for rouleaux is given for different ϕ_{RBC} at [Dex] = 20 mg/ mL. The roman numerals refer to the phase diagram (Fig. 4.1). The size of different rouleaux was determined by counting the number of cells per rouleau manually. The cells were counted in a 2D horizontal plane of the 3D image stacks. For each 2D image, more than 100 individual cells were observed, thus increasing the confidence in our statistics. As long as there is no percolation, and thus 3D network, we assume that the rouleaux are dispersed

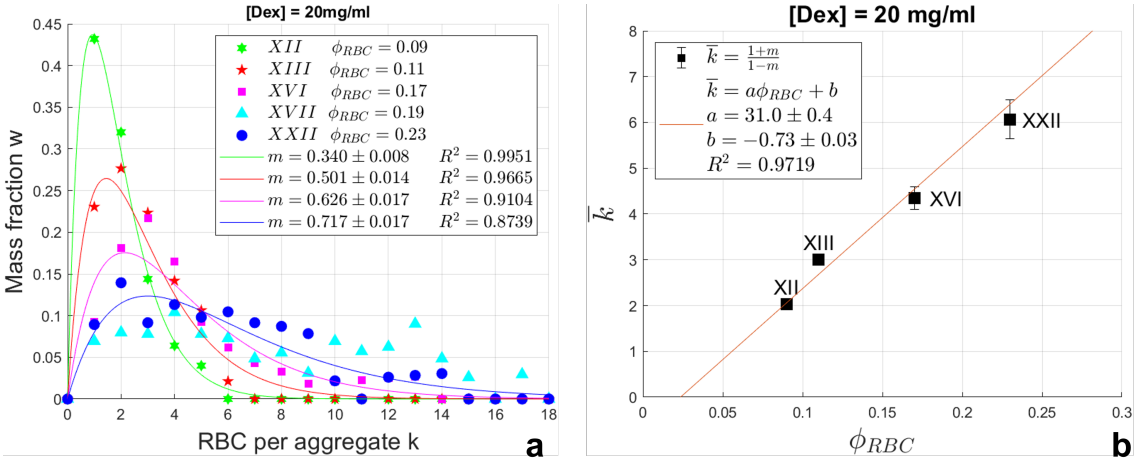

Figure 4.7: Distribution of RBCs per rouleau k for RBC-Dex mixtures. Roman numerals refer to same data points in Fig. 4.1 **(a)** RBC mass fraction $w_m(k)$ in function of number of RBCs per rouleau k. Fitted with the Flory-Schulz distribution (eq. 4.4) **(b)** Average number of RBCs per rouleau $\overline{k}$ in function of ϕ_{RBC}

evenly across the sample. Naturally, a count in 3D would be more accurate but was presumed to laborious by hand.

The data was then fitted with the model of the Flory-Schulz distribution (Eq. 4.4) returning the aggregation probability m. The fit for $\phi_{RBC} = 0.19$ had an $R^2 \approx 0.4$ and therefore was not used in further analysis. In figure 4.7.b, $\overline{k}$ was calculated from m and presented in function of ϕ_{RBC}. At constant Dex concentration (20 mg/ mL), there appears to be a strong linear relation between ϕ_{RBC} and $\overline{k}$.

$$\overline{k} = 31.0 \cdot \phi_{RBC} - 0.73 \tag{4.5}$$

From the phase diagram (Fig. 4.1), percolation appears (for [Dex]=20 mg/ mL) above $\phi_{RBC} = 0.26$. This would correspond to an average rouleau length of 7.33 RBCs per rouleau. Branched rouleaux appear for $\phi_{RBC} > 0.14$ and thus $\overline{k} > 3.61$. *This, however, does not mean that all rouleaux with more than three red blood cells will branch or one with more than 7 cells forms networks. It merely suggests branching and percolation based on the average rouleau length. As seen in figure 4.7.a, rouleaux much longer than $\overline{k}$ are common in the tail of the Flory-Schulz distribution.*

Analysis of rouleaux lengths, reveals information about the aggregation mechanism in the rouleaux phase. Although not in the rouleaux phase, the addition of data points XVI and XXII extends the distribution into the BR phase, improving the statistics of our analysis.

In future work, examination of the rouleaux lengths should be expanded to samples of other $[Dex]$ as well, to get a complete overview of the aggregate phase. At higher dextran concentrations, we predict longer aggregates to form at smaller ϕ_{RBC}, which would shift the curve in figure 4.7.b to the left.
Further, we believe a more accurate way of conducting rouleaux length measurements is to make binary versions of the confocal images with TWS. From such binary images, the individual aggregates can be identified and their volume/surface area easily determined. If we can relate the total volume of a rouleau to that of the RBCs in that rouleau, it would allow to cal-

culate the number of cells in that rouleaux. If such program can be established, it would allow for an analysis in three-dimensional space and based on numbers rather than visual counting.

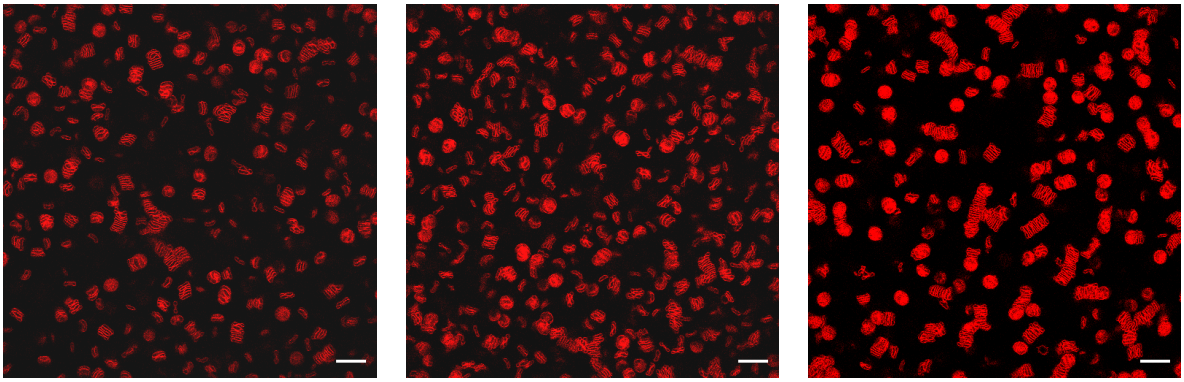

(a) $\phi_{RBC} = 0.11$ $[Dex] = 50\,\mathrm{mg/\,mL}$ **XV**

(b) $\phi_{RBC} = 0.17$ $[Dex] = 20\,\mathrm{mg/\,mL}$ **XVI**

(c) $\phi_{RBC} = 0.19$ $[Dex] = 20\,\mathrm{mg/\,mL}$ **XVII**

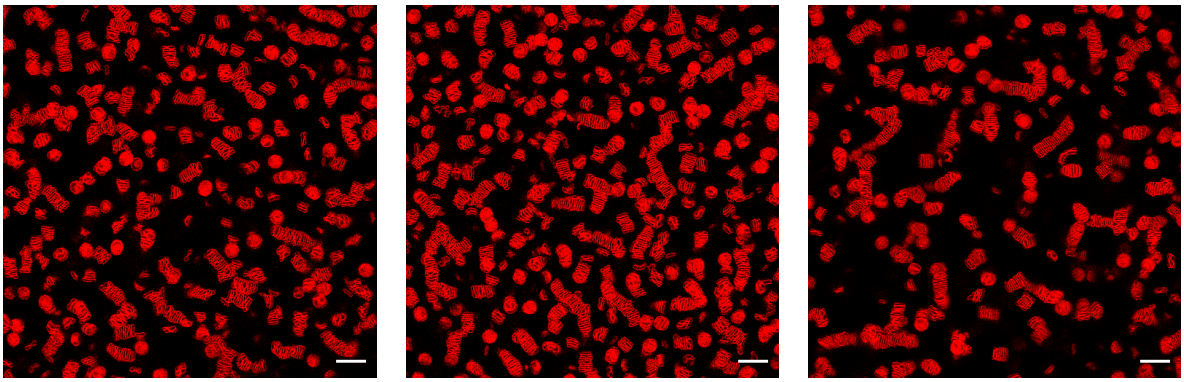

(d) $\phi_{RBC} = 0.17$ $[Dex] = 50\,\mathrm{mg/\,mL}$ **XVIII**

(e) $\phi_{RBC} = 0.19$ $[Dex] = 50\,\mathrm{mg/\,mL}$ **XIX**

(f) $\phi_{RBC} = 0.17$ $[Dex] = 40\,\mathrm{mg/\,mL}$ **XX**

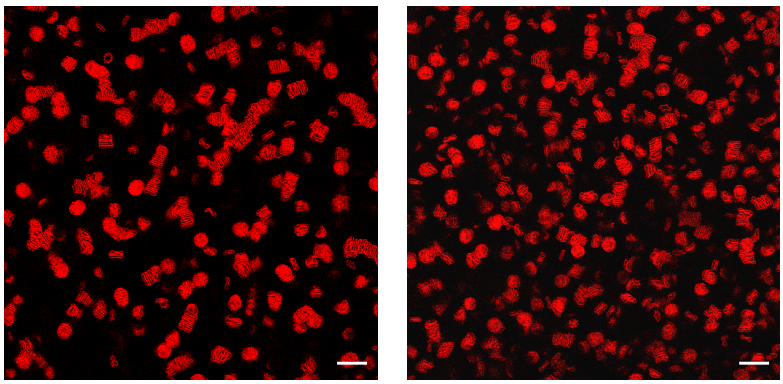

(g) $\phi_{RBC} = 0.19$ $[Dex] = 40\,\mathrm{mg/\,mL}$ **XXI**

(h) $\phi_{RBC} = 0.23$ $[Dex] = 20\,\mathrm{mg/\,mL}$ **XXII**

Figure 4.8: Branched Rouleaux phase (BR) RBC-Dex mixtures at different volume fraction ϕ_{RBC} and concentration $[Dex]$. Roman numerals refer to data points in Fig. 4.1. Scale bar 20 µm

4.1.4 Branched Rouleaux Phase

Branched rouleaux do not form a phase much different from the gas-rouleaux phase. However, it forms a precursor for the percolated phase as branching is a prerequisite for percolation. As seen in figure 4.8, BR phase consists almost exclusively of aggregated RBCs. A second feature of the branched rouleaux phase is the increased average rouleaux length e.g. 4.3 RBC per rouleaux for XVI (Figs. 4.8b and 4.7.b) and 6.1 for XXII (Fig. 4.8h).

The criterion to distinguish BR phase is based on the occurrence of branching. Dex ensures that RBCs form linearly ordered rouleaux, maximising the attraction interaction. When large rouleaux are formed, the possibility of RBCs aggregating to the side increases. Other cells can then sprout new rouleaux that are branched from the original rouleau. Specimens that show such branching behaviour are classified into the branched rouleaux phase.
Future research into the branched rouleaux phase should, according to us, focus on the aggregation of rouleaux into percolation structures. As most RBCs are, by now, stacked in rouleaux of different lengths, the aggregation becomes effectively one of rods opposed to singlet cells. Such an approach potentially can characterise branching.

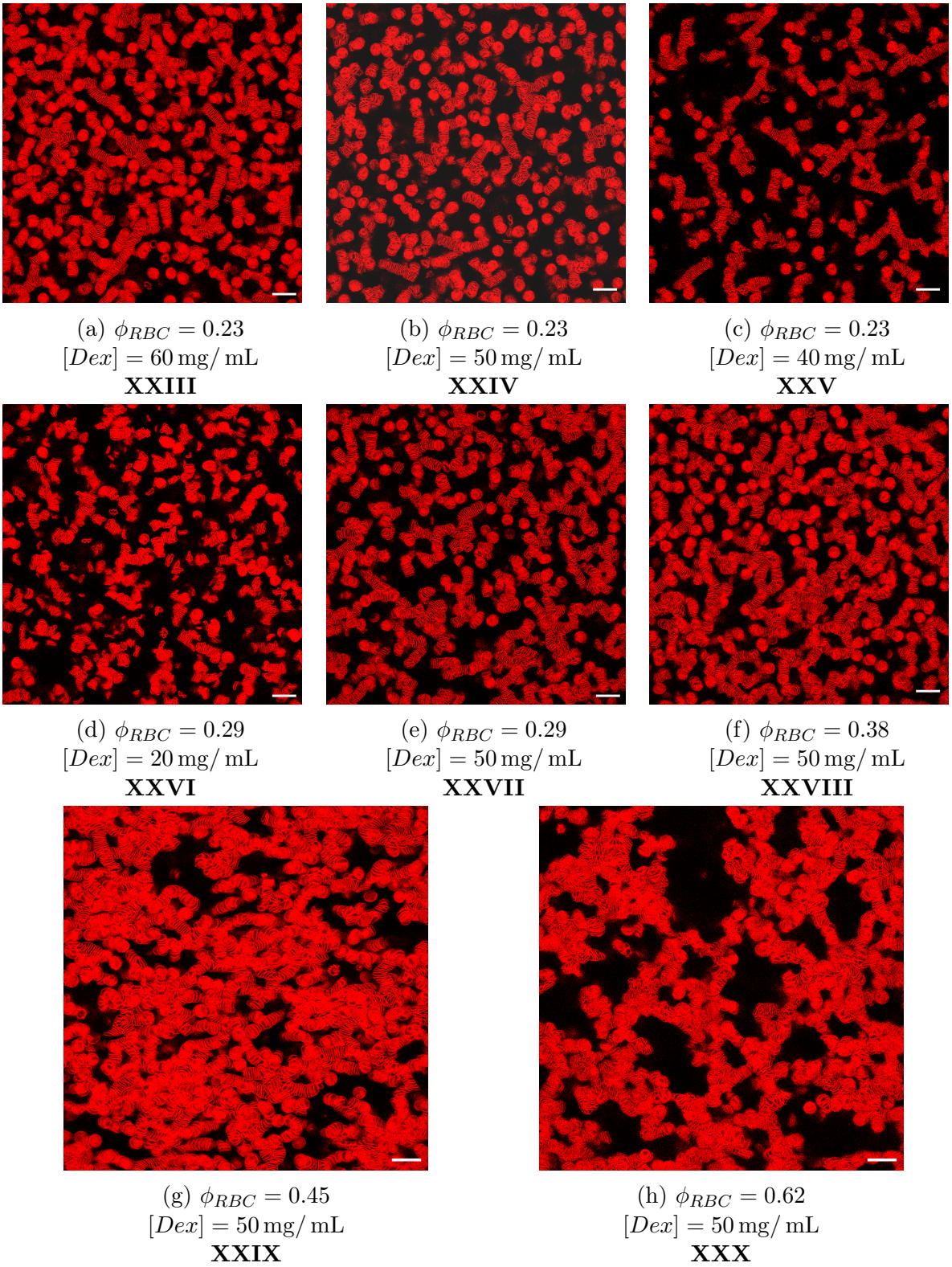

(a) $\phi_{RBC} = 0.23$ $[Dex] = 60\,\mathrm{mg/\,mL}$ **XXIII**

(b) $\phi_{RBC} = 0.23$ $[Dex] = 50\,\mathrm{mg/\,mL}$ **XXIV**

(c) $\phi_{RBC} = 0.23$ $[Dex] = 40\,\mathrm{mg/\,mL}$ **XXV**

(d) $\phi_{RBC} = 0.29$ $[Dex] = 20\,\mathrm{mg/\,mL}$ **XXVI**

(e) $\phi_{RBC} = 0.29$ $[Dex] = 50\,\mathrm{mg/\,mL}$ **XXVII**

(f) $\phi_{RBC} = 0.38$ $[Dex] = 50\,\mathrm{mg/\,mL}$ **XXVIII**

(g) $\phi_{RBC} = 0.45$ $[Dex] = 50\,\mathrm{mg/\,mL}$ **XXIX**

(h) $\phi_{RBC} = 0.62$ $[Dex] = 50\,\mathrm{mg/\,mL}$ **XXX**

Figure 4.9: Percolation phase (P) RBC-Dex mixtures at different volume fraction ϕ_{RBC} and concentration $[Dex]$. Roman numerals refer to data points in Fig. 4.1. Scale bar 20 µm

4.1.5 Percolation Phase

The final phase manifests itself at high ϕ_{RBC} and relatively high $[Dex]$. As discussed in section 2.6, percolated networks span the entire confocal image. In section 3.5.2, we then presented the direct way of detecting percolation through analysing confocal images and searching paths through the RBC structure. Percolated networks are found as soon as paths appear in the three principal directions: X,Y and Z.

The images that correspond to the percolated networks, are shown in figure 4.9. In the horizontal planes, percolated networks show rouleaux of different sizes. The average rouleaux has considerable length compared to the other phases. Furthermore strong rouleaux branching occurs, which enables the construction of the percolated networks. For high ϕ_{RBC}, e.g. samples XXVIII (Fig. 4.9f) and XXIX (Fig. 4.9g), there appear to be large aggregated clumps, composed of individual rouleaux. This would suggest that after rouleaux formation, these rouleaux themselves can be viewed as the aggregating particles. Further RBC aggregation then becomes aggregation of rouleaux.

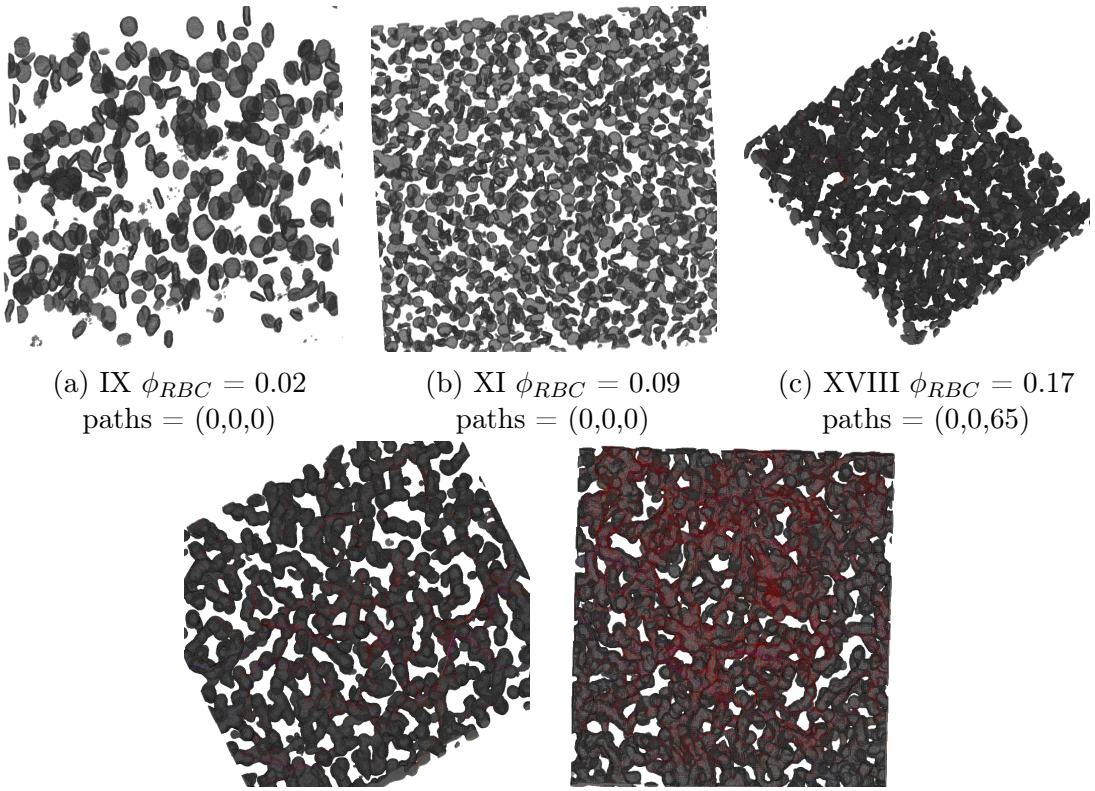

(a) IX $\phi_{RBC} = 0.02$ paths = (0,0,0)

(b) XI $\phi_{RBC} = 0.09$ paths = (0,0,0)

(c) XVIII $\phi_{RBC} = 0.17$ paths = (0,0,65)

(d) XXIV $\phi_{RBC} = 0.23$ paths = (72,12,1139)

(e) XXVIII $\phi_{RBC} = 0.38$ paths = (143,60,21306)

Figure 4.10: 3D visualisation of RBC networks with percolation paths in RBC-Dex samples with $[Dex] = 50\,\mathrm{mg/\,mL}$. Total number of found paths in (X,Y,Z) direction. Roman numerals refer to data points in Fig. 4.1. Colours as defined in Tab. 3.2

Figure 4.10 shows the output images from the percolation algorithm for constant $[Dex] = 50\,\mathrm{mg/\,mL}$ at different ϕ_{RBC}. The number of paths in (X,Y,Z) is given for each sample.

With increasing ϕ_{RBC}, we observe an increase in the number of identified paths. It has to be mentioned that this does not give any information about the complexity of the network. Due to the nature of the percolation algorithm, multiple paths can cover the same RBC or rouleau. Remember that paths are searched between opposing sides of the image between *useful* nodes. Should the network connect all points in one side, this side would be presented as just 1 useful node. Therefore, the absolute number of paths is not used to quantify the percolation, it can, however, show trends.
Apart from increasing number of paths with increasing ϕ_{RBC}, we also observe initial path formation in Z-direction before percolation in X and Y. Two explanations are presented. The first one, the most obvious, is that the scanned length in Z ($< 50\,\mu\mathrm{m}$) is much smaller than the scanned lengths in X and Y ($\approx 250\,\mu\mathrm{m}$). Accordingly, it is much easier for aggregates of RBCs to span the Z-direction e.g. through long rouleaux.
The second explanation is that rouleaux anchor to the bottom of the sample and the network is grown from these rouleaux. It is observed that RBCs can stick to the walls through the same aggregation attraction interaction. Despite density matching, RBCs are always pushed to the bottom through the depletion force. Therefore, a large number of RBCs are present at the bottom and can potentially aggregate with cells stuck to the wall. This then produces a rouleaux, anchored to the bottom, as seen in figure 4.11. Besides the possibility of networks forming from these anchors, they also provide long rouleaux in Z-direction, and thus easy Z-paths. We hypothesise this but the dynamics of network formation are not further elaborated. For all samples at constant concentration of $[Dex]$ with increasing ϕ_{RBC}, the observation of Z-paths is the precursor of the percolated networks.

As seen in figure 4.11, anchoring of rouleaux to the bottom of the microscope channels potentially influences the construction of percolated networks. One can also hypothesise that more structured RBC networks could be engineered by applying a repulsive coating to the channel wall but all the while including non-coated anchoring points. The RBC networks are then allowed to grow from these anchoring points outward. This is a suggested approach that can be researched in future work.

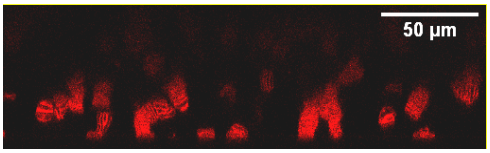

Figure 4.11: XZ-Cross section of image XXI shows anchoring of rouleaux to the wall

In figure 4.12, a complete percolation analysis is shown for sample XXV ($\phi_{RBC} = 0.23$ and $[Dex] = 40\,\mathrm{mg/\,mL}$). The same procedure was performed on all images in the percolated, rouleaux and branched rouleaux phase. From the raw output files of the percolation algorithm, figure 4.10, it is difficult to see the paths. Therefore , we separate in figure 4.12 the percolation image into it's constituents: an image of the RBC shells and images of the paths in X,Y and Z individually. The RBC shells (Fig. 4.12a) resemble the original confocal images but more transparent. The paths are divided into the paths in each direction. The blue paths in X-direction (Fig. 4.12b) and the yellow paths in Y-direction (Fig. 4.12c) clearly show that the RBCs span the entire XY plane. In figures 4.12d and 4.12e, the X and Y paths in Z-direction are projected on top of each other to openly show the connections between opposite sides. For the Z-direction in red (Fig. 4.12f), this connection is less clearly seen since the final plane

is of course not well defined. In Z-direction, paths are investigated between the bottom of the specimen (at the wall) and the highest plane that exceeds a certain threshold of non-background pixels. We often observe that at the top the RBCs extend as spires of rouleaux. A perfect network is not anymore visible deep into the sample. Therefore, the top plane in Z-direction will give scattered points in all the separate spires, as seen in figure 4.12g. We also show an image of the RBCs overlaid with the different paths (Fig. 4.12h). Since the paths are posed on top of the RBCs, this does not necessarily mean that the paths also go through this top-layer of the network. It is mainly shown for creating a better visual understanding.

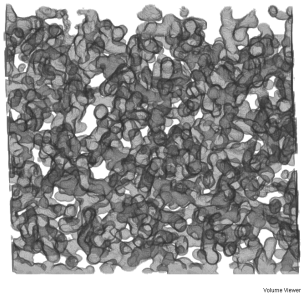

(a) RBCs

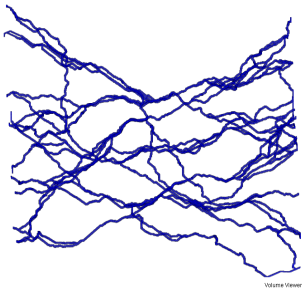

(b) X-paths = 155

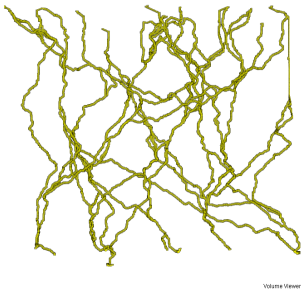

(c) Y-paths = 144

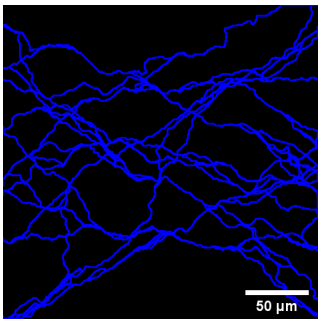

(d) X-paths stack projected along Z-direction shows that X-paths span the image

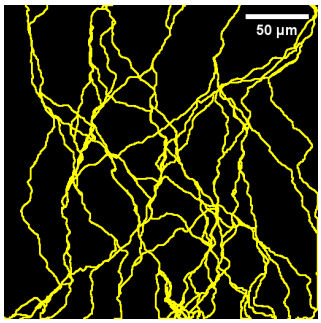

(e) Y-paths stack projected along Z-direction shows that Y-paths span the image

(f) Z-paths = 350

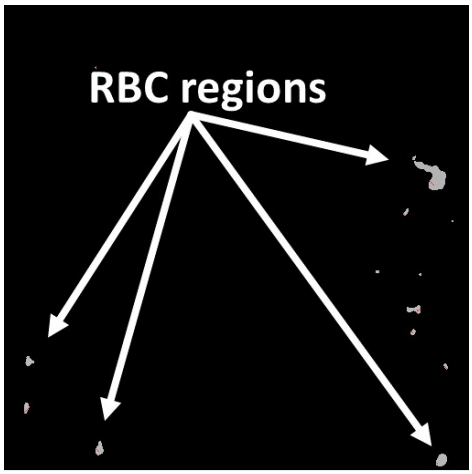

(g) Top plane in Z-direction

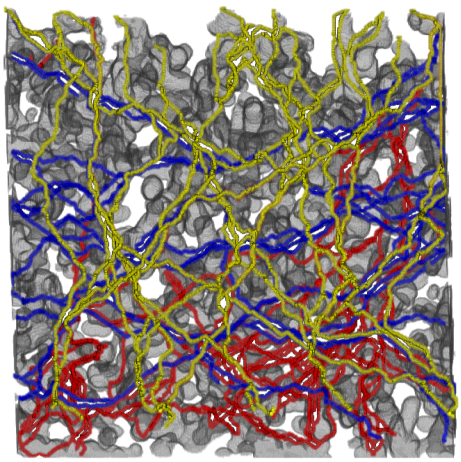

(h) RBCs with path overlay

Figure 4.12: Percolation analysis of sample XXV $\phi_{RBC} = 0.23$ and $[Dex] = 40\,\mathrm{mg/\,mL}$, image 4.9c

In table 4.1, we present the images used to detect percolation. These images were classified using WEKA segmentation. This confirmed the experimental ϕ_{RBC} through volume fraction control (section 3.5.1). The output images of the percolation algorithm for the samples in table 4.1 can be accessed by the reader as seen in Appendix A.

Sample	Exp. ϕ_{RBC}	[Dex] (mg/ mL)	Calc. ϕ_{RBC}	X paths	Y paths	Z paths
IX	0.02	50	0.034	0	0	0
X	0.06	50	0.057	0	0	0
XI	0.09	50	0.107	0	0	0
XII	0.09	20	0.074	0	0	0
XV	0.11	50	0.095	0	0	8
XVI	0.17	20	0.127	0	0	2
XVII	0.19	20	0.183	0	0	127
XVIII	0.17	50	0.19	0	0	65
XIX	0.19	50	0.184	0	0	27
XXII	0.23	20	0.187	0	0	82
XXIV	0.23	50	0.202	72	12	1139
XXV	0.23	40	0.227	130	144	350
XXVI	0.29	20	0.257	24	56	6280
XXVIII	0.38	50	0.356	143	60	21306
XXIX	0.45	50	0.414	12 †	8 †	16 †

Table 4.1: Images classified by WEKA segmentation. Table shows calculated and experimental volume fractions ϕ_{RBC}. The number of paths found by the percolation algorithm are given for X,Y and Z separate. †Percolation algorithm does not search all paths. These are too numerous and weren't found after 2 days. This simplified algorithm only checks whether percolation exist

Radial distribution function

To analyse the different phases, and differentiate between the individual samples, it is interesting to look at the radial distribution function $g(r)$ (section 2.6) as well as the 3D reconstructions of individual cells. The 3D meshes of the RBCs can be used to determine the bending energies and quantitatively describe the deformation of the cells. As discussed in section 3.4.3, ilastik can be used to mesh individual cells, which would allow the calculation of bending energies. However, for the determination of $g(r)$, we would need to identify tens to hundreds of RBCs to find their r_{CM}, which is necessary to calculate $g(r)$. Then this method of labelling each individual cell at a time, is deemed too time consuming.
One different method we tried, was to use Trainable Weka Segmentation to label individual cells. Without going to deep into this, we trained the TWS software to recognise RBCs' cytosol (Fig. 4.13.b) and label that in comparison to the background and fluorescent cell membranes. From the binary image of these cytosols, we could find the centres of mass of the individual cytosols, and thus cells. The cytosols were selected instead of the entire RBCs, since RBCs can touch each other (or aggregate), and then be interpreted as one object by the computer. Effectively, we would then find one r_{CM} of the aggregate instead of the constituents.

In figure 4.13, we attempted to find r_{CM} for the individual RBCs of a single rouleau. The centres of mass are then used to calculate $\frac{dN}{dr}$ and $g(r)$ for the RBC marked with the yellow dot. Apart from the obvious, poor statistics, figures 4.13.c and 4.13.d show that the neighbouring RBCs in a linear rouleaux are evenly spaced. This is observed as three distinct peaks at equally spaced distance from each other, the thickness of a RBC (approximately 1 µm). In future work on these RBC networks, g(r) can be a powerful tool to characterise the individual phases.

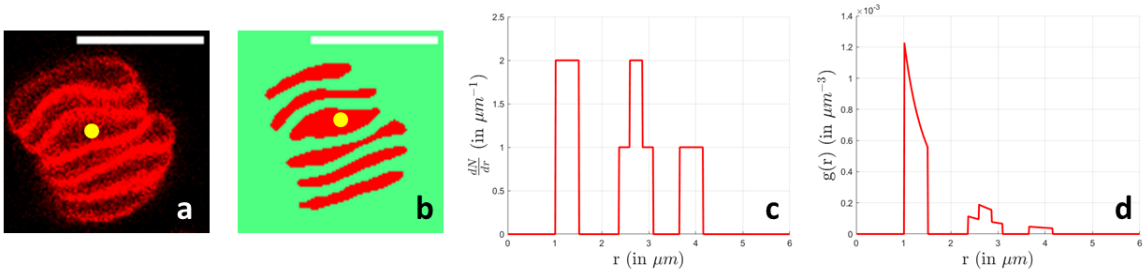

Figure 4.13: Calculating the radial distribution function: **(a)** raw image. Scale is 8 µm; **(b)** segmented cytosols. Scale is 8 µm; **(c)** $\frac{dN}{dr}$ in function of r for the RBC marked with yellow dot. $dr = 0.5$ µm; **(d)** $g(r)$ for the RBC marked with yellow dot. $dr = 0.5$ µm

In future work on percolated phases of RBCs, the establishment of a radial distribution function can be used to determine the fractal dimension d_f of the networks, allowing a quantitative comparison of network complexity. Furthermore, it's fruitful to expand the quest for percolated networks at high ϕ_{RBC} to the low $[Dex]$ regions. So far it is unclear whether a gas-percolation transition exists, or that, these phases are always separated by a (branched) rouleaux phase.

4.2 RBC-*fd* phase diagram

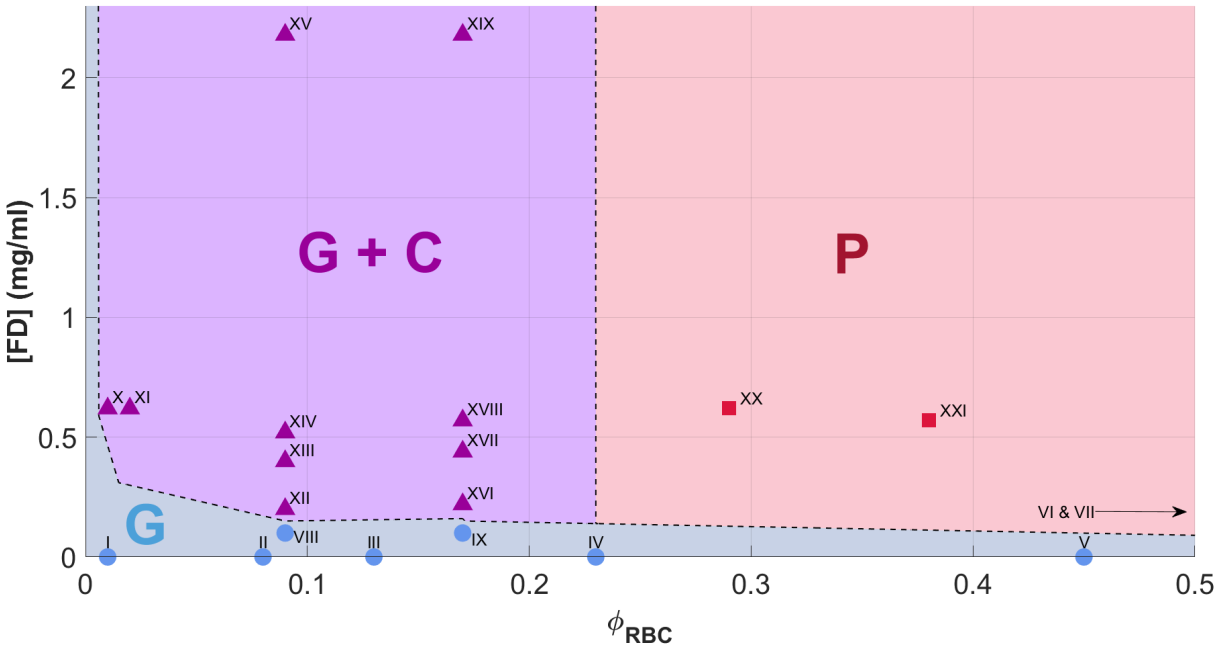

Figure 4.14: Phase diagram for RBC-*fd* mixtures. Three distinct phases are identified: Gas phase (G), Gas and Cluster phase (G+C) and Percolation phase (P). Phase boundaries indicate the gas-cluster transition and percolation transition. Error bars on the data points are smaller than markers and thus not shown. Roman numerals refer to the corresponding confocal images

Since in this thesis, we focus mainly on the aggregation of RBCs due to Dex, less data points were examined for the RBC-*fd* mixtures. Nonetheless, we present a phase diagram based on the available images of RBC-*fd* samples. As seen in figures 4.15, 4.16 and 4.17, the dimensions of most of the images are often smaller than $(250\,\mu\mathrm{m} \times 250\,\mu\mathrm{m})$ as was standard in the RBC-Dex phase diagram. The reason is that these images were acquired in experiments long before we developed the percolation algorithm. At that time, it was deemed important to visualise the aggregates at the highest possible resolution, rather than have large dimensions to prove percolation.

For RBC-*fd* mixtures, we identify three different phases: the Gas phase (G), the Gas-Cluster co-existence phase (G+C) and the Percolation phase (P). Similarly to the Dextran diagram, different phases are separated by a phase transition line, connected between two points of different phase. The characteristics of these individual phases are discussed in sections 4.2.1,4.2.2 and 4.2.3.

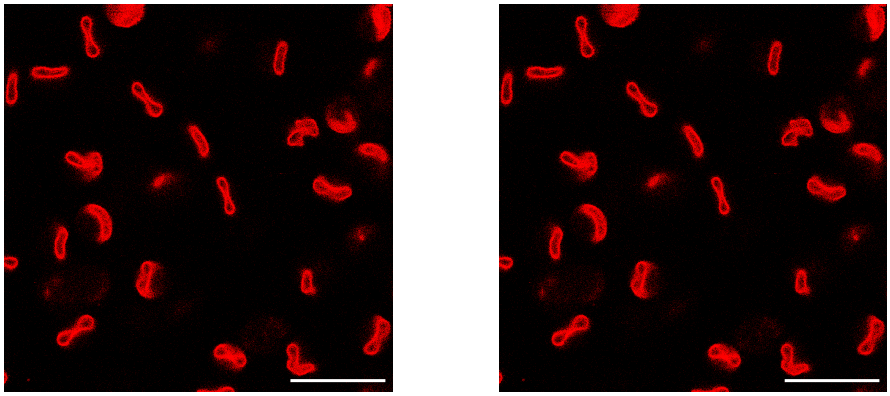

(a) $\phi_{RBC} = 0.09$
$[fd] = 0.10\,\mathrm{mg/\,mL}$
VIII

(b) $\phi_{RBC} = 0.17$
$[fd] = 0.10\,\mathrm{mg/\,mL}$
IX

Figure 4.15: Gas phase (G) RBC-*fd* mixtures at different volume fraction ϕ_{RBC} and concentration $[fd]$. Roman numerals refer to data points in Fig. 4.14. Scale bar 20 µm

4.2.1 Gas phase

In the gas phase, again, no aggregates are present and we only observe singlet RBCs. With increased $[fd]$, RBCs start to aggregate and clump together. Samples enter the cluster phase.

Samples I-VII are the same as in section 4.1.1 and seen in figure 4.5. Furthermore, we observe two points were the RBCs are in the gas phase, Fig. 4.15. This confirms that also for *fd* there is a certain concentration threshold before aggregation occurs.

4.2.2 Cluster phase

At higher concentrations of *fd*, RBCs aggregate and form doublets, small rouleaux or clusters. Since these aggregates are not always linearly stacked in rouleaux, we distinguish between the aggregates formed by Dex and *fd*. With Dextran, we clearly observe aggregation of RBCs into rouleaux of increasing length. Instead of exclusively linear rouleaux, we find much more clumps of RBCs. This clustering behaviour also has important consequences for the percolation of these samples. The requirements for percolation are identical to those for Dex samples. Since many cells are still singlets (Fig. 4.16), there once again is a coexistence between the cluster and gas phase. Aggregates do not form ideal linear rouleaux, thus branching can not be defined. For *fd*, we observe that RBCs more easily attach in other configurations than the columnar way to form rouleaux (as discussed in section 4.1.3). We can look at figure 4.16i and note that, besides cluster formation, the rouleaux that do form are more diagonal than linear. All these observations suggest that the maximal overlap volume V_{ov} is achieved without columnar stacking as with Dex.

This could be due to two reasons. First, the range of interactions (section 1.2) of *fd* ($\Delta = 440\,\mathrm{nm}$) is much longer than Dex ($\Delta_0 = 11.2\,\mathrm{nm}$). This means that RBCs can easily stick to a surface which is not smooth but curved. Second, we know that *fd* is a pure depletant and does not stick to the surface. Thus, We suggest that *fd* depletion allows the cells to aggregate more freely and attach e.g. to each other's sides.

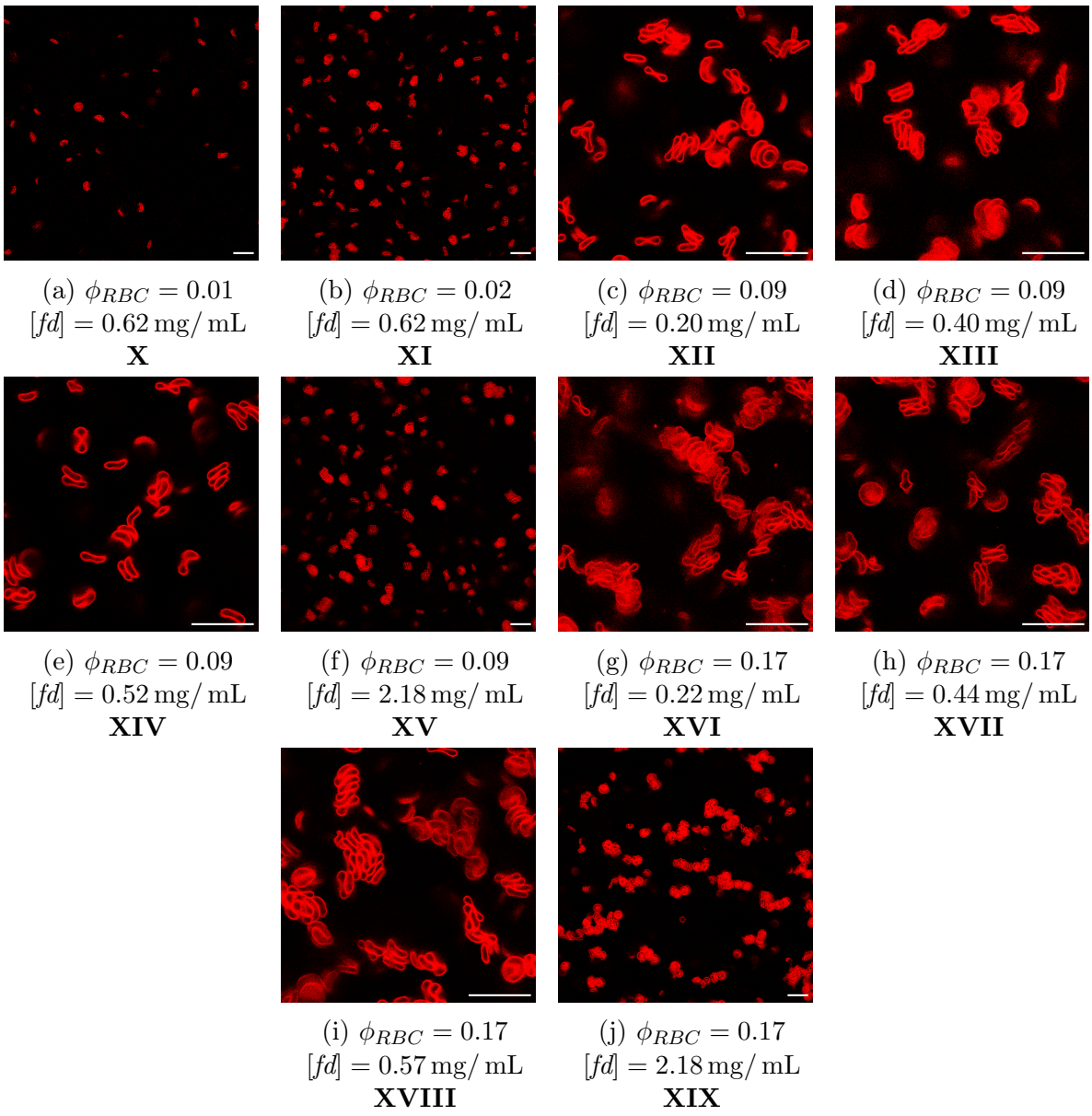

(a) $\phi_{RBC} = 0.01$ $[fd] = 0.62\,\text{mg/mL}$ **X**

(b) $\phi_{RBC} = 0.02$ $[fd] = 0.62\,\text{mg/mL}$ **XI**

(c) $\phi_{RBC} = 0.09$ $[fd] = 0.20\,\text{mg/mL}$ **XII**

(d) $\phi_{RBC} = 0.09$ $[fd] = 0.40\,\text{mg/mL}$ **XIII**

(e) $\phi_{RBC} = 0.09$ $[fd] = 0.52\,\text{mg/mL}$ **XIV**

(f) $\phi_{RBC} = 0.09$ $[fd] = 2.18\,\text{mg/mL}$ **XV**

(g) $\phi_{RBC} = 0.17$ $[fd] = 0.22\,\text{mg/mL}$ **XVI**

(h) $\phi_{RBC} = 0.17$ $[fd] = 0.44\,\text{mg/mL}$ **XVII**

(i) $\phi_{RBC} = 0.17$ $[fd] = 0.57\,\text{mg/mL}$ **XVIII**

(j) $\phi_{RBC} = 0.17$ $[fd] = 2.18\,\text{mg/mL}$ **XIX**

Figure 4.16: Gas-Cluster co-existence phase (G+C) RBC-*fd* mixtures at different volume fractions ϕ_{RBC} and concentration $[fd]$. Roman numerals refer to data points in Fig. 4.14. Scale bar is 20 µm

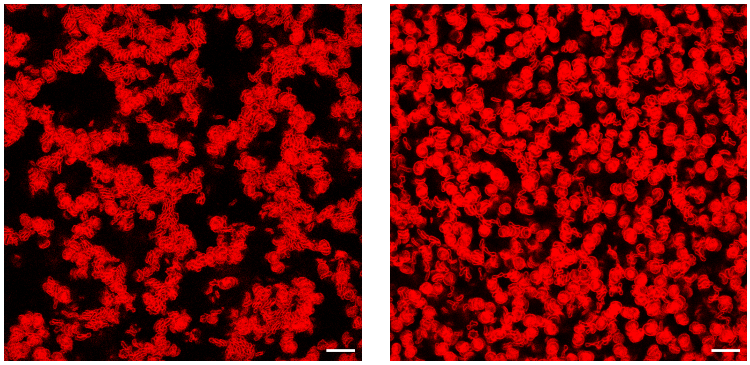

(a) $\phi_{RBC} = 0.29$
$[fd] = 0.62\,\mathrm{mg/\,mL}$
XX

(b) $\phi_{RBC} = 0.38$
$[fd] = 0.57\,\mathrm{mg/\,mL}$
XXI

Figure 4.17: Percolation phase (P) RBC-*fd* mixtures at different volume fraction ϕ_{RBC} and concentration $[fd]$. Roman numerals refer to data points in Fig. 4.14. Scale bar 20 µm

4.2.3 Percolation phase

Whereas percolated networks of RBC-Dex were composed of connected rouleaux, RBC-*fd* are composed of much less ordered structures. It is not possible to differentiate substructures in the percolated networks. The difference comes from the difference in the nature of aggregation mechanism. With Dextran, we have bridging and depletion, where bridging from the sides (to make a clump of cells) does not maximise the contact surface. On the other hand when the cells are stacked linearly, face to face, the contact surface is maximised (the attraction energy is proportional to the contact surface). For *fd*, depletion attraction seeks to increase the overlap volume of RBCs and it does not matter how the cells are aggregated. *Fd* is pushing cells in forming clusters of cells, whereas bridging leads to rouleaux formation.

Table 4.2 shows which samples were used to determine the percolation line. The output images of the percolation algorithm for the samples in table 4.2 can be accessed by the reader as seen in Appendix A.

It has to be mentioned that the percolation algorithm found percolation paths in three

Sample	Exp. ϕ_{RBC}	$[fd]$ (mg/ mL)	Calc. ϕ_{RBC}	X paths	Y paths	Z paths
XVIII	0.17	0.57	0.243	110	8	480
XIX	0.17	2.18	0.170	0	0	133
XX	0.29	0.62	0.316	144	18	12
XXI	0.38	0.57	0.437	160	176	6150

Table 4.2: Images classified by WEKA segmentation. Table shows calculated and experimental volume fractions ϕ_{RBC}. The number of paths found by the percolation algorithm are given for X,Y and Z separate

directions in sample XVIII (Fig. 4.16i). We do not count this sample to be in the percolation phase, since we think the dimensions of the image are too small and that percolation paths in the horizontal plane will not be observed if the image was the usual ($250\,\mu\mathrm{m} \times 250\,\mu\mathrm{m}$). We did not have such an image available at the time of the analysis.

4.3 Rheology of percolated networks

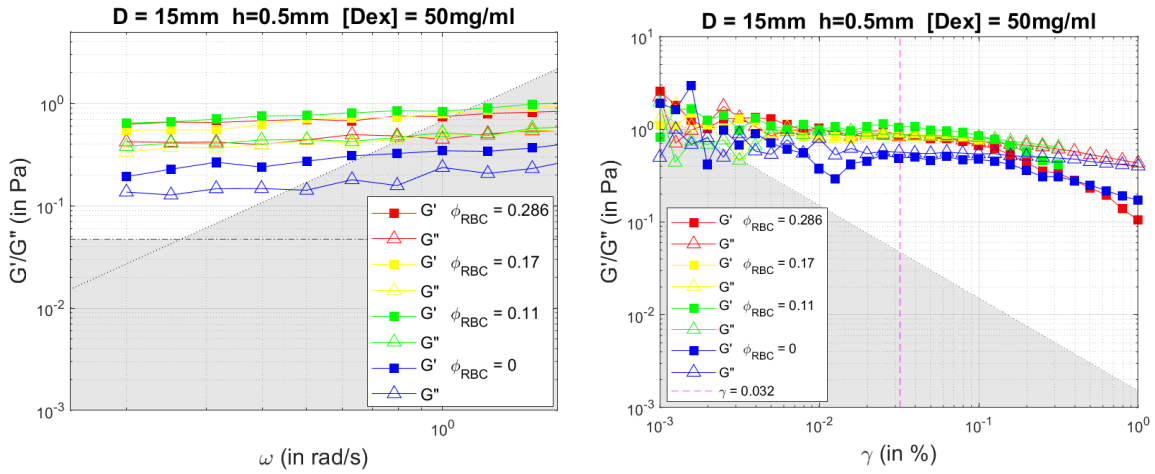

(a) Amplitude sweep (AS)

(b) Frequency sweep with $\gamma_0 = 0.032$

Figure 4.18: DMA on mixtures of RBCs and Dex with PP $D = 15\,\mathrm{mm}$ geometry and gap $h = 0.5\,\mathrm{mm}$. Grey regions indicate experimental boundaries

Dynamic Mechanical Analysis (DMA) on mixtures of red blood cells and Dextran (Dex) can demonstrate the rheological behaviour of the specimen. In figure 4.18a, the dynamic moduli are measured in function of frequency to show the nature of the samples on different timescales. The samples were analysed with an Anton Paar MCR 702b twin-drive rheometer and a parallel plate (PP) geometry of diameter $D = 15\,\mathrm{mm}$. The gap between the plates was taken $h = 0.5\,\mathrm{mm}$. We performed a Frequency Sweep (FS), with input $\gamma(t) = \gamma_0 \sin \omega t$, after determining $\gamma_0 = 0.036$ from an Amplitude Sweep (AS). In the amplitude sweep G' and G" are measured in function of strain γ. In the linear regime, $\gamma < \gamma_c$, G' and G" are supposed to be constant. Above a critical strain γ_c they decrease. In order to perform a FS in the linear regime, the applied strain should be below the critical one $\gamma_0 < \gamma_c$.

From the frequency sweep, we observe relatively constant moduli over a range of frequencies. Moreover, since the storage modulus is larger than the loss modulus $G' > G$", there is a more elastic response that can correspond to gel behaviour. However, the behaviour appears similar for different ϕ_{RBC}, while we would expect stronger gels when more RBCs are present and the network is more extensive. The same frequency sweep on a sample without RBCs and $[Dex] = 50\,\mathrm{mg/\,mm}$ unexpectedly displays identical behaviour, albeit at lower G. The trend that we see in all these samples, is therefore attributed to Dex and not the red blood cells. Although we thus not observe gelation of RBCs, some kind of structure is present, since we do not have a liquid (viscous) response where $G' < G$". We speculate that we observe a crystallisation of the dextran solution instead. Fluid could evaporate from between the plates, altering the results.

A potential solution to this problem could be the incorporation of a solvent trap for the geometry. This would prevent fluid from escaping the geometry, changing the results. Such a solvent trap is, however, not compatible with the twin-drive mechanism. The measurements could then be done on a different rheometer (single drive), but that would give less accurate

measurements. Another potential solution is the use of a different geometry, like a Couette cup. Couette cups are often used in haemorheology [81] but require sample volumes above a mL. This is not possible in the current experimental procedure as we do not extract enough blood daily to make such samples (section 3.1.4). With larger, available quantities of blood, this becomes a possibility to consider.
The experimental boundaries depend on the minimal measurable torque M_{min} (instrument specific) and the instrument inertia I (geometry specific) [104]. The rheometer has a minimal measurable torque which leads to a minimal measurable modulus

$$G_{min} > \frac{C_\sigma M}{\gamma_0} \tag{4.6}$$

where C_σ is a constant to measure the stress response $\sigma = C_\sigma M$. Further, the total torque measured will be the sum of material torque M_{mat} and instrument torque $M_I = \theta I \omega^2$. It can then be shown that

$$G_{min} > \frac{C_\sigma}{C_\gamma} I \omega^2 \tag{4.7}$$

must be satisfied, where C_γ is a constant to record strain $\gamma = C_\gamma \theta$.
For a parallel plate geometry these constants are calculated from the radius of the plates R and the separation between them h [105]

$$C_\gamma = \frac{R}{h} \qquad C_\sigma = \frac{2}{\pi R^3} \tag{4.8}$$

From calibration measurements, the inertia of the PP 15 mm geometry was determined to be $I = 6.718 \times 10^{-6}\,\mathrm{kg\,m^2}$.

Chapter 5

Miscellaneous

In the following chapter, we present some results that, although not crucial to the results of this work, can be of importance and help to further studies of RBC networks and aggregates.

5.1 Depth limited confocal scanning

In order to visualise the bulk of the formed RBC networks, samples need to be examined over sufficient distances. Tuning the magnification alters the pixel dimensions in the axial plane. Further, the image size depends on the amount of pixels scanned by the confocal. The majority of phase diagram images are scanned over an area of $(250\,\mu\mathrm{m} \times 250\,\mu\mathrm{m})$.
Axially the spacing between two subsequently scanned horizontal planes is chosen by the user. In this work, a Z-spacing of $0.334\,\mu\mathrm{m}$ is chosen most of the time. However, it is not possible through the whole height of the sample. In this work, samples were loaded into Ibidi®μ-slide VI 0.1 (cat.No 80666) channels. The channel measures 17 mm in length, 1 mm in width and have a height of 100 µm. We observe that the fluorescence intensity decreases rapidly within the channels, limiting the depth scanning of the sample. Figure 5.1 shows the fluorescence intensity in function of depth for some samples of RBCs with Dex. At each Z-position the intensity was calculated by summing the individual pixel intensities in the corresponding horizontal plane. This value was then normalised and the maxima were set at the origin. Each of these images were scanned from a position just under the channel up to 100 µm in to the channel.

This shows that there is a rapid and seemingly exponential intensity decay with going deeper into the sample. This is expected since light coming from fluorophores has an increased probability to scatter before reaching the PMT detector. The shape of the curves can be explained as follows. At first the intensity is zero since we scan outside the channel, then it suddenly increases to a maximum. This early peak results from RBCs that are attached to the wall because of an attraction interaction combined with possible sedimentation, as can also be seen in the images. As we get deeper into the channel, the intensity drops exponentially. Samples with higher ϕ_{RBC} show very high intensities since there are more RBCs, and thus more fluorescence, in each plane. However, more RBCs also increase the scattering probability, resulting in a more abrupt intensity decrease. To find out how large the contribution of RBCs was to this effect, the same procedure was undertaken for a channel filled with homogeneous dye solution of 5% Promofluor Premium 488 carboxylic dye in water. For the homogeneous

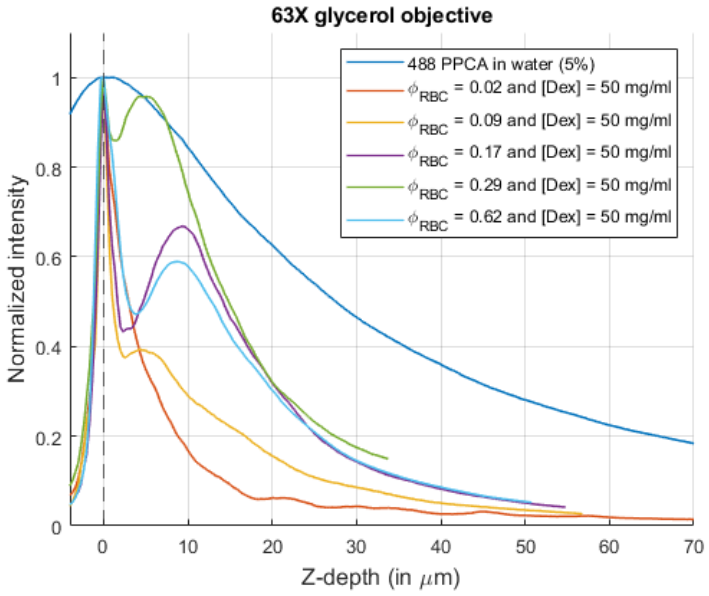

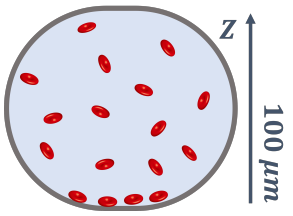

(a) Cross-section of Ibidi μ-slide channel

Figure 5.1: Normalised fluorescence intensity in function of depth of the channel measured on RBC-Dex mixtures and a sample of homogeneous Promofluor Premium 488 carboxylic acid dye in water (5%). Origin fixed at maxima

dye, the exponential decrease was also observed but over larger distance. Scattering by RBCs thus is a defining factor that is hard to overcome.
The samples of RBCs could be properly scanned up to $30 - 40\,\mu m$, which is still enough to observe percolation but not close to the entire height of the channel (100 µm). In order to scan as deep as possible, our dye emitted fluorescent light in the red part of the electromagnetic spectrum (>600 nm) since long wavelength light tends to scatter less. We expect a much better penetration of the sample when imaging with a 2-photon microscope that then excited non-linearly with 2 infrared photons instead. Although this does not change the scattering of the emitted fluorescence, it would reduce the scattering of the emission light, possibly resulting in more excited fluorophores. In addition, the right choice of objective also influences measurements. Here, we work with a 63X glycerol objective with refractive index $n = 1.46$ and $NA = 1.3$.

5.2 Dye influenced echinocyte transformation

In search of the right experimental procedures, we experienced multiple issues with the right conditions of the sample. Work on RBC aggregation requires cells with discocyte shape. This intrinsic RBC shape, is extremely dependent on it's environment, as explained in section 2.2. A change of pH, or other factors can make the cells go echinocyte, thus rendering those samples useless to this research. Naturally the state of the products used for the sample are crucial. Aged PBS or PBS-OP can get contaminated by dust or bacteria that can then cause increased echinocyte occurrence.
Besides this obvious factors, we also experienced that labelling the cells with too much CellMask dye also increases the formation of echinocytes. In figure 5.2, cells were labelled with the proposed amount of dye (Fig. 5.2a) and double that amount (Fig. 5.2b). Apart from

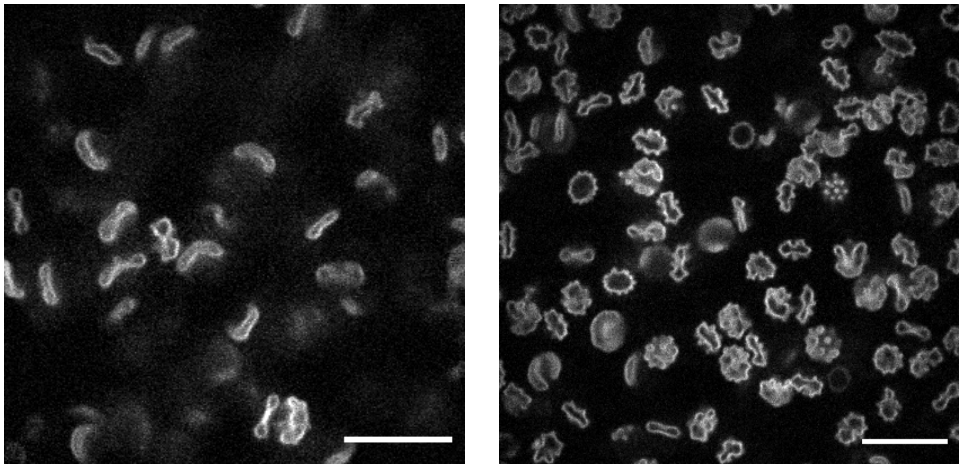

(a) $\phi_{RBC} = 0.02$ $V_{dye} = 0.2\,\mu\text{L}$ (b) $\phi_{RBC} = 0.02$ $V_{dye} = 0.4\,\mu\text{L}$

Figure 5.2: Enhanced discocyte-echinocyte transition in samples where RBCs are labelled with too much dye

the amount of dye used, all other conditions were identical for these samples. Blood from the same day, same ϕ_{RBC}, same amounts of PBS and PBS-OP.

Chapter 6

Conclusion and outlook

In this thesis, we studied red blood cell aggregation and percolation. We visually identified different phases of RBC-macromolecule mixtures and developed a direct method of detecting percolation in confocal images to identify networks of RBCs.

Unlike spherical colloids, the shape anisotropy of RBCs allows for the formation of stable linear aggregates, termed rouleaux. Whereas RBC aggregation and colloidal gels are both well studied topics, the study of RBC colloidal gels remains largely untouched. We investigated the existence and properties of RBC networks where aggregation is induced by *fd*-virus (an ideal long-range depletant), and Dex 70kDa (a short-range depletion-bridging hybrid macromolecule).

For mixtures of RBCs and Dex, four distinct phases were classified: the gas phase (G), the gas-rouleaux co-existence phase (G+R), the branched rouleaux phase (BR) and the percolation phase (P).
In the gas phase, we obtained confocal images at high ϕ_{RBC} without aggregating macromolecules. We estimate a critical ϕ_{RBC} where RBCs cannot be packed without deforming, for which an upper limit ($\phi_{RBC} < 0.75$) was found experimentally.
The following, rouleaux phase, is characterised by the appearance of 1D 'rouleaux' crystals. The length of this rouleaux is shown to evolve linearly at constant $[Dex]$ with increasing ϕ_{RBC}.
Closely linked to the rouleaux phase, is the branched rouleaux phase.
At high ϕ_{RBC}, we find that aggregation of RBCs results in the formation of percolated networks. For the direct detection of these percolated networks, we developed a *percolation algorithm*, that checks percolation through the detection of individual paths throughout the RBC-structure in three directions X,Y and Z. Many samples of RBCs and Dex were examined to determine the exact percolation line of the system. These percolated networks have an open structure in comparison to spherical colloidal gels. We suggest this is because the network is composed of individual, long rouleaux of RBCs that form branched structures. In future research, this branching can be studied by inspection aggregation of rouleaux into networks.

In addition, mixtures of RBCs and *fd* culminate in, besides gas and percolation phases, a cluster phase that shows more clumped aggregates. This confirms the inherent difference in aggregation mechanism of *fd*, compared to Dex, where almost exclusively linear rouleaux aggregates are perceived. We suggest that future work on these mixtures should mainly focus on quantitatively describing the phases and expand the phase diagram into unknown regions,

mainly high ϕ_{RBC}.

Further research is needed into characterisation of the nature of percolated RBC networks. Furthermore, rheological measurements can also provide evidence of yield stress σ_y in gels. Therefore, examining the yield stress of samples in the percolated phase, can become a further criterion to distinguish percolated networks. Also with increased interaction strength, an increased σ_y is expected. The future aim would be to make confocal images while shearing the percolated networks. This rheo-confocal measurements would exactly show how the percolated networks behave under shear, and where they will break up into rouleaux or even single RBCs.

Bibliography

[1] E. W. Merrill, G. C. Cokelet, A. Britten, and R. E. Wells, "Non-Newtonian rheology of human blood–effect of fibrinogen deduced by "subtraction".", Circulation research **13**, 48–55 (1963).

[2] C. Picart, J.-M. Piau, H. Galliard, and P. Carpentier, "Human blood shear yield stress and its hematocrit dependence", Journal of Rheology **42**, 1–12 (1998).

[3] R. Fåhraeus, "THE SUSPENSION STABILITY OF THE BLOOD", Physiological Reviews **9**, 241–274 (1929).

[4] E. W. Merrill, E. R. Gilliland, T. S. Lee, and E. W. Salzman, "Blood rheology: effect of fibrinogen deduced by addition.", Circulation research **18**, 437–446 (1966).

[5] S. Asakura and F. Oosawa, *On interaction between two bodies immersed in a solution of macromolecules*, Dec. 1954.

[6] B. Neu and H. J. Meiselman, "Depletion-mediated red blood cell aggregation in polymer solutions", Biophysical Journal **83**, 2482–2490 (2002).

[7] S. Chien and K. m. Jan, "Ultrastructural basis of the mechanism of rouleaux formation", Microvascular Research **5**, 155–166 (1973).

[8] G. Yuan, J. Luo, C. C. Han, and Y. Liu, "Gelation transitions of colloidal systems with bridging attractions", Physical Review E **94**, 040601 (2016).

[9] H. Tanaka, Y. Nishikawa, and T. Koyama, "Network-forming phase separation of colloidal suspensions", Journal of Physics Condensed Matter **17**, L143 (2005).

[10] S. Chien, S. Simchon, R. E. Abbott, and K. M. Jan, "Surface adsorption of dextrans on human red cell membrane", Journal of Colloid And Interface Science **62**, 461–470 (1977).

[11] M. Naessens, A. Cerdobbel, W. Soetaert, and E. J. Vandamme, *Leuconostoc dextransucrase and dextran: Production, properties and applications*, Aug. 2005.

[12] D. Guu, J. K. Dhont, G. A. Vliegenthart, and M. P. Lettinga, "Depletion induced clustering in mixtures of colloidal spheres and fd-virus", Journal of Physics Condensed Matter **24**, 464101 (2012).

[13] Encyclopædia Britannica, *Blood diagram*.

[14] O. Korculanin, "Disk-like Particles under Shear Flow Understanding the physics behind yielding of colloidal disks in the nematic phase and the mechanics of red blood cell (dis)aggregation", PhD thesis (KU Leuven, Leuven, 2021).

[15] T. R. Gregory, "The bigger the C-value, the larger the cell: Genome size and red blood cell size in vertebrates", Blood Cells, Molecules, and Diseases **27**, 830–843 (2001).

[16] K. A. Brown, "Erythrocyte metabolism and enzyme defects", Laboratory Medicine **27**, 329–333 (1996).

[17] M. D. Mager, V. Lapointe, and M. M. Stevens, "Exploring and exploiting chemistry at the cell surface", Nature Chemistry **3**, 582–589 (2011).

[18] H. P. Fernandes, C. L. Cesar, and M. d. L. Barjas-Castro, "Electrical properties of the red blood cell membrane and immunohematological investigation", Revista Brasileira de Hematologia e Hemoterapia **33**, 297–301 (2011).

[19] N. Unsain, F. D. Stefani, A. Cáceres, S. Halpain, C. Leterrier, A. Prokop, and P. E. Hotulainen, "The Actin/Spectrin Membrane-Associated Periodic Skeleton in Neurons", `10.3389/fnsyn.2018.00010` (2018).

[20] G. R. Lázaro, K. A. Melzak, J. L. Toca-Herrera, I. Pagonabarraga, and A. Hernández-Machado, "Elastic energies and morphologies of the first stages of the discoechinocyte transition", Soft Matter **9**, 6430–6441 (2013).

[21] A. S. Smith, R. B. Nowak, S. Zhou, M. Giannetto, D. S. Gokhin, J. Papoin, I. C. Ghiran, L. Blanc, J. Wan, and V. M. Fowler, "Myosin IIA interacts with the spectrin-actin membrane skeleton to control red blood cell membrane curvature and deformability", Proceedings of the National Academy of Sciences of the United States of America **115**, E4377–E4385 (2018).

[22] B. J. Bain, *Blood cells: a practical guide*, 4th ed. (Blackwell Publishing, Oxford, 2007).

[23] C. E. McLaren, G. M. Brittenham, and V. Hasselblad, "Statistical and graphical evaluation of erythrocyte volume distributions", American Journal of Physiology - Heart and Circulatory Physiology **252**, `10.1152/ajpheart.1987.252.4.h857` (1987).

[24] B. Angelov and Ivailo M. Mladenov, *On the Geometry of Red Blood Cell*, tech. rep. (Institute of Biophysics and Biomedical Engineering, Bulgarian Academy of Sciences, Sofia, Jan. 2000), pp. 27–46.

[25] Y. Kim, K. Kim, and Y. Park, "Measurement Techniques for Red Blood Cell Deformability: Recent Advances", `10.5772/50698` (2012).

[26] N. M. Geekiyanage, M. A. Balanant, E. Sauret, S. Saha, R. Flower, C. T. Lim, and Y. T. Gu, "A coarse-grained red blood cell membrane model to study stomatocyte-discocyteechinocyte morphologies", PLoS ONE **14**, e0215447 (2019).

[27] I. Mustafa, A. Al Marwani, K. Mamdouh Nasr, N. Abdulla Kano, and T. Hadwan, "Time Dependent Assessment of Morphological Changes: Leukodepleted Packed Red Blood Cells Stored in SAGM", BioMed Research International **2016**, `10.1155/2016/4529434` (2016).

[28] C. Wagner, P. Steffen, and S. Svetina, *Aggregation of red blood cells: From rouleaux to clot formation*, June 2013.

[29] S. R. Cho, *Plasma cell leukemia with rouleaux formation involving: Neoplastic cells and RBC*, Sept. 2011.

[30] E. Giudice, V. Voeikov, A. Tedeschi, and G. Vitiello, *The origin and the special role of coherent water in living systems*, Vol. 37661 (May 2015), pp. 95–111.

[31] H. N. Lekkerkerker and R. Tuinier, *Colloids and the Depletion Interaction*, Vol. 833, Lecture Notes in Physics (Springer Netherlands, Dordrecht, 2011).

[32] K. M. Jan and S. Chien, "Role of surface electric charge in red blood cell interactions", Journal of General Physiology **61**, 638–654 (1973).

[33] S. Chien, L. A. Sung, S. Kim, A. M. Burke, and S. Usami, "Determination of aggregation force in rouleaux by fluid mechanical technique", Microvascular Research **13**, 327–333 (1977).

[34] D. E. Brooks, J. W. Goodwin, and G. V. Seaman, "Interactions among erythrocytes under shear.", Journal of applied physiology **28**, 172–177 (1970).

[35] D. E. Brooks and G. V. Seaman, "The effect of neutral polymers on the electrokinetic potential of cells and other charged particles. I. Models for the zeta potential increase", Journal of Colloid And Interface Science **43**, 670–686 (1973).

[36] P. Bagchi, P. C. Johnson, and A. S. Popel, "Computational fluid dynamic simulation of aggregation of deformable cells in a shear flow", Journal of Biomechanical Engineering **127**, 1070–1080 (2005).

[37] H. Schmid-Schönbein, P. Gaehtgens, and H. Hirsch, "On the shear rate dependence of red cell aggregation in vitro", Journal of Clinical Investigation **47**, 1447–1454 (1968).

[38] O. Baskurt, B. Neu, and H. J. Meiselman, *Red blood cell aggregation*, 1st ed. (CRC Press, Boca Raton, June 2011), pp. 1–288.

[39] J. Swenson, M. V. Smalley, and H. L. Hatharasinghe, "Mechanism and strength of polymer bridging flocculation", Physical Review Letters **81**, 5840–5843 (1998).

[40] G. Barshtein, I. Tamir, and S. Yedgar, "Red blood cell rouleaux formation in dextran solution: Dependence on polymer conformation", European Biophysics Journal **27**, 177–181 (1998).

[41] A. V. Vrij, "Polymers At Interfaces And The Interactions in Colloidal Dispersions", Pure and Applied Chemistry **48**, 471–483 (1976).

[42] F. K. Lin-In-On, B. Vincent, and F. A. Waite, "STABILITY OF STERICALLY STABILIZED DISPERSIONS AT HIGH POLYMER CONCENTRATIONS.", in Acs symposium series, 9 (1974), pp. 165–172.

[43] B. Vincent, J. Edwards, S. Emmett, and A. Jones, "Depletion flocculation in dispersions of sterically-stabilised particles ("soft spheres")", Colloids and Surfaces **18**, 261–281 (1986).

[44] A. Jones and B. Vincent, "Depletion flocculation in dispersions of sterically-stabilised particles 2. Modifications to theory and further studies", Colloids and Surfaces **42**, 113–138 (1989).

[45] B. Vincent, "The calculation of depletion layer thickness as a function of bulk polymer concentration", Colloids and Surfaces **50**, 241–249 (1990).

[46] S. Chien, "Electrochemical interactions between erythrocyte surfaces", Thrombosis Research **8**, 189–202 (1976).

[47] H. Bäumler and E. Donath, "Does dextran indeed significantly increase the surface potential of human red blood cells?", Studia Biophysica **120**, 113–122 (1987).

[48] H. Bäumler, E. Donath, A. Krabi, W. Knippel, A. Budde, and H. Kiesewetter, "Electrophoresis of human red blood cells and platelets. Evidence for depletion of dextran", Biorheology **33**, 333–351 (1996).

[49] V. A. Parsegian and E. A. Evans, "Long and short range intermolecular and intercolloidal forces", Current Opinion in Colloid and Interface Science **1**, 53–60 (1996).

[50] H. N. Lekkerkerker and R. Tuinier, "Depletion interaction", Lecture Notes in Physics **833**, 57–108 (2011).

[51] E. Eisenriegler, "Universal density-force relations for polymers near a repulsive wall", Physical Review E - Statistical Physics, Plasmas, Fluids, and Related Interdisciplinary Topics **55**, 3116–3123 (1997).

[52] Z. Dogic, K. R. Purdy, E. Grelet, M. Adams, and S. Fraden, "Isotropic-nematic phase transition in suspensions of filamentous virus and the neutral polymer Dextran", Physical Review E - Statistical Physics, Plasmas, Fluids, and Related Interdisciplinary Topics **69**, 9 (2004).

[53] C. A. Haynes, R. A. Beynon, R. S. King, H. W. Blanch, and J. M. Prausnitz, "Thermodynamic properties of aqueous polymer solutions: poly(ethylene glycol)/dextran", Journal of physical chemistry **93**, 5612–5617 (1989).

[54] K. Lee, M. Kinnunen, M. D. Khokhlova, E. V. Lyubin, A. V. Priezzhev, I. Meglinski, and A. A. Fedyanin, "Optical tweezers study of red blood cell aggregation and disaggregation in plasma and protein solutions", Journal of Biomedical Optics **21**, 035001 (2016).

[55] C. E. HALL and H. S. SLAYTER, "The fibrinogen molecule: its size, shape, and mode of polymerization.", The Journal of biophysical and biochemical cytology **5**, 11–16 (1959).

[56] D. A. Marvin and H. Hoffmann-Berling, "Physical and chemical properties of two new small bacteriophages", Nature **197**, 517–518 (1963).

[57] K. H. Lin, J. C. Crocker, A. C. Zeri, and A. G. Yodh, "Colloidal interactions in suspensions of rods", Physical Review Letters **87**, 88301–1 (2001).

[58] J. Opdam, M. P. Schelling, and R. Tuinier, "Phase behavior of binary hard-sphere mixtures: Free volume theory including reservoir hard-core interactions", Journal of Chemical Physics **154**, 74902 (2021).

[59] G. A. Vliegenthart, A. Van Blaaderen, and H. N. Lekkerkerker, "Phase transitions, aggregation and crystallization in mixed suspensions of colloidal spheres and rods", Faraday Discussions **112**, 173–182 (1999).

[60] J. Newman, H. L. Swinney, and L. A. Day, "Hydrodynamic properties and structure of fd virus", Journal of Molecular Biology **116**, 593–603 (1977).

[61] J. Torbet, "Neutron scattering study of the solution structure of bacteriophages Pf1 and fd", FEBS Letters **108**, 61–65 (1979).

[62] E. H. de Hoog, W. K. Kegel, A. van Blaaderen, and H. N. Lekkerkerker, "Direct observation of crystallization and aggregation in a phase-separating colloid-polymer suspension", Physical Review E - Statistical Physics, Plasmas, Fluids, and Related Interdisciplinary Topics **64**, 9 (2001).

[63] H. N. Lekkerkerker and R. Tuinier, "Stability of colloid-polymer mixtures", Lecture Notes in Physics **833**, 131–175 (2011).

[64] V. J. Anderson and H. N. W. Lekkerkerker, "Insights into phase transition kinetics from colloid science", Nature **416**, 811–815 (2002).

[65] D. Kleshchanok, J. M. Meijer, A. V. Petukhov, G. Portale, and H. N. Lekkerkerker, "Attractive glass formation in aqueous mixtures of colloidal gibbsite platelets and silica spheres", Soft Matter **7**, 2832–2840 (2011).

[66] F. Cardinaux, E. Zaccarelli, A. Stradner, S. Bucciarelli, B. Farago, S. U. Egelhaaf, F. Sciortino, and P. Schurtenberger, "Cluster-driven dynamical arrest in concentrated lysozyme solutions", Journal of Physical Chemistry B **115**, 7227–7237 (2011).

[67] D. A. Weitz and M. Oliveria, "Fractal structures formed by kinetic aggregation of aqueous gold colloids", Physical Review Letters **52**, 1433–1436 (1984).

[68] P. J. Flory, "Molecular Size Distribution in Three Dimensional Polymers. I. Gelation", Journal of the American Chemical Society **63**, 3083–3090 (1941).

[69] M. Li, R. R. Liu, L. Lü, M. B. Hu, S. Xu, and Y. C. Zhang, "Percolation on complex networks: Theory and application", Physics Reports **907**, 1–68 (2021).

[70] K. A. Whitaker, Z. Varga, L. C. Hsiao, M. J. Solomon, J. W. Swan, and E. M. Furst, "Colloidal gel elasticity arises from the packing of locally glassy clusters", Nature Communications **10**, 1–8 (2019).

[71] D. Bonn and M. M. Denn, "Yield stress fluids slowly yield to analysis", Science **324**, 1401–1402 (2009).

[72] E. C. Bingham, "An investigation of the laws of plastic flow", Bulletin of the Bureau of Standards **13**, `10.6028/bulletin.304` (1916).

[73] A. J. Apostolidis, M. J. Armstrong, and A. N. Beris, "Modeling of human blood rheology in transient shear flows", Journal of Rheology **59**, 275–298 (2015).

[74] N. Casson, "Flow Equation for Pigment Oil Suspensions of the Ink Type", Rheology of Dispersed Systems, 84–102 (1959).

[75] M. Lattuada, H. Wu, A. Hasmy, and M. Morbidelli, "Estimation of fractal dimension in colloidal gels", Langmuir **19**, 6312–6316 (2003).

[76] S. Bindgen, F. Bossler, J. Allard, and E. Koos, "Connecting particle clustering and rheology in attractive particle networks", Soft Matter **16**, 8380–8393 (2020).

[77] Y. He, P. G. Boswell, P. Bühlmann, and T. P. Lodge, "Ion gels by self-assembly of a triblock copolymer in an ionic liquid", Journal of Physical Chemistry B **111**, 4645–4652 (2007).

[78] Y. Liao, "Practical electron microscopy and database", An Online Book (2006).

[79] D. Amadeus and D. Flormann, "Physical charaterization of red blood cell aggregation", PhD thesis ().

[80] Life Technologies/ ThermoFischer Scientific, *CellMask ™ Plasma Membrane Stains / 2*, tech. rep. (Life Sciences, Carlsbad, CA, USA, 2014).

[81] O. Baskurt, M. Boynard, G. Cokelet, P. Connes, B. M. Cooke, S. Forconi, F. Liao, M. Hardeman, F. Jung, H. Meiselman, and O. K. Baskurt, *New guidelines for hemorheological laboratory techniques*, tech. rep. 2 (2009).

[82] W. H. Reinhart, N. Z. Piety, J. W. Deuel, A. Makhro, T. Schulzki, N. Bogdanov, J. S. Goede, A. Bogdanova, R. Abidi, and S. S. Shevkoplyas, "Washing stored red blood cells in an albumin solution improves their morphologic and hemorheologic properties", Transfusion **55**, 1872–1881 (2015).

[83] A. Orbach, O. Zelig, S. Yedgar, and G. Barshtein, "Biophysical and Biochemical Markers of Red Blood Cell Fragility", Transfus Med Hemother **44**, 183–187 (2017).

[84] Anton Paar, *The Modular Compact Rheometer series*, tech. rep. (Anton Paar GmbH, Graz, Austria, 2021).

[85] A. Nwaneshiudu, C. Kuschal, F. H. Sakamoto, R. Rox Anderson, K. Schwarzenberger, and R. C. Young, "Introduction to confocal microscopy", Journal of Investigative Dermatology **132**, 1–5 (2012).

[86] N. S. Claxton, T. J. Fellers, and M. W. Davidson, *LASER SCANNING CONFOCAL MICROSCOPY*, tech. rep. ().

[87] J. B. Pawley, *Handbook of biological confocal microscopy: Third edition* (Springer US, 2006), pp. 1–985.

[88] I. C. Ghiran, "Introduction to Fluorescence Microscopy", in *Light microscopy: methods and protocols*, edited by R. C. N. Chiarini-Garcia Helioand Melo (Humana Press, Totowa, NJ, 2011), pp. 93–136.

[89] A. H. Coons, J. Creech, R. Norman, and E. Berliner, "The Demonstration of Pneumococcal Antigen in Tissues by the Use of Fluorescent Antibody", The Journal of Immunology **45** (1942).

[90] A. H. Coons, "THE APPLICATION OF FLUORESCENT ANTIBODIES TO THE STUDY OF NATURALLY OCCURRING ANTIBODIES", Annals of the New York Academy of Sciences **69**, 658–662 (1957).

[91] M. Minsky, *Memoir on Inventing the Confocal Scanning Microscope*, tech. rep. (1988), pp. 128–138.

[92] N. S. Claxton, T. J. Fellers, and M. W. Davidson, "Microscopy, Confocal", in *Encyclopedia of medical devices and instrumentation* (John Wiley & Sons, Inc., Hoboken, NJ, USA, Apr. 2006).

[93] Leica-Microsystems GmbH, *All-Purpose Super-Sensitivity Leica HyD for Confocal Imaging*, tech. rep. (Leica Microsystems GmbH, Wetzlar, Germany, 2015).

[94] E. H. K. Stelzer, "The Intermediate Optical System of Laser-Scanning Confocal Microscopes", in *Handbook of biological confocal microscopy*, edited by J. B. Pawley (Springer US, Boston, MA, 2006), pp. 207–220.

[95] C. J. Sheppard, "Axial resolution of confocal fluorescence microscopy", Journal of Microscopy **154**, 237–241 (1989).

[96] Leica Microsystems GmbH, *GLYCEROL OBJECTIVE*, tech. rep. (Leica Microsystems Heidelberg GmbH, Mannheim, Germany, Apr. 2004).

[97] J. Schindelin, I. Arganda-Carreras, E. Frise, V. Kaynig, M. Longair, T. Pietzsch, S. Preibisch, C. Rueden, S. Saalfeld, B. Schmid, J.-Y. Tinevez, D. J. White, V. Hartenstein, K. Eliceiri, P. Tomancak, and A. Cardona, "Fiji: an open-source platform for biological-image analysis", Nature Methods **9**, 676–682 (2012).

[98] S. Berg, D. Kutra, T. Kroeger, C. N. Straehle, B. X. Kausler, C. Haubold, M. Schiegg, J. Ales, T. Beier, M. Rudy, K. Eren, J. I. Cervantes, B. Xu, F. Beuttenmueller, A. Wolny, C. Zhang, U. Koethe, F. A. Hamprecht, and A. Kreshuk, "ilastik: interactive machine learning for (bio)image analysis", Nature Methods **16**, 1226–1232 (2019).

[99] S. Sternberg, "Biomedical Image Processing", Computer **16**, 22–34 (1983).

[100] P. Cignoni, M. Callieri, M. Corsini, M. Dellepiane, F. Ganovelli, and G. Ranzuglia, "MeshLab: an Open-Source Mesh Processing Tool", in (The Eurographics Association, 2008), pp. 129–136.

[101] I. Arganda-Carreras, V. Kaynig, C. Rueden, K. W. Eliceiri, J. Schindelin, A. Cardona, and H. S. Seung, "Trainable Weka Segmentation: A machine learning tool for microscopy pixel classification", Bioinformatics **33**, 2424–2426 (2017).

[102] R. Sedgewick and K. Wayne, "Graphs", in *Algorithms*, 4th ed. (Addison-Wesley, Mar. 2011) Chap. 4, pp. 514–693.

[103] P. J. Flory, "Molecular Size Distribution in Linear Condensation Polymers", Journal of the American Chemical Society **58**, 1877–1885 (1936).

[104] E. Koos, *Applied rheology: Experimental challenges*, Leuven, Oct. 2020.

[105] E. Koos and A. Vananroye, *Applied rheology: Rheology and Rheometers*, Leuven, Oct. 2020.

Appendices

Appendix A

Additional material

We grant the readers of this thesis access to the original confocal tiff stacks and the output images of the percolation algorithm, so they have the opportunity to view the images more clearly and in three dimensions. The best way to view tiff stacks is by downloading them and loading them into the free software program FIJI [97] and using the VolumeViewer plug-in. Furthermore, we think this also gives better insight into the networks. More information and supplementary material is also provided. We do remind the reader that no material is to be distributed or used without consulting the author.

RBCs with Dextran:
`https://drive.google.com/drive/folders/1R1fEyzaQC26gTgcAtE9qLcHaAXQ-n69A?usp=sharing`

RBCs with fd:
`https://drive.google.com/drive/folders/1VDxaUqY6WyOuGekARDicDDAfaiq1wlNs?usp=sharing`

Percolation images:
`https://drive.google.com/drive/folders/1ERa2NXHtWCK876aQotq-1z0-5F7PS0bE?usp=sharing`

Departement Natuurkunde en Sterrenkunde
Celestijnenlaan 200d - bus 2412
3001 Leuven, BELGIË
tel. +32 16 32 71 24
www.kuleuven.be